Low-Density Reactive-Extruded Polybutylene Terephthalate Foams with Enhanced Compressive Properties

Von der Fakultät für Ingenieurwissenschaften

der Universität Bayreuth

zur Erlangung der Würde

Doktor-Ingenieurin (Dr.-Ing.)

genehmigte Dissertation

von

M.Sc. (hons.) Merve Aksit (geb. Demir)

aus

Bursa, Türkei

Erstgutachter: *Professor Dr.-Ing. Volker Altstädt*

Zweitgutachter: *Professor Dr. Hans-Werner Schmidt*

Tag der mündlichen Prüfung: *07. Februar 2023*

Lehrstuhl für Polymere Werkstoffe

Universität Bayreuth

2023

Short Summary

In this thesis, a novel route to obtain low-density (< 100 kg/m^3) extruded strand foams made from polybutylene terephthalate (PBT) with a fine cellular and uniform morphology (< 500 µm) was presented. For the first time, organic (1,3,5-benzenetrisamides (BTAs)) and inorganic (halloysites (HNTs)) nanoadditives at various concentrations (< 1 wt%) were used as both nucleating agents for polymer crystals of chemically post-modified PBT (mPBT) and nucleation of mPBT foam cells. Two different BTAs (commercially available BTA (BTA1) and tailor-made BTA (BTA2)) having discrete chemical nature were selected. Among all concentrations, 0.08 wt% BTA1 and 0.02 wt% BTA2 were found to be optimum concentrations leading to the best melt properties, smallest cell size and foams having the best mechanical performance. Compressive test results exhibited that 0.08 wt% BTA1 results in a 25 % increase in compressive strength at the same foam density, whereas 0.02 wt% BTA2 features a 35 % increase at around 15 % larger foam density compared to the one of the neat mPBT. This enhancement is attributed to the improved foam morphology, including finer and more uniform cellular structure as well as to the intrinsic reinforcing effect of BTA fibers in the cell walls and struts. Furthermore, HNT-based extruded foam strands of mPBT were produced in the same manner like BTA-based foams. The highest melt strength, the smallest mean cell size and the highest increase in the compressive strength (26 %) compared to a neat mPBT foam at the same foam density were achieved with only 0.02 wt% HNT concentration. This improvement was also assigned to a more homogeneous foam morphology and to the presence of HNTs in the cell walls and struts. Finally, synergistic effects of combining multiple nanoadditives on the morphology and compressive properties of mPBT foam were presented. The mixture of HNT and BTA2 resulted in foams with the smallest achieved cell size (~ 235 µm) and a foam density of 75 kg/m^3. Yet, the highest compressive strength was achieved with the mixture of all three nanoadditives (BTA1, BTA2 and HNT) at a relatively higher foam density of 98 kg/m^3.

Kurzfassung

In dieser Arbeit wird ein neuartiger Weg zur Herstellung von extrudierten Strangschaumstoffen aus Polybutylenterephthalat (PBT) mit niedriger Dichte (< 100 kg/m^3) und einer feinzelligen und einheitlichen Morphologie (< 500 μm) vorgestellt. Erstmals wurden organische (1,3,5-Benzetrisamide (BTAs)) und anorganische (Halloysite (HNTs)) Nanoadditive in verschiedenen Konzentrationen (< 1 Gew.-%) sowohl als Nukleierungsmittel für Polymerkristalle von chemisch modifiziertem PBT (mPBT) als auch zur Nukleierung von mPBT-Schaumzellen eingesetzt. Es wurden zwei verschiedene BTAs, ein kommerziell erhältliches BTA (BTA1) und ein maßgeschneidertes BTA (BTA2)) mit unterschiedlichen chemischen Eigenschaften ausgewählt. Unter allen Konzentrationen erwiesen sich 0,08 Gew.- % BTA1 und 0,02 Gew.- % BTA2 als optimale Konzentrationen, die zu den besten Schmelzeigenschaften, der kleinsten Zellgröße und zu Schäumen mit den besten mechanischen Eigenschaften führten. Drucktests ergaben, dass 0,08 Gew.- % BTA1 bei gleicher Schaumdichte eine um 25 % höhere Druckfestigkeit bewirkt, während 0,02 Gew.- % BTA2 eine um 35 % höhere Druckfestigkeit bei etwa 15 % höherer Schaumdichte im Vergleich zu reinem mPBT aufweist. Diese Verbesserung wird auf eine feinere und gleichmäßigere Zellstruktur sowie der intrinsischen Verstärkungswirkung der BTA-Fasern in den Zellwänden und -stegen zurückgeführt. Darüber hinaus wurden extrudierte Schaumstränge aus mPBT auf HNT-Basis auf die gleiche Weise hergestellt wie Schaumstoffe auf BTA-Basis. Die höchste Schmelzfestigkeit, die kleinste mittlere Zellgröße und die höchste Steigerung der Druckfestigkeit (26 %) im Vergleich zum reinen mPBT-Schaum bei gleicher Schaumdichte wurden mit nur 0,02 Gew.- % HNT-Konzentration erreicht. Diese Verbesserung wurde auch der besseren Schaummorphologie und den HNTs in den Zellwänden und -stegen zugeschrieben. Schließlich werden die synergistischen Auswirkungen der Kombination mehrerer Nanoadditive auf die Morphologie und die Druckeigenschaften von mPBT-Schaumstoff vorgestellt. Die Mischung aus HNT und BTA2 führte zu Schäumen mit der kleinsten erreichten Zellgröße (~ 235 μm) und Schaumdichte (75 kg/m^3). Die höchste Druckfestigkeit wurde jedoch mit der Mischung aus allen drei Nanoadditiven (BTA1, BTA2 und HNT) bei einer höheren Schaumdichte von 98 kg/m^3 erhalten.

Acknowledgements

Last but certainly not least, I must acknowledge my friends, Gizem and Bünyamin, family and especially my husband, Alper Aksit, for the unwavering support, constant encouragement, and always being there for me all along with my Ph.D. journey. It is all of you to give me the strength to work hard, to make my effort to pursue what I want. I love all of you.

In dedication to my parents, Sükran and M. Ali,

for their endless love, support and encouragement

&

to my beloved daughter, Ayla

Table of Contents

Abbreviations

BA	Blowing agent
PUR	Polyurethane
PS	Polystyrene
PVC	Polyvinylchloride
PE	Polyethylene
i-PP	Isotactic polypropylene
PET	Polyethylene terephthalate
PBT	Polybutylene terephthalate
mPBT	Chemically post-modified PBT
PTFE	Polytetrafluoroethylene
$CaCO_3$	Calcium carbonate
CNFs	Carbon nanofibers
MMT	Montmorillonite
HNTs	Halloysites
BTAs	1,3,5-benzenetrisamides
PLA	Polylactide
PBS	Polybutylene succinate
CBA	Chemical blowing agent
PBA	Physical blowing agent
HCFCs	Hydrochlorofluorocarbons
HFCs	Hydrofluorocarbons
CO_2	Carbon dioxide
N_2	Nitrogen
SCFs	Supercritical fluids
sc-CO_2	Supercritical carbon dioxide
EOS	Equation of state
0D	Zero-dimensional
1D	One-dimensional
2D	Two-dimensional
3D	Three-dimensional
H-bonding	Hydrogen bonding
XPS	Extruded polystyrene
MWCNTs	Multi-walled carbon nanotubes
CNFs	Carbon nanofibers
CNTs	Carbon nanotubes
TEM	Transmission electron microscopy
AFM	Atomic force microscopy
EPA	Environmental protection agency
phr	Parts per hundred of resin
LCBPP	Long-chain branched polypropylene
PMI	Polymethacrylamide
SAN	Styrene acrylonitrile
PVC	Polyvinyl chloride
EPDM	Ethylene–propylene–diene monomer

DDC	Dynamic Decompression and Cooling
CE	Chain extender
TGIC	Triglycidyl isocyanurate
UWG	Underwater granulation
e-PP	Expanded polypropylene
e-PBT	Expanded polybutylene terephthalate
AlPi-Et	Aluminium diethyl phosphinate
PDI	Polydispersity index
MVR	Melt volume rate
rpm	Rotations per minute
DSC	Differential scanning calorimetry
μ-CT	Micro-computer tomography
FE-SEM	Field emission scanning electron microscopy
OCC	Open cell content
NaOH	Sodium hydroxide
DI-H_2O	Deionized water

Symbols

T_m	Melt temperature
p	Gas adsorption pressure
C_{dis}	Concentration of the dissolved gas
k_h	Henry's law constant
ΔH_s	Enthalpy of solution
R_i	Ideal gas constant
T	Absolute temperature
$k_{H,0}$	Constant
C	Concentration
t	Time for diffusion
x	Distance for diffusion
D_c	Diffusion coefficient of the gas
D_0	Pre-exponential factor
E_A	Activation energy in diffusion
ΔG	Free energy change
J_s	Nucleation rate at steady state
J_t	Nucleation rate at transient state
R	Apparent radius of nucleus (bubble)
ΔP	Pressure drop
$\gamma_{\alpha\beta}$	Interfacial energy
$\Delta V_{free\ vol}$	Change in free volume
Z	Zeldovich non-equilibrium factor
β^*	Rate at which gas molecules are added to the critical nucleus
N	Number of nucleation sites per unit volume
ΔG^*	Gibbs free energy of forming a critical nucleus
k	Boltzmann constant
τ	Induction period for establishing steady-state nucleation conditions
θ_c	Wetting or contact angle
β	Angle of conical cavity of a nucleating agent
r^*	Critical radius
ΔG^*_{homo}	Gibbs free energy barrier of forming a critical nucleus in homogeneous nucleation
ΔG^*_{het}	Gibbs free energy barrier of forming a critical nucleus in heterogeneous nucleation
$S(\theta_c,\beta)$	Geometric factor of the nucleating agent
V_g	Volume of a heterogeneously nucleated cell
$V_{g,\ spherical}$	Volume of a spherical cell with the same radius
γ	Surface tension
A	Surface area
p_1	Partial (internal) pressure
V	Volume of the cell (bubble)
T_g	Glass transition temperature
L	Characteristic length

D	Diameter or thickness
d_{avg}	Average diameter
w	Diffusion rate
g	Acceleration of gravity
η	Dynamic viscosity
ρ	Density of the bulk material
α	Melt opening angle
d	Cross-section diameter
T_c	Crystallization temperature
T_{die}	Die temperature
E_f	Elastic modulus of foams
E_s	Elastic modulus of the cell wall (solid, bulk) material
ρ_f	Foam density
ρ_s	Solid polymer density
ϕ_s	Fraction of polymer contained in cell struts
p_0	Internal gas pressure of the cells
v_f	Poisson's ratio
n	Density exponent of foam
σ^*_{pl}	Plastic collapse stress
$\sigma^*_{y,s}$	Yield strength of the cell wall material
t_w	Cell edge (strut) thickness
l_s	Strut length
M_w	Weight-averaged molecular weight
M_n	Number-averaged molecular weight
ϕ	Cooling rate
T_p	Peak temperature
ΔE	Crystallization activation energy
$\eta^+(t)$	Transient shear viscosity
$\eta_E^+(t,\dot{\varepsilon})$	Transient extensional viscosity
S	Strain hardening coefficient
$\dot{\varepsilon}$	Hencky strain
ρ_w	Density of water
m_a	Weight of the foam sample in air
m_w	Weight of the foam sample in water
A_t	Total foam cell areas
D_c	Cell diameter
ρ_c	Cell density
N_c	Number of cells in the selected area
A_s	Area of the selected section
$V_{geometric}$	Geometric volume of the sample
$V_{diffused}$	Volume of the sample into which nitrogen diffused

1 Introduction and Motivation

Foams are solid-gas-phase structured materials, and the way they are made is much like baking a cake. They are composed of a bulk material (the dough), blowing agent (the baking soda) and, in most cases, additives (chocolate chips) to control the morphology and properties (taste). Optimizing the processing technology and parameters is crucial for trapping the gas inside the matrix and avoiding the rupture of cells to achieve the desired properties. The characteristic properties of foams, such as density, cell structure, cell size, rigidity, and cost, vary depending on the bulk material (can be polymers, metals, ceramics, and glass), the blowing agent (BA) (chemical or physical BA) and the additives (e.g., nucleating agents, reinforcing fillers and flame-retardants). Due to their being price-friendly, easy processability and low density, polymers are commonly used as bulk materials for foaming. As a result, the market value of polymer foams worldwide reached almost 90.7 billion U.S. dollars in 2020. By 2025, it is expected to grow approximately 114.8 billion U.S. dollars, at a compound annual growth rate of 4.8% [a]. Polyurethane (PUR), polystyrene (PS), polyvinylchloride (PVC), polyethylene (PE) and elastomers, such as natural rubber and silicone, are the most usually preferred polymers in the polymer foam market. Depending on the field of application, the performance requirements and economics, the final properties of the foams can be adjusted by tailoring the characteristic properties.

Mechanical properties of foams are mainly affected by the mechanical properties of the bulk material (polymer matrix) that they are made of [1]. Semi-crystalline polymers, such as isotactic polypropylene (i-PP), polyethylene terephthalate (PET) and polybutylene terephthalate (PBT), have been gaining tremendous interest as a bulk material for foaming. The foams based on these polymers are vital for applications in transportation and construction, where noticeably high mechanical strength and modulus are required. For these applications, an ongoing task is achieving a significant weight reduction without significantly deteriorating mechanical properties, which can be enabled by foam extrusion technology [2].

However, foam extrusion of semi-crystalline polymers is a challenging task due to their poor rheological properties, including low elasticity, melt viscosity and strength [3]. Compared to

amorphous polymers such as PS, semi-crystalline polymers such as PBT show a narrower processing temperature window (Fig. 1).
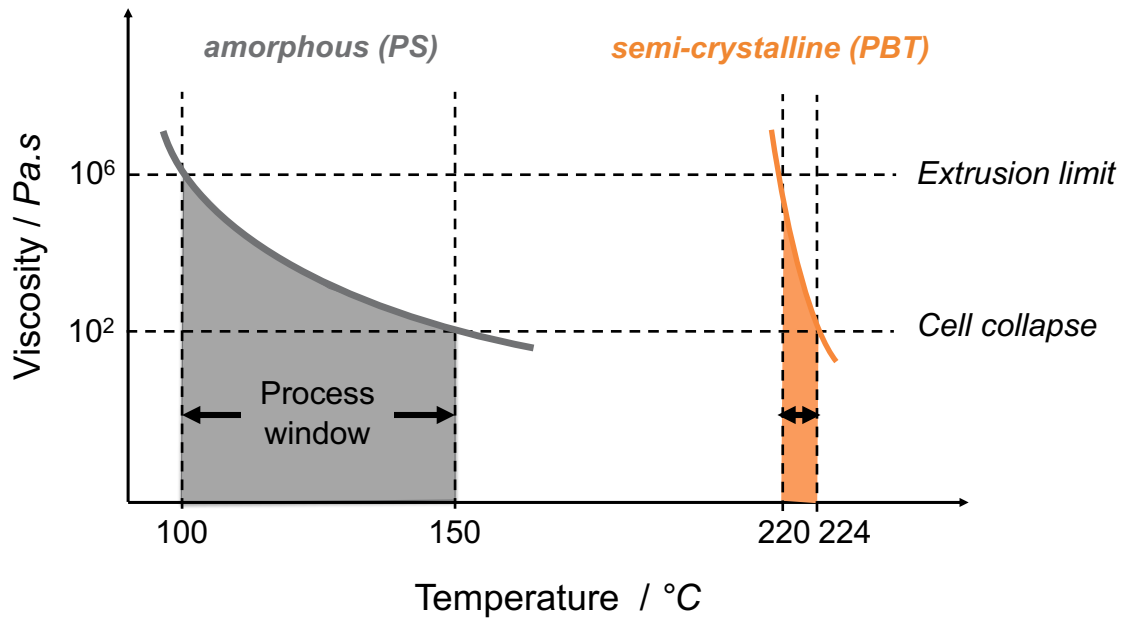
Figure 1 Processing window for foaming of amorphous and semi-crystalline polymers. Reproduced from [4].

When the melt temperature (T_m) exceeds the upper-temperature limit at the processing window, sagging and cell collapse during the foam extrusion process is inevitable. At temperatures below the lower-temperature limit, the process reaches its limit with a rapid increase in barrel pressure in the extruder due to polymer melt solidification induced by crystallization. Both cases are responsible for foams with coarse cell morphology, high foam density and thus deteriorated mechanical properties.

To address this problem, there have been numerous attempts in the literature to improve the rheological properties and thus foamability of semi-crystalline polymers, in particular polyesters, such as PET [5–7] and PBT [8–11]. For instance, post-polymerization modification reactions, namely partial crosslinking [12], long-chain branching, and chain extension are some of the frequently used strategies to widen the processing-temperature window by increasing

melt viscosity, melt strength and strain hardening (extensional thickening) behavior [6,7,13–16].

Despite many attempts to improve melt properties and foamability of PET [4–7,12,17], a limited number of studies on the modification of PBT via reactive extrusion [8–11] and very few studies on extrusion foaming of PBT [2,3,18] exist in the literature. To the best of my knowledge, there is no commercial PBT foam product existing in the market. Yet, the foams of chemically post-modified PBT (mPBT) exhibit great potential in diverse applications within the polymer foam market. For example, insulation or sound absorption in the engine compartment, fish or seafood packaging and construction applications [2–4,18,19]. For these applications, foams with fine cellular structure, relatively low density, high thermal and chemical stability, as well as enhanced mechanical properties are desired. PBT is an up-and-coming candidate to fulfill these requirements due to its appealing bulk properties. Its fast and efficient crystallization behavior features small-sized crystallites, high-temperature dimensional stability, high heat deflection temperature (up to 150 °C), toughness and good chemical and abrasion resistance.

One of the newest strategies to improve the foamability, morphology and mechanical properties of foams is using nanoadditives. They can improve the melt strength and foamability (e.g., graphene [20], polytetrafluoroethylene (PTFE) nanofibers [21], in-situ fibrillated nanofibers [22–24]). A fine and uniform foam morphology is also enabled by the high aspect ratio of the additives (e.g., calcium carbonate ($CaCO_3$) [25], supramolecular additives [26]). Also, they reinforce the cell walls and struts (e.g., carbon nanofibers (CNFs) [27], montmorillonite (MMT) [28], halloysites (HNTs) [29]) by an alignment on the cell walls and struts induced by the bi-axial flow of the bulk material during the foaming (e.g., silica and silicates [30,31]). Finally, they allow controlling the crystallization behavior of bulk material (crystallite size and crystallinity).

Among these organic and inorganic nanoadditives, using 1,3,5-benzenetrisamides (BTAs) and HNTs as foaming additives for semi-crystalline foams is a relatively new approach. BTAs show an advantage as they can be dissolved in the polymer melt at a molecular level when suitable conditions (processing temperature, additive concentration etc.) are provided. Upon cooling, they self-assemble into columnar stacks forming supramolecular nanoobjects. In contrast to

other nanoadditives, poor dispersion and/or agglomeration are not an issue for BTAs. BTAs have already been used successfully for non-polar semi-crystalline i-PP. With only a very low amount of BTAs (< 0.1 wt%), foams with reduced cell size and improved mechanical properties were achieved. Depending on the chemical structure of BTAs, crystal nucleating efficiency and aspect ratio of the self-assembled nanofibers vary. It was found that while some BTA nanofibers lead to crystal nucleation of PBT, nanofibers of other BTAs with different chemical structures are not able to nucleate the polymer [32].

On the other hand, HNTs offer essential benefits, such as being naturally occurring, abundant and low-priced, low carbon footprint and easy to handle during processing. HNTs are kaolinite-based one-dimensional, inorganic clay nanoadditives, having been used as foaming additives for polylactide (PLA) [29,33], PP [34] and polybutylene succinate (PBS) foams [35]. Their unique tubular geometry and high aspect ratio lead to many nucleating sites featuring fine cellular and uniform foam morphology. In addition to improved foam morphology, superior intrinsic mechanical properties of HNTs provide further enhancement to the mechanical properties of polymer foams by creating perfect nano-reinforcement. Up to now, no fundamental research studies investigating the effect of BTAs and HNTs on the morphology and properties of extruded PBT foams have been performed.

In this context, obtaining low-density mPBT foams (< 80 kg/m^3) via foam extrusion technology based on two different BTAs and HNTs showing enhanced mechanical properties is of interest. This motivates the current study to explore the influence of BTAs and HNTs on the polymer crystallization behavior, melt properties, foamability of mPBT and the resulting foam morphology and mechanical properties.

2 Theoretical Background and Literature Survey

2.1 Classification of Polymer Foams

Polymer foams are classified according to their density, cell structure, cell size, chemical structure, manufacturing method and stiffness [36,37].

Table 1   Classification of polymer foams.

Property	Classification
Density	• high (> 500 kg/m^3) • medium ($200 - 500$ kg/m^3) • low ($50 - 200$ kg/m^3) • ultra-low (< 50 kg/m^3)
Cell structure	• open-celled • closed-celled • mixed-celled
Cell size	• nano-cellular (< 500 nm) • micro-cellular ($0.5 - 30$ µm) • fine-cellular ($30 - 300$ µm) • macro-cellular or conventional (> 300 µm)
Chemical structure	• crosslinked • non-crosslinked
Manufacturing method	• batch foaming • foam injection molding • foam extrusion • bead foaming
Stiffness	• soft • rigid • visco-elastic • integral foam

The properties of polymer foams (e.g., mechanical properties) depend on the properties of the bulk material and these characteristic foam properties. Depending on the application, desired

foam properties can be achieved by tailoring the characteristics of foams (e.g., density, cell structure and size). For instance, foams with high strength and modulus are required for building and construction, furniture, and transportation applications. Foams with high density, rigidity and closed-cell structure are widely used here [2,26]. Medium-density foams are preferred for the packaging, building and construction industry, while low-density foams find many uses in insulation applications. In contrast to closed-celled foams, open-celled foams are softer and more flexible, making them excellent components for the applications such as bedding, seating and sport where superior comfort and cushioning are needed. Furthermore, open-celled foams can be used as acoustical insulation panels as they can absorb sound waves very well [38].

2.2   Fundamentals and Steps of Foaming

A typical foaming process consists of the following five steps, illustrated in Figure 2:

- Mixing of polymer and BA (two-phase system)
- Dissolution and diffusion of the BA in the polymer melt (single-phase system)
- Cell nucleation
- Cell growth
- Cell stabilization

In the beginning, the two-phase system, which is a mixture of polymer melt and BA, is homogenized into the single-phase system by dissolution and diffusion of the BA (Figure 2). Upon introduction of a thermodynamic instability to the single-phase system, cell nucleation, followed by cell growth and stabilization of the cellular structure, occurs [39].

2.2.1   Two-Phase System

With the dosing of the BA in the polymer melt at sufficiently high pressures and certain temperatures (depending on glass or melt temperature of the polymer), the two-phase mixture is obtained. BAs play a crucial role in the foaming process, significantly influencing the final foam properties, such as cell size, cell density, and foam density. BAs are categorized into chemical and physical BAs.
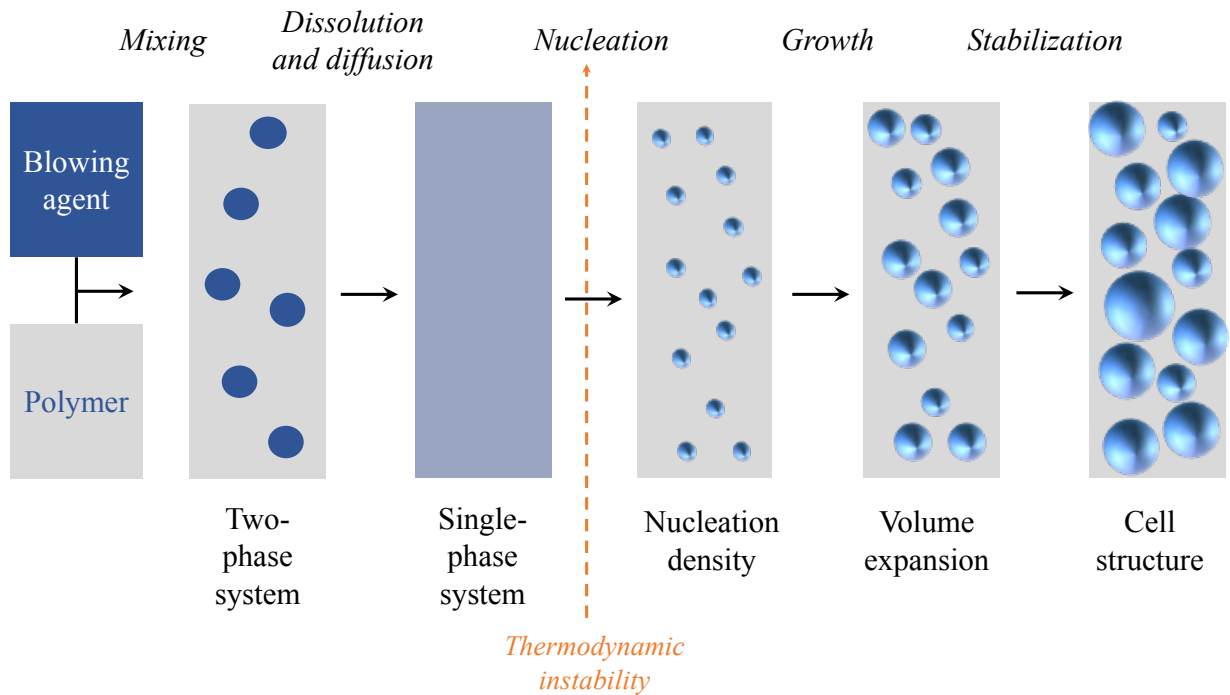
Figure 2 Schematic of the typical foaming process, including different steps for a basic two-phase polymer-gas system. Reproduced from [4].

2.2.1.1 Chemical Blowing Agents (CBAs)

CBAs can either be of organic or inorganic nature, which decompose thermally (exothermically or endothermically) into gases at raised processing conditions. They do not react with the polymer matrix and are responsible for the expansion of the polymer during foaming. The decomposition temperature is the characteristic property of these compounds, and it determines their practical use as BAs for a given polymeric material and processing conditions. Azodicarbonamide and benzene sulfonyl hydrazide (exothermic), sodium bicarbonate and citric acid (endothermic) are some examples of the most frequently used CBA [40]. In general, the foams obtained by using CBAs show non-homogeneous foam morphologies and higher foam densities. Therefore, they are mainly used in foam-injection molding processes to provide a sufficient weight reduction of the injection-molded components.

2.2.1.2 Physical Blowing Agents (PBAs)

PBAs are gases or volatile liquids that evaporate or desorb at certain conditions (e.g., temperature and pressure) featuring the foam expansion. In contrast to CBAs, they do not react or decompose due to their inert nature.

First-generation PBAs, such as hydrochlorofluorocarbons (HCFCs) and hydrofluorocarbons (HFCs), which were commonly used PBAs for foaming, were phased out in 2010 because of their negative environmental impact on the ozone layer [41]. Inert gases like carbon dioxide (CO_2) and nitrogen (N_2), water vapor, alcohols such as methanol, ethanol and isopropanol or low boiling temperature hydrocarbons such as propane, butane and pentane are some examples of today's most used PBAs. Among these, CO_2 is the most preferred PBA for the foam extrusion process due to its benefits, such as being non-flammable, inexpensive, non-toxic, and more environmentally friendly [40,42]. To transform the two-phase mixture into a single-phase system, the injected PBA must remain in the polymer melt, requiring sufficient solubility and diffusivity. However, its relatively low solubility and high diffusivity in most polymer melt as well as high gas thermal conductivity restrict its use as a PBA [40].

To address this, PBAs are often injected in the polymer melt in a supercritical state at high pressures. The required pressure in the extruder ranges from 30 to 100 bar to reach a maximally dissolved BA amount in polymer melt [43]. Supercritical fluids (SCFs) are substances when their pressure and temperature are above the critical borders. SCFs have liquid-like densities that act as excellent solvents, while gas-like viscosities lead to a high diffusion rate. Reduction in viscosity enables the production of microcellular foams [44]. Supercritical N_2, CO_2, water, ammonia, ethane, and methane are examples of SCFs. Among these, supercritical CO_2 (sc-CO_2) has been the most often used BA for foaming since it has a critical temperature of 31 °C and critical pressure of 7.38 MPa, which can be reached easily [45–52].

2.2.2 Single-Phase System

Forming a single-phase system composed of a polymer and a BA is crucial for achieving high-quality polymer foams with a homogeneous cell structure having a narrow cell size distribution. This is controlled by the solubility and diffusion of the BA in the polymer melt. Solubility is

the maximum quantity of BA absorbed by a polymer depending on the solubility limit of the polymer at a particular temperature and pressure. It is obtained from the difference between the amount of gas initially contacted with the polymer and the amount remaining in the gas phase after equilibration, which can be determined experimentally [53–59] or calculated by the equation of state (EOS) under measuring gas pressure and temperature [60,61]. The EOS provides a theoretical estimation of how much BA dissolves in a polymer melt at a given pressure and temperature. When a polymer in which BA dissolves is in a liquid or glassy state, Henry's law relates the gas adsorption pressure p to the concentration of the dissolved gas C_{dis} through Henry's law constant k_H, as shown in Equation 1 [62]:

$$C_{dis} = k_H \cdot p \tag{1}$$

k_H depends on the solubility enthalpy ΔH_s, ideal gas constant R_i, absolute temperature T and the constant $k_{H,0}$. The typical Arrhenius-like dependence is given in Equation 2:

$$k_H = k_{H,0} \cdot e^{-\frac{\Delta H_s}{R_i T}} \tag{2}$$

Solubility is quite significant in the foaming process. It depends on the molecular size, the polarity and the molecular weight of the BA and the free volume of the polymer [63]. Higher BA solubility, meaning greater amounts of BA in the polymer, favors efficient cell nucleation and growth. A certain level of solubility is mandatory for obtaining low-density foams.

Once the gas dissolves in the polymer, gas diffusion starts. The gas molecules are transported by diffusion and stored between the polymer chains. The diffusion is also temperature-dependent and described by Fick`s second law of diffusion, in Equation 3:

$$\frac{\partial C}{\partial t} = D_c \cdot \frac{\partial^2 C}{\partial^2 x^2} \tag{3}$$

where C is the concentration, t is the time for diffusion, x is distance and D_c is the diffusion coefficient of the gas. Latter can be described by an Arrhenius-type equation (Equation 4):

$$D_c = D_0 \cdot e^{\frac{E_A}{RT}} \tag{4}$$

where D_0 is a pre-exponential factor and E_A is the activation energy in diffusion. The diffusion of BA in the polymer also depends on time, temperature, and gas concentration. Since thermodynamic and transport properties, including the diffusion coefficient in the liquid phase, are usually not very sensitive to pressure, the pressure dependence of the diffusion coefficient is neglected [57]. Furthermore, M_w of the BA and the free volume of the polymer affect the diffusion of BA. Higher temperatures and smaller M_w of BA promote an increased diffusion rate of BA within the polymer matrix, which favors faster foam cell nucleation. However, too high diffusivity might result in fine-cell structures as a large amount of BA phases out of the polymer within a short period. This might feature weak cell growth and coarse structures.

In semi-crystalline polymers, sorption and transport of BAs occur in the amorphous parts of the polymer. Crystalline phases act as a barrier for diffusing gas. Therefore, solution and diffusion are affected by the degree of the crystallinity of the polymer [64].

2.2.3   Cell Nucleation and Growth

Cell nucleation is the first and essential step of the foaming process. The phenomenon describes the spontaneous formation of a new and more stable phase (nuclei) within the body of a metastable original phase (polymer melt) induced by thermodynamic instabilities. In the context of polymer foams, the nuclei are referred to as foam cells or bubbles. Depending on the influencing factors and nucleating systems, nucleation type and mechanism show a difference. For example, homogeneous, heterogeneous, mixed-mode, cavity, shear-induced and micro void. Various nucleation types with corresponding nucleation mechanisms are outlined by Ramesh [65]. Among these, homogeneous, heterogeneous, and a combination of the two, namely mixed-mode nucleation, are the three most seen nucleating types for gas-polymer systems. Despite various theoretical models [65–72] proposed over the last several decades, the classical nucleation theory is the most common and successful approach used for modeling cell nucleation and growth in a polymeric matrix [73,74].

2.2.3.1 Classical Nucleation Theory

Classical nucleation theory provides fundamentals of free energy barriers and has been used to predict the rate of cell (nucleus) formation and growth. This enables to tune and engineer polymer foams with smaller cell sizes. In the frame of the classical nucleation theory, the following principles and assumptions have been outlined by Oxtoby [75] and Kumar [76]:

- Phase transitions in fluids occur via nucleation and growth of the cells (new phase) in the polymer matrix (original phase).
- The nucleation probability is a function of the minimum work used to form many nuclei in a polymer melt.
- An energy barrier for nucleation exists. However, this is not valid for every case.
- Nuclei show the same properties as the bulk phase.
- All formed nuclei (cells) possess a spherical geometry with specific boundaries.
- The cell interface is composed of an infinite flat planar surface.
- No kinetic information is considered.

Based on these assumptions, the Gibbs free energy change ΔG, nucleation rate at steady state J_s and nucleation rate at transient state J_t of the cell formation can be expressed by Equations 5, 6 and 7 [65].

$$\Delta G(R) = -\frac{4}{3}\pi R^3 \Delta P + \pi R^3 \gamma_{\alpha\beta} - \Delta V_{free\,vol} \tag{5}$$

$$J_s = Z\beta^* N \cdot e^{\frac{-\Delta G^*}{kT}} \tag{6}$$

$$J_t = J_s \cdot e^{\frac{-t}{\tau}} \tag{7}$$

where R is the apparent radius of the nucleus, ΔP is pressure drop, $\gamma_{\alpha\beta}$ is interfacial energy, $\Delta V_{free\,vol}$ is the change in free volume due to the presence of heterogeneous particles, Z is the Zeldovich non-equilibrium factor, β^* is the rate at which gas molecules are added to the critical nucleus, N is the number of nucleation sites per unit volume, ΔG^* is Gibbs free energy of forming a critical nucleus, k is Boltzmann constant, T is the absolute temperature and τ is the induction period for establishing steady-state nucleation conditions.

According to the classical nucleation theory, foam cell nucleation is classified mainly into two types: (1) homogeneous nucleation and (2) heterogeneous nucleation.

Homogeneous and Heterogeneous Cell Nucleation

Homogeneous cell nucleation occurs with the dissolution of the secondary component (e.g., BA) in a primary phase (polymer melt) to form a stable second phase (gas bubble, cell). In polymer foams, the single-phase system, where homogeneous cell nucleation occurs, is composed of a pure homopolymer and a dissolved BA with a critical amount at which the BA is entirely homogenized. In addition, the system does not contain any immiscible impurities or additives. The nucleation is usually initiated by random fluctuations or changes in temperature or pressure. Unlike homogeneous nucleation, heterogeneous nucleation occurs in the presence of foreign bodies (impurities) or additives. It plays a significant role in polymer foaming as various foreign bodies and additives are ubiquitous in commercial foam products. During heterogeneous nucleation, these external particles act as nucleating agents where cell formation is initiated at the interface of the nucleating agent and the polymer melt [77–79]. In contrast to the assumptions that nucleating sites are smooth and planar surfaces [80,81], the interface of these sites might contain conical pits induced by surface roughness. The crevices on the surface of the nucleating agent enable trapping of the gas (BA) and nuclei formation, as shown in Figure 3.
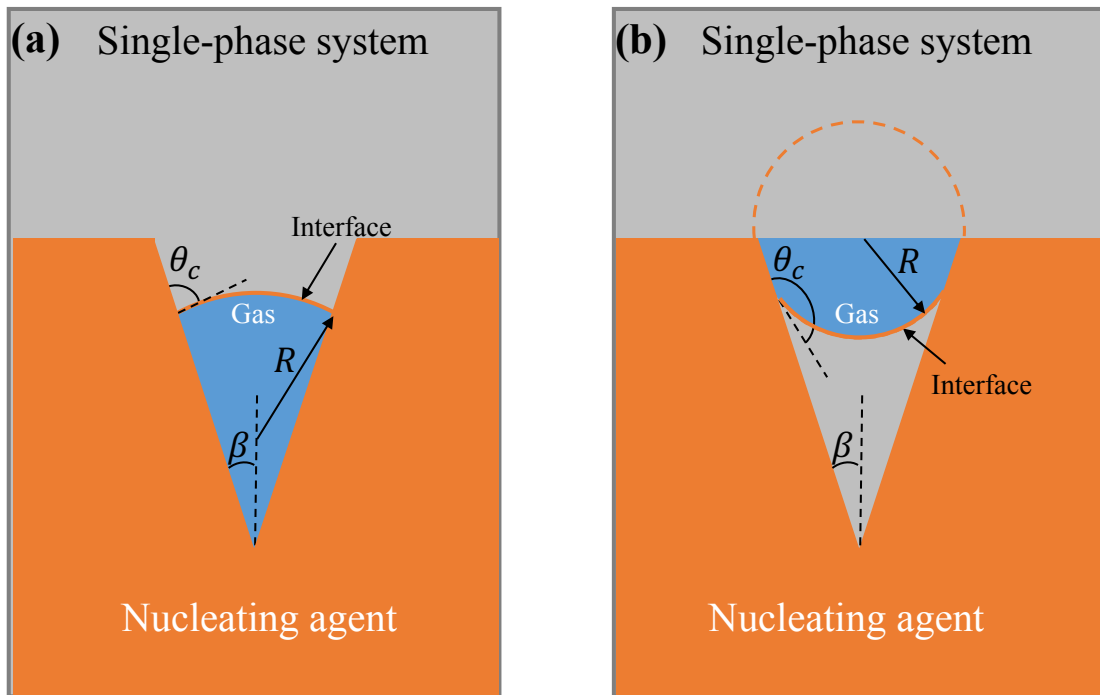
Figure 3 The formation of the nucleus in a conical cavity with (a) a positive radius of curvature and (b) a negative radius of curvature, where R is the radius of the curvature (bubble), θ_c is the wetting or contact angle and β is the angle of the conical cavity of a nucleating agent. Reproduced from [80].

The heterogeneously formed nucleus in a conical cavity can possess either a positive radius of curvature (when $\theta_c - \beta < 90°$) or a negative radius of curvature (when $\theta_c - \beta > 90°$). In homogeneous cell nucleation, nuclei are spherically shaped and always possess a positive radius of curvature. A change of free energy induces the thermodynamic instability for nucleus formation. The relationship between ΔG for the homogeneous or heterogeneous nucleation of a cell with a positive radius and the heterogeneous nucleation of a cell with a negative radius is shown in Figure 4 and Figure 5, respectively.
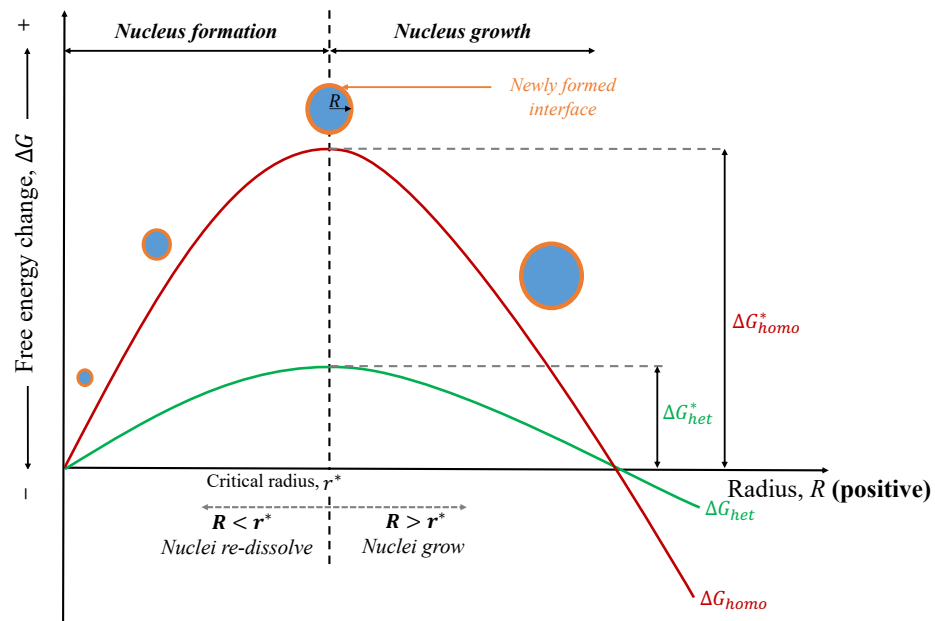
Figure 4   Free energy change for the homogeneous or heterogeneous nucleation of a cell with a positive radius, where r^* is the critical radius. Reproduced from [80,82].
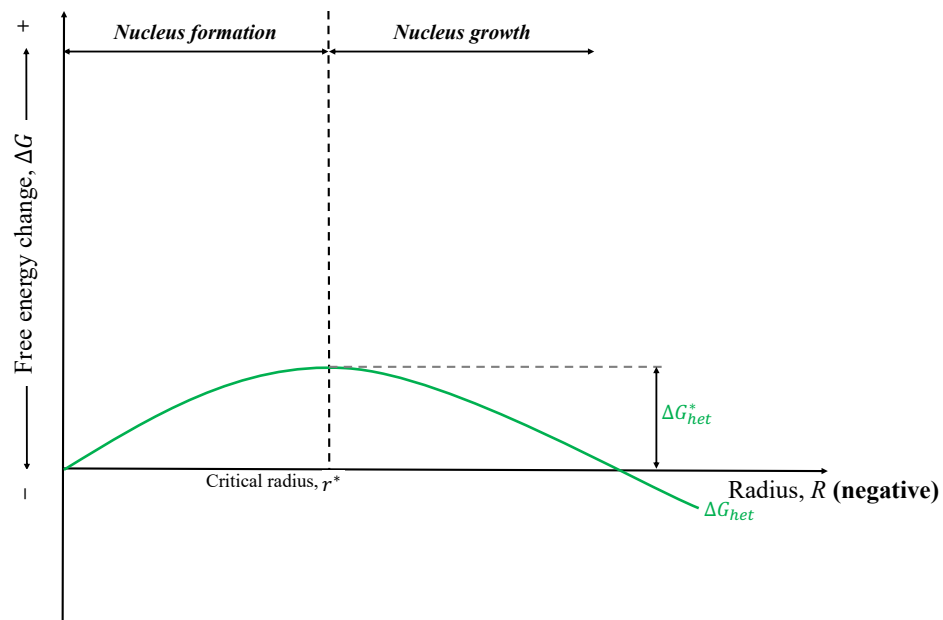
Figure 5   Free energy change for the heterogeneous nucleation of a cell with a negative radius. Reproduced from [80].

In the case of homogeneous cell nucleation and heterogeneous nucleation of a cell with a positive radius (Fig. 3a), once nuclei radius exceeds the critical radius ($R > r^*$), they can irreversibly grow within the polymer melt until it is stabilized. Cell growth occurs when the pressure inside a bubble is higher than the pressure of the medium surrounding it. Oppositely, when $R < r^*$, nuclei re-dissolve into polymer melt and no foam cell is formed (Fig. 4).

In the case of heterogeneous nucleation of a cell with a negative radius (Fig. 3b), the change in free energy reaches its minimum when $R = r^*$, where the nucleus is at a stable equilibrium state. For the formation of a macroscopic cell, an external force (e.g., a shear force) is required to pull out the conical pits of nucleating sites by providing strong fluctuation [83]. As the shear force-induced nucleation is not considered in this thesis, the case of the negative radius of curvature will be neglected.

Heterogeneous nucleation has a lower activation energy barrier than homogeneous nucleation, suggesting that heterogeneous nucleation is energetically more favored. However, r^* for both homogeneous and heterogeneous nucleation is the same, expressed in Equation 8 [65,84,85].

$$r^* = \frac{2\gamma_{\alpha\beta}}{\Delta P} \tag{8}$$

where $\gamma_{\alpha\beta}$ and ΔP are interfacial energy and pressure drop, respectively. Gibbs free energy barrier of forming a critical nucleus in homogeneous nucleation (ΔG^*_{homo}) and in heterogeneous nucleation (ΔG^*_{het}) are given in Equation 9 and Equation 10, respectively [65].

$$\Delta G^*_{homo} = \frac{16\pi\gamma^3_{\alpha\beta}}{3\Delta P^2} \tag{9}$$

$$\Delta G^*_{het} = \frac{16\pi\gamma^3_{\alpha\beta}}{3\Delta P^2} \cdot S(\theta_c,\beta) \tag{10}$$

Both ΔG^*_{homo} and ΔG^*_{het} are dependent on $\gamma_{\alpha\beta}$ and ΔP while ΔG^*_{het} is also a function of the geometric factor of the nucleating agent $S(\theta_c,\beta)$, expressed in Equation 11 [80].

$$S(\theta_c, \beta) = \frac{V_g}{V_{g,spherical}} = \frac{1}{4}\left[2 - 2\sin(\theta_c - \beta) + \frac{\cos\theta_c\cos^2(\theta_c - \beta)}{\sin\beta}\right] \tag{11}$$

where $S(\theta_c, \beta)$ is the ratio of the volume of a heterogeneously nucleated cell V_g to the volume of a spherical cell with the same radius $V_{g,spherical}$. β directly depends on the geometry of the nucleating agents and influences the ΔG^*_{het}. Therefore, nucleating agents, in other words, additives play a significant role in polymer foaming by determining the nucleation mechanism.

The nuclei which exceed the free energy barrier and reach the critical radius, r^* start growing. The cell growth process is induced by further diffusion of the dissolved BA into the stable nuclei. When the energy required for surface expansion equals to the volume work in the growing cell, in other words, when the equilibrium state is reached, the cell growth process stops. The equilibrium can be described mathematically with the help of Equation 12:

$$\gamma \cdot dA = p_1 \cdot dV \tag{12}$$

where γ is surface tension, A is surface area, p_1 is the partial (internal) pressure and V is the volume of the bubble.

It is assumed that a single growing foam cell has a spherical geometry and is representative of all other growing cells in the polymer-gas mixture. Based on these assumptions and Equation 12, Equation 13 can be derived.

$$\gamma \cdot 8\pi r \cdot dr = p_1 \cdot 4\pi r^2 \cdot dr \tag{13}$$

$$p_1 = \frac{2\gamma}{r} \tag{14}$$

According to Equation 14, the internal pressure is higher in small cells than in large cells. In real systems, walls of the bubbles having different sizes contact each other. The higher internal pressure of small foam cells causes the gas to diffuse into larger cells, whereby large cells continue to grow, and small ones disappear. This results in relatively coarse-celled, inhomogeneous foam morphology that is not desirable. The rate of gas diffusion (w) into the bubble is described by Stoke`s law, given in Equation 15:

$$w = \frac{g \cdot (2r)^2}{18\eta} \Delta\rho \tag{15}$$

where g acceleration of gravity, η is dynamic viscosity and $\Delta\rho$ is the change in density of the bulk material. To reduce the coarsening of the cells, it is necessary to increase the melt viscosity. This can be achieved, for example, by increasing the molecular weight of the polymer via long-chain branching or by reducing the gas load [37,86,87].

The mechanisms of homogeneous cell nucleation and heterogeneous cell nucleation and growth in the presence of nucleating agents are summarized schematically in Figure 6.
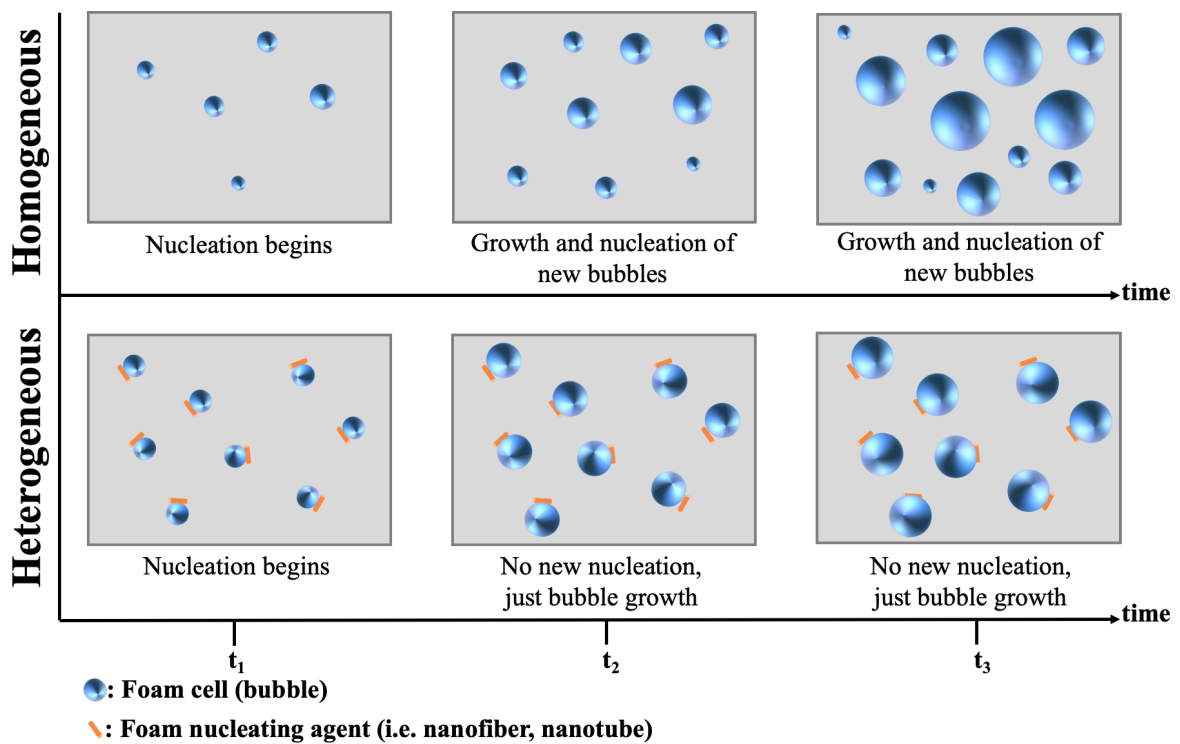
Figure 6   Schematics of the progress of homogeneous and heterogeneous cell (bubble) nucleation and growth. Reproduced from [88,89].

2.2.4 Cell Stabilization

After the nucleation and growth steps, the fixation of the foam cell structure is crucial to avoid cell collapse or coalescence. This can be induced by decreasing the melt temperature lower than the gas-polymer system's effective glass transition temperature (T_g). As soon as foaming starts, the gas solubility in the melt changes due to temperature and pressure drop. This causes T_g to increase very quickly. Due to the significant increase in melt viscosity upon cooling and the change in T_g, the pressure inside a cell is no longer sufficient for further expansion. In addition, the diffusion speed of the gas decreases due to the higher viscosity and the decreasing gas concentration in the polymer melt. The stabilization of the cell structure takes place after pressure is dropped at the end of the stage. For example, at the die in the foam extrusion process. The pressure drop results in outgassing of the BA from the cells and is replaced by ambient air [37,86,87,90].

2.3 Role of Nanoadditives as Foam Cell Nucleating Agents

Nanoadditives (nanofillers) are materials with a geometric size of less than 100 nm in at least one dimension. These nanoadditives, mixed and dispersed in a polymer matrix, play a significant role as heterogeneous nucleating agents in foaming due to their high specific surface areas featuring many heterogeneous nucleation sites. Their shape and dimensions differ depending on their characteristic length (L) and diameter or thickness (D). L over D ratio of the nanoadditive is defined as aspect ratio. Figure 7 demonstrates typical geometries of nanoadditives.
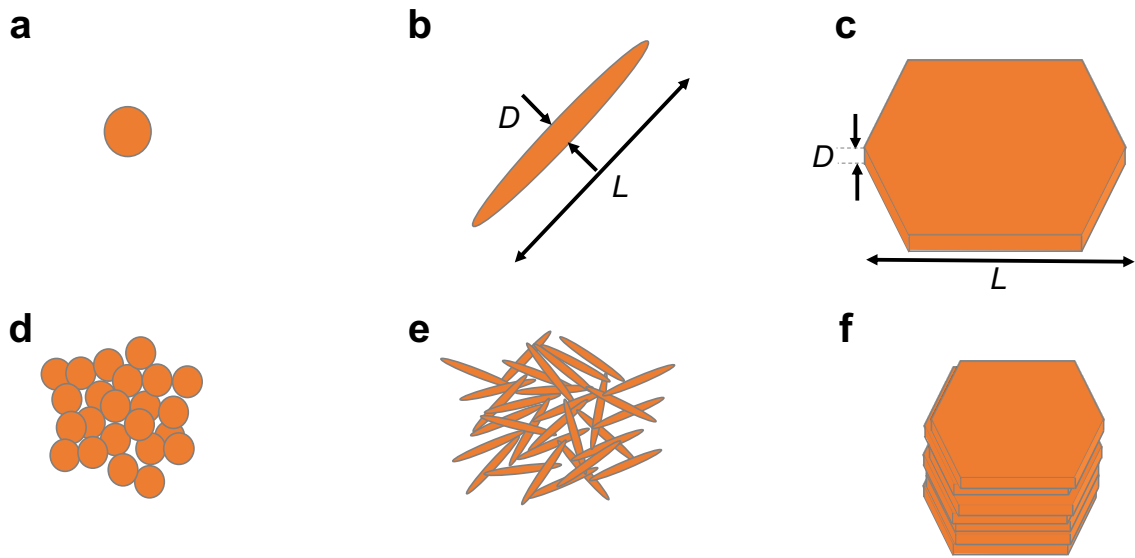
Figure 7 Various shapes of nanoadditives. (a) nanoparticle, (b) nanorod (or nanotube, nanofiber, etc.), (c) nanoplatelet (or nanosheet, nanoflake, etc.), (d-f) secondary particles or aggregate forms of each nanoadditives. L and D represent the characteristic length and diameter/thickness of the nanoadditives, respectively [91].

Besides their shapes, depending on their dimensions, nanoadditives are mainly classified into four categories, namely zero-dimensional (0D), one-dimensional (1D), two-dimensional (2D) and three-dimensional (3D) [92].

- 0D nanoadditives: All three dimensions < 100 nm (e.g., nanoparticles)
- 1D nanoadditives: Two dimensions < 100 nm while one dimension > 100 nm (e.g., nanofibers, nanorods or nanotubes)
- 2D nanoadditives: One dimension < 100 nm while the other two dimensions >100 nm (e.g., nanoplatelets, nanosheets or nanoflakes)
- 3D aggregates of nanoadditives: All three dimensions > 100 nm (e.g., secondary particles or aggregate forms of nanoadditives such as bundles of nanorods, nanofibers or nanotubes)

In addition, nanoadditives can be made of organic, inorganic, and metallic materials. In this study, organic and inorganic nanoadditives are mainly focused.

- Organic nanoadditives: Composed of organic components (e.g., polymer nanofibers such as PTFE or in-situ fibrillated and supramolecular polymer nanofibers)
- Inorganic nanoadditives: Composed of inorganic substituents (e.g., carbon-based such as graphene, expanded graphite, carbon black, CNFs and clay-based nanoadditives such as nanosilica, layered-nanosilicates and HNTs)

Geometries, including dimension and aspect ratio, shapes, and chemical compositions of the nanoadditives in the polymer matrix, determine their interaction with polymer and thus interfacial area, dispersion, foam nucleation efficiency and thus foam morphology and properties.

2.3.1 Organic Nanoadditives

The successful use of organic nanoadditives as foam nucleating agents in various semi-crystalline polymers has already been reported [21,22,24,26,93]. Rizvi et al. [93] prepared in-situ fibrillated blends of PP/PTFE, in which PTFE elongates into nanofibrillar structures having diameter less than 500 nm and length exceeding 100 mm. It was claimed that 0.3 wt% PTFE in a PP foam leads to reduced cell size and a ten-fold expansion ratio compared to the neat PP foam [93]. In-situ fibrillated polymer fibers such as PET, having the aspect ratio of 190 and average diameter (d_{avg}) of around 163 nm, with a concentration of 5 wt% resulted in PP foams with three orders of magnitude increased cell density and 15 times higher expansion ratio [22]. In another study of [22], in-situ fibrillated PP fibers (5 wt%, $d_{avg} = 100 - 300$ nm, aspect ratio $=> 200$) were used as foam nucleating agents to improve foamability and foam morphology of PE foams. Although in-situ fibrillated polymer fibers play a beneficial role as foam nucleating agents, reducing cell size, increased expansion ratio, and homogeneous foam morphology, their three-step manufacture is not time and cost-effective [22].

In contrast, foams nucleated by soluble organic nanoadditives, such as supramolecular nanoadditives, can be produced in only one step. Processing conditions (e.g., temperature and cooling rate of the polymer melt), polarity, chemical nature, and concentration of the nanoadditive affect the solubility (intimate mixing) of the molecules in the polymer melt and their self-assembling behavior. Therefore, by tuning these parameters, the geometry and dispersion quality of the nanoadditives, which are formed by self-assembly, can be controlled. As a result, controlled foam cell nucleation, resulting in improved foam morphology with

smaller mean cell size and narrower cell size distribution as well as greater cell density, is achieved [26,94,95].

Supramolecular Nanoadditives

A new class of organic nanoadditives, so-called supramolecular nanoadditives, has gained significant interest in literature as a potential alternative nucleating agent. Unlike conventional in-situ fibrillated polymer nanofibers consisting of covalent bonds, supramolecular nanoadditives are polymeric arrays of organic molecules (monomers), such as 1,3,5-benzenetrisamides (BTAs), held together by highly directional and reversible secondary interactions [96]. In general, the self-assembly from monomers to a high-molecular-weight polymer by the non-covalent interactions is defined as supramolecular polymerization. Synthetic cooperative supramolecular polymerizations are enthalpically driven and occur upon cooling [97]. The directionality of the secondary interactions determines the 1D nature of supramolecular polymers, which distinguishes them from 3D molecular polymers.

On the other hand, the reversibility of the non-covalent bonds ensures that supramolecular polymers are always formed under thermodynamic equilibrium conditions. Hence, the length of the polymer chains or the degree of polymerization can be adjusted by the strength of the non-covalent bond, the concentration of the monomer, association constant, temperature and the purity of the monomers [96]. This reversibility explains the strong dependence of the melt viscosities on temperature, that is, a considerable reduction in viscosity resulting from a minimal increase in temperature above T_g. Supramolecular polymer chains can break and then recombine with other strain-free chain-ends to release stress under high temperatures, while conventional polymers use reptation to achieve stress relaxation [96].

Four typical secondary interactions are acting as driving forces for the formation of supramolecular assemblies: (1) hydrogen bonding, (2) $\pi - \pi$ interactions, (3) hydrophobic interactions and (4) metal-ligand binding [98]. Although hydrogen bonds between neutral organic molecules are not the most robust non-covalent interactions, they are among the most studied non-covalent interactions in supramolecular chemistry because of their directionality and versatility [99].

1,3,5-Benzenetrisamide (BTA)-Based Supramolecular Nanofibers

BTA-based supramolecular nanofibers are a relatively new category of nanoadditives, having attracted attention as crystal and foam nucleating agents for semi-crystalline thermoplastics [26,100–102]. Depending on the temperature and concentration, BTAs can dissolve in the polymer melt and thus are intimately dispersed at the molecular level. Figure 8 shows the general chemical structure of BTA-based molecules, composed of one aromatic core and three amide groups, surrounded by nonpolar substituents.
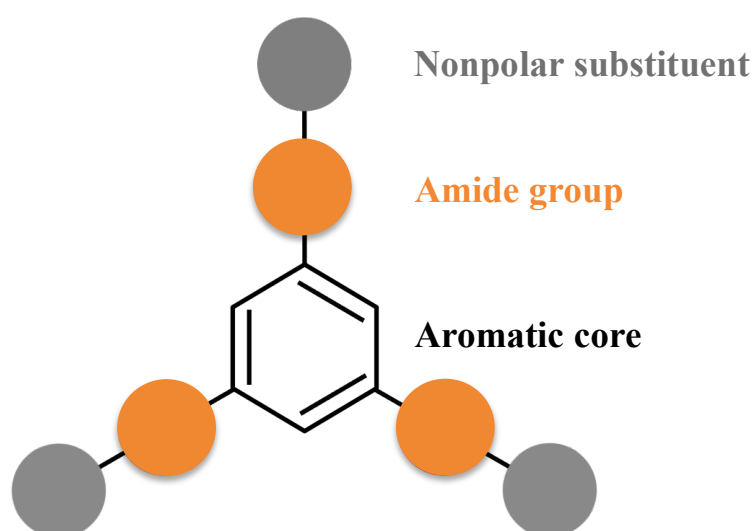
Figure 8 General molecular structure of BTA molecule.

The aromatic core benzene ring is connected to a nonpolar substituent at 1-, 3- and 5-positions through amide groups. The amide groups can form hydrogen bonds, while the nonpolar substituent, on the one hand, controls the solubility of the additive in the polymer and, on the other hand, influences the crystal structure of the additive. The amide group can be attached to the benzene ring either with the carbon atom or the nitrogen atom [103].

Similar to discotic liquid crystals, upon cooling, individual molecules of BTAs can be stacked above one another while rotating by 60° to the previous molecule due to intermolecular forces. This results in columnar stacks with a helical structure [104,105]. Figure 9 illustrates a small section of such a stack and the way how they arrange by three directed hydrogen bonds

(between hydrogen and oxygen atoms) among amide groups and $\pi - \pi$ stacking among aromatic benzene rings from side-view (Fig. 9a) and top-view (Fig. 9b).
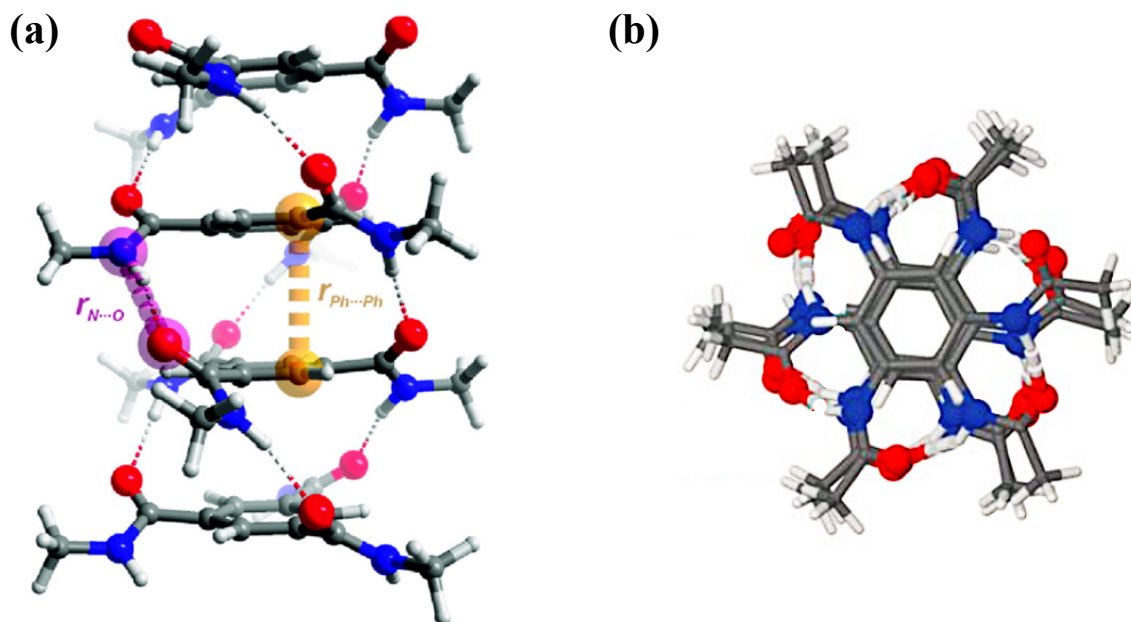
Figure 9   A section of a columnar stack of BTA molecules self-assembled via hydrogen bonding (H-bonding) and π-π interaction (a) side view, (b) top view. Reproduced from [106].

These columnar stacks further self-assemble into very finely dispersed and highly ordered fibers having diameters on the nano and mesoscale (from 45 nm to 5 µm) [107]. The self-assembly behavior of BTAs in a polymer melt upon cooling is illustrated in Figure 10.
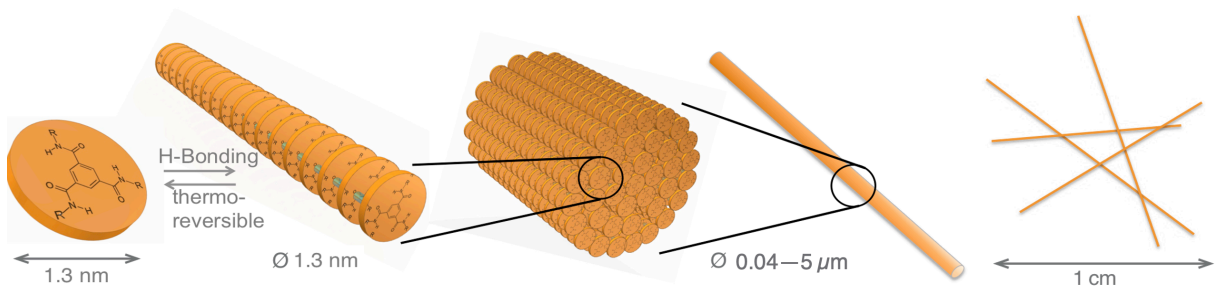
Figure 10   Schematic illustration of the self-assembly behavior of BTAs in a polymer melt. Reproduced from [108].

Under suitable cooling and processing conditions, the length of the BTA fibers can reach dimensions of several centimeters. Due to their corrugated surface and high surface-to-volume ratio, homogenously dispersed BTA nanofibers can act as effective nucleating sites for both polymer crystal and foam cell nucleation in semi-crystalline polymers [26,109]. For instance, in the presence of BTA nanofibers, i-PP crystallites grow and orientate themselves perpendicular to the nanofiber surface. The bulky and stiff substituents of BTA provide a well-defined solid surface with the ability to induce polymer crystallization on that surface, leading to an increased crystallization temperature and reduced crystallite size [100].

Aside from polymer crystal nucleation, the high quantity of nucleating sites, given by the large surface area of BTA nanofibers, contributes to reducing the free energy barrier of the foam cell nucleation. Therefore, heterogeneous cell nucleation is supposed to start on the surface of the BTA nanofibers. The use of BTAs as a foam cell nucleating agent was reported by Stumpf et al. for the first time [94]. In the presence of BTAs, injection-molded i-PP foams were showed to have an improved morphology compared to the neat i-PP foam. BTA nanofibers resulted in a reduced mean cell size (from 120 to 20 µm) and four orders of magnitude increased cell density (from 10^5 to 10^9 cells/cm³).

In another study [26], BTA-based i-PP foams were produced by a tandem foam extrusion line. It was reported that BTA objects provided a large surface and higher number of nucleating sites leading a finer and more homogenous foam morphology. Figure 11 shows the morphological difference of the neat extruded i-PP foam and i-PP foam with 0.4 wt% BTA including corresponding foam densities and cell sizes.
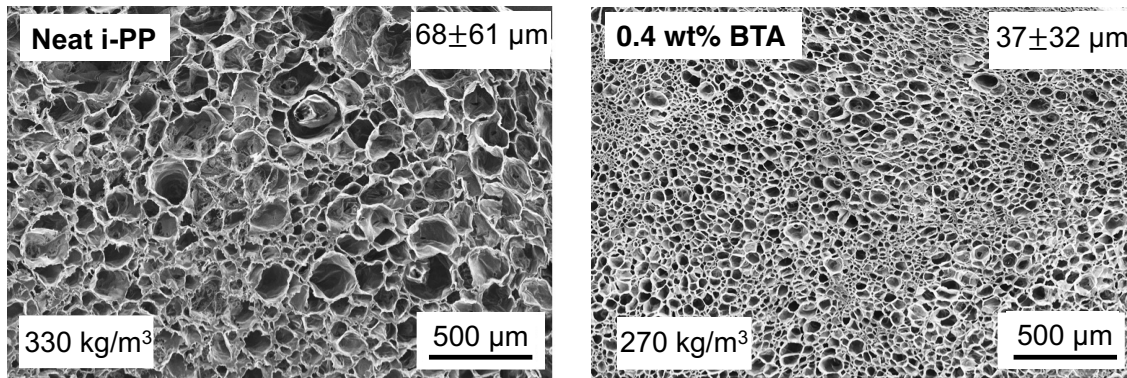
Figure 11 The SEM images of extruded neat i-PP foam and i-PP foam with 0.4 wt% BTA. Reproduced from [26].

As seen in Figure 11, addition of 0.4 wt% BTA in i-PP foam featured a significant cell size reduction from 68 to 37 μm at the similar foam densities showing the important role of BTA nanofibers as a foam nucleating agent.

A further study [95] was accomplished on amorphous PS to understand the effect of BTA nanofibers on the morphology of extruded-PS (XPS) foams. Figure 12 exhibits the morphological overview of the neat XPS foam and XPS foams including various concentrations of BTAs together with corresponding foam densities. BTA nanofibers in XPS featured a significant decrease (by a factor of 35) in mean cell size from 632 to 18 μm compared to those of a neat XPS foam. 0.5 wt% BTA led to slight increase in cell size which was attributed to larger aggregates of BTA nano-objects due to the limited solubility of BTA in PS melt at the processing conditions. Furthermore, the foams with BTA possessed the density in the range of 69 – 78 kg/m³ while the neat one had 52 kg/m³ which might be due to the increased cell density induced by BTAs.
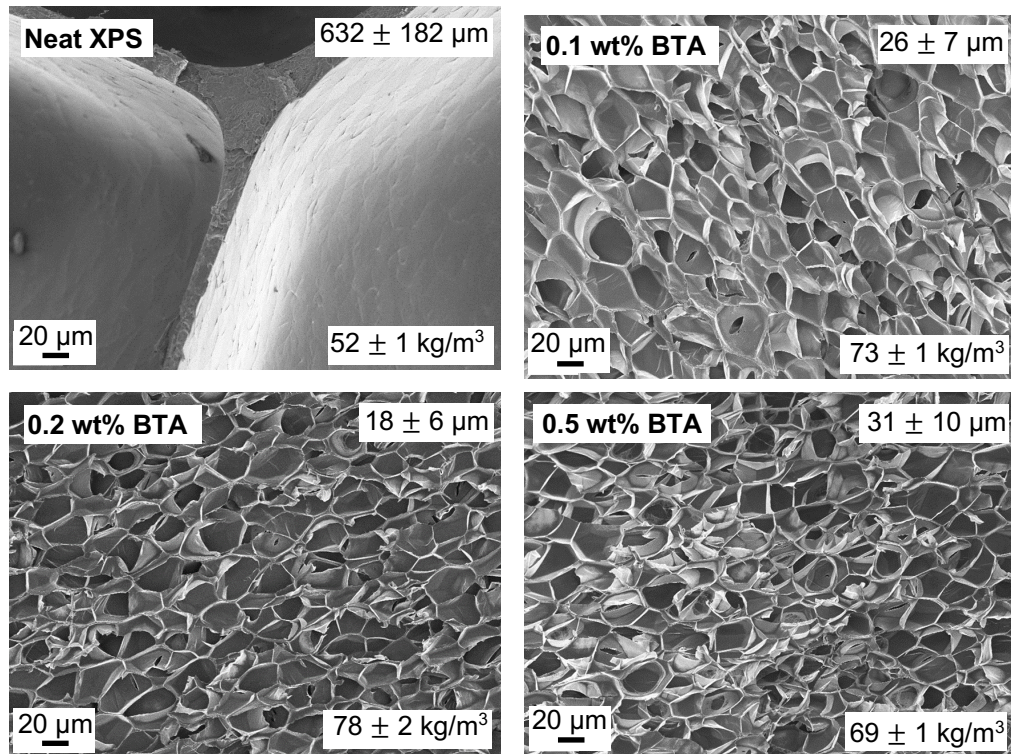
Figure 12 The SEM images of extruded neat XPS foam and XPS foams with various concentrations of BTA. Reproduced from [95].

Beside morphology, BTA nanofibers play a significant role in increasing the mechanical performance of XPS and extruded i-PP foams. Yet, the influence of BTA nanofibers on mechanical properties of foams will be discussed in *Chapter 2.5.4.*

2.3.2 Inorganic Nanoadditives

As organic nanoadditives, inorganic nanoadditives are also widely used as foam nucleating agents, increasing the number of sites for cell nucleation due to their high surface-to-volume ratio [110–112]. Inorganic nanoadditives can be mainly divided into two categories: (1) Carbon-based nanoadditives such as thermally-reduced and functional graphite oxide [113,114] expanded graphite [111], multi-walled carbon nanotubes (MWCNT) [110,115], carbon nanofibers (CNFs) [116] and (2) clay-based nanoadditives such as nanosilica [117],

layered-silicates [28,30,31] and HNTs [29]. For instance, Acuña et al. [118] reported that 6 wt% expandable graphite with the particle size of 300 μm led to a 34 % decrease in cell size of a PUR foam, showing graphite's role as a foam nucleating agent. In another study, Zhao et al. [119] produced microcellular PP foams via batch foaming in the presence of multi-walled carbon nanotubes (CNTs) with the surface area, mean diameter and mean length of 250 – 300 m^2/g, 9.5 nm, and 1.5 μm, respectively. It was found that compared to the neat PP, the cell size of PP foams with 5 wt% CNT was reduced by 49.7 % (smaller than 30 μm). Aside from their successful use as cell nucleating agents for semi-crystalline foams, carbon-based nanoadditives show some drawbacks, such as being high in cost, hazardous to human health, and handling difficulties during processing. In contrast, clay-based nanoadditives are naturally occurring, non-toxic, biocompatible, are safe in various fields and easy to handle during processing [120]. Due to their abundance and lower price, they are a good alternative for carbon-based nanoadditives for foaming applications where cost sensitivity is a concern [121]. It has been proven that finely dispersed clay-based nanoadditives can reduce the cell size and increase the cell density as they can act as sites for bubble nucleation. For example, Di et al. [122] showed that with 5 wt% organoclay, the cell density of PLA foam was increased from 0.008×10^8 cells/cm^3 to 5.1×10^8 cells/cm^3. Hwang and Hsu [31] showed that 4 wt% nanosilica led to a significant cell size reduction to 20 μm in injection-molded PP foams. Furthermore, the great potential of HNTs as foam nucleating agents at small concentrations (< 1 wt%) for PLA foams was reported [33]. It was claimed that compared to the neat PLA foam, a significant weight reduction ($\approx$ 15 %) and a decrease in cell size ($\approx$ 42 %) are achievable with 0.5 wt% HNT.

Halloysites

HNTs are naturally existing, kaolinite-based one-dimensional inorganic clay nanotubes, with the chemical formula $Al_2Si_2O_5(OH)_4 \cdot nH_2O$. Their structural design is depicted in Figure 13.

(a) TEM image of Halloysite

100 nm

(b) AFM image of Halloysite

Layer A
Interlayer Space
Layer B

Siloxane Surface (Outer)

Magnification

Aluminol Surface (Inner)

(c) Halloysite Nanotube

Siloxane Network

Aluminol Network

Water Molecules

Inner surface OH
O atom
Si atom

Inner OH
Al atom
H_2O molecule
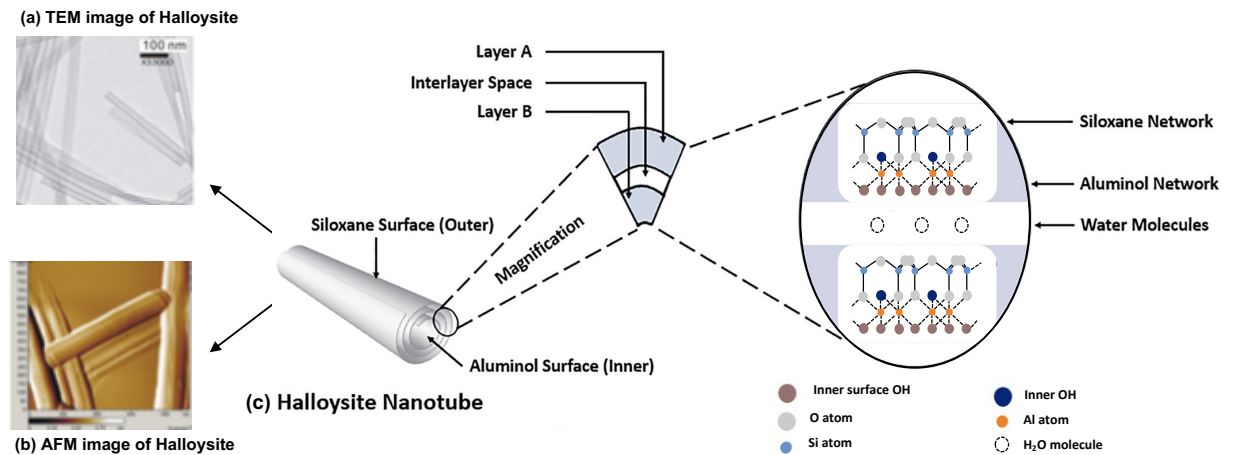
Figure 13   Images of HNTs by (a) Transmission Electron Microscopy (TEM) and (b) Atomic Force Microscopy (AFM). Reproduced from [123]. (c) Schematic representation of the rolled structure of halloysite (Left). Schematic illustration of the crystalline structure of halloysite (Right). Reproduced from [124].

The hollow nanotubular structure consists of siloxane (Si-O-Si, outer), aluminol (Al-OH, inner) surface and 10 to 15 bilayers with an interlayer space of around 0.72 nm (Fig. 13c). They have an aspect ratio of around 20 and a density of around 2.53 g/cm^3 [124,125]. The length of HNTs commonly ranges from 0.2 to 1.5 µm. A length up to 5 µm can also be seen in some deposits. The inner and outer diameters are generally in the range of 10 – 30 nm and 40 – 70 nm, respectively [126–128]. This geometry qualifies HNTs as a perfect cell nucleating agent and nano-reinforcement for cellular foams. Their abundance in nature, high aspect ratio, modulus and economic viability widen their applications. For instance, in porcelain production as a whitening agent to reinforce polymers, crystal nucleation, flame retardance, catalysis or extended-release of active ingredients in medical applications [c]. In addition, their unique nanotubular and porous shape with sharp edges, high surface area and aspect ratio make HNTs an excellent candidate as foam cell nucleating agents like other mineral-based inorganic

additives such as talc and calcium carbonate. The following benefits of HNTs give an insight into their tremendous potential compared to the other available additives:

- Compared to the other mineral-based additives (e.g., talc and calcium carbonate), HNTs possess a lower density (2.14-2.59 g/cm^3) due to their porous structure with a lumen space in the range of 10.7 to 39 % [129,130]. This is crucial in producing lightweight polymer composites and foams as materials with lower densities are desired.
- The unique tubular structure and surface of HNTs enable plenty of possibilities for post-modification, leading to enhanced dispersion quality in the polymer matrix [131]. This is important for avoiding the re-agglomeration, a common problem of insoluble additives, leading to an inhomogeneous foam morphology and deteriorated properties.
- Due to its fine particle size and asymmetrical geometry with sharp edges and high surface area, lower amounts (< 1 wt%) are adequate to tune the polymer crystallization behavior of polymer (e.g., Polyamide), while simultaneously increasing stiffness and strength. Although the aspect ratio of talc and glass fibers is very similar to HNTs, the latter only require lower amounts to reach the same level of reinforcement [c].
- Compared to hazardous carbon-based additives such as CNFs and MWCNTs, HNTs are natural materials with proven biocompatibility and non-toxicity as well as more and easy to process [120]. Furthermore, HNTs are a member of the green and non-hazardous nanomaterials listed by the environmental protection agency (EPA 4A) [132].
- Due to its abundance and low price (at about 4 $/kg at year 2008), HNTs seem to be a good substitute for carbon-based (at about 500 $/kg at year 2008) and BTA-based (at about 300 $/kg at year 2014) additives within the challenging price environment of the polymer foam market [121] .

To the best of my knowledge, using HNTs as a foam cell nucleating agent for thermoplastic polymer foams in the literature is rare [29,33–35].

Wu et al. [29] prepared PLA/HNT nanocomposite foams with HNT concentrations of 1, 3, 5 and 7 wt% via batch foaming process. It was found that the best HNT dispersion quality was provided at 5 wt% HNT, leading to the smallest mean cell size of around 6 μm and narrowest cell size distribution. Further increase in HNT content to 7 wt% caused a broadened cell size distribution with a smaller cell density of only 1.16×10^9 cells/cm^3. This was attributed to bubble coalescence close to HNT agglomerates because of the high concentration. Neither foam density nor volume expansion ratio of the foams was provided by the researchers.

The morphological overview of PLA foams including various HNT concentrations are shown in Figure 14.
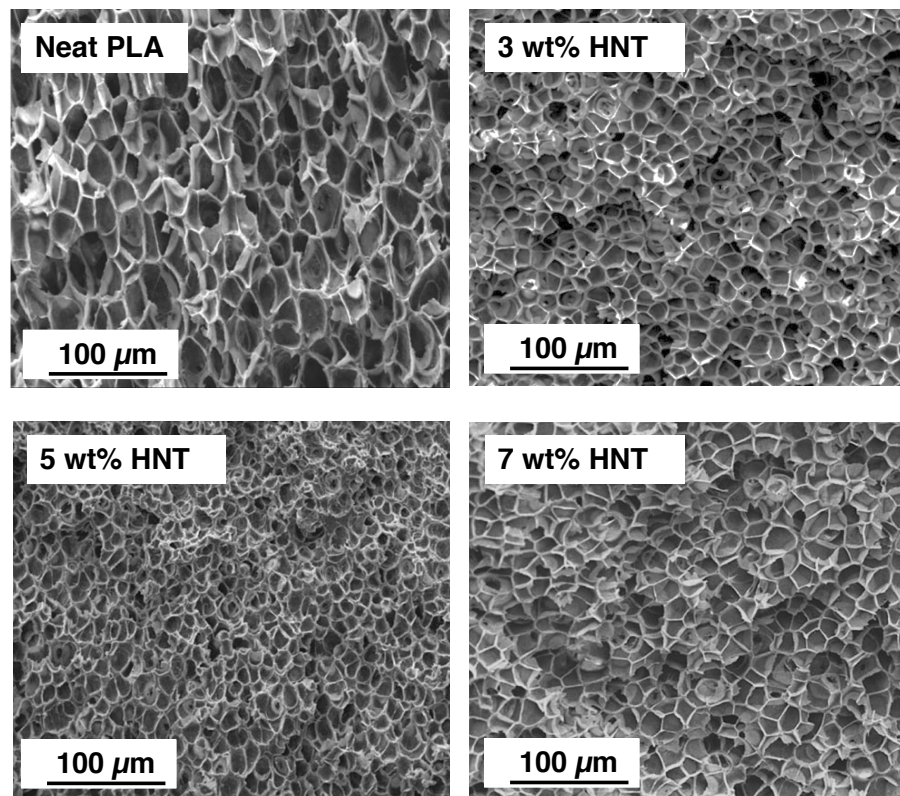
Figure 14   The SEM images of extruded neat PLA foam and PLA foams with various concentrations of HNT. Reproduced from [29].

In another study [35], the authors produced PBS nanocomposite foams, including the same HNT concentrations (1, 3, 5 and 7 wt%). Nanocomposite foams were foamed by using a pressure quenching method (pressure-induced batch foaming) with sc-CO_2 as a physical blowing agent. Like PLA/HNT nanocomposite foams, 5 wt% HNT was found to be the optimum concentration, giving the best dispersion quality and heterogeneous cell nucleation efficiency. Thus, foams with the finest cell size of around 13 μm, the highest cell density of 2.17×10^8 cells/cm^3 and the narrowest cell size distribution were achieved. The authors also reported that 5 wt% HNT provided the largest volume expansion ratio of 5.7. It was supposed that due to their large aspect ratio, HNT nanoadditives decrease the activation energy for cell nucleation. Therefore, they serve as foam cell nucleating agents by increasing the number of nuclei during the foaming. Further increase in HNT content resulted in a higher viscosity of PBS and thus retarded cell growth as well as cell coalescence.

Demori et al. [34] produced injection-molded foams of neat PP, PP/long-chain branched PP (LCBPP) (100/20) blend and nanocomposite foams based on PP, PP/LCBPP and HNTs with

0.5 and 3 parts per hundred of resin (phr). LCBPP was used to increase the melt strength of PP by strain hardening of the melt leading to improved foamability. It was claimed that only small HNT contents enhance the foamability and foam morphology of the nanocomposite foams.
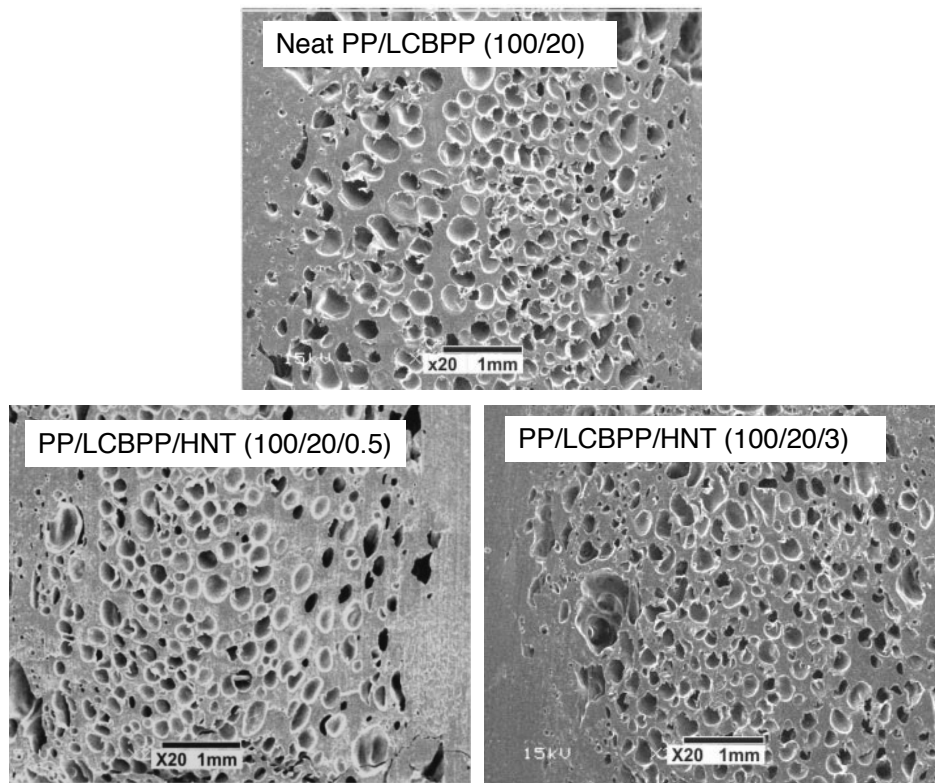
Figure 15 The SEM images of neat PP/LCBPP 100/20 foam and PP/LCBPP foams with 0.5 and 3 phr HNT. Reproduced from [34].

The addition of 0.5 and 3 phr HNT featured an 85 % and 140 % increase in cell density of PP/LCBPP/HNT nanocomposite foam compared to the neat foam based on PP/LCBPP blend (100/20), respectively. This was explained by well-distributed HNTs in the polymer matrix, which was observed by TEM analysis.

Apart from morphology, HNTs show great potential in increasing the mechanical performance of foams. The influence of HNTs on mechanical properties of foams will be discussed in *Chapter 2.5.4.*

2.4 Reactive Foam Extrusion Process

Foam extrusion is a continuous process consisting of either one single-screw extruder or two extruders connected in series (tandem-extrusion line) [43]. Compared to the single-extrusion line, the tandem extrusion line is more commonly used in industrial-scale processes, in which improved dispersion of blowing agent, chain extender and nanoadditives is essential. They are beneficial in terms of process technology, as they offer high throughputs. Different tasks, such as melting, dispersion, dissolution, homogenization, degassing and post-modification reactions (e.g., long-chain branching of polymer), can be combined in a single melting process. The first extruder (A-extruder) serves as a melting and mixing extruder. The post-modification reactions start in this extruder under certain temperature and pressure. It can be either a single- or twin-screw extruder depending on resin formulation and properties of the end product. The second extruder (B-extruder), which serves as a cooling extruder, is a single-screw extruder with a large cylinder diameter to cool the melt as fast as possible. Two separate phases of melting/mixing and cooling phase make the process versatile and easily controllable. The second extruder enables to cool the polymer melt to the desired temperature range for foaming. Reduction in throughput rate in B-extruder is usually required to reach the decreased melt temperatures featuring a pressure build-up, which is crucial for nucleation of foam cells [133,134]. Although the used second extruder is not feasible due to higher investment costs, it provides a rapid and uniform cooling of the polymer melt at higher throughputs than the single-extrusion line, leading to foams with satisfactory quality for diverse applications.

In the light of the processing issues, the general steps of a tandem-reactive-foam extrusion process (illustrated in Figure 16) can be described as follows:
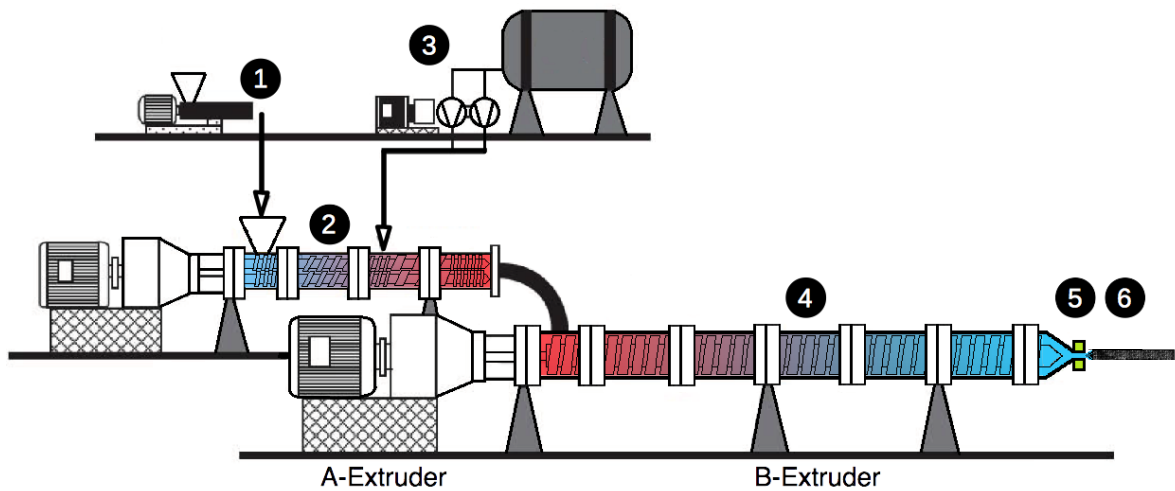
Figure 16 Illustration of a conventional tandem-reactive-foam extrusion line composed of a (1) dosing unit, (2) A-extruder (twin-screw extruder), (3) gas (PBA) injecting unit, (4) B-extruder (single-screw extruder), (5) die with different geometries and (6) foam. Reproduced from [108].

1. The process starts with dosing the materials such as bulk polymer, additive, nucleating agent, filler, chain extender or CBA (in the form of granulate and/or powder) into the A-extruder.

2. With the help of rotating screws, materials are transported from metering to melting zone where heated barrels, shear forces and high-pressure result in polymer plasticization.

3. PBA (e.g., sc-CO_2) is injected into the plasticized melt (with a noticeable pressure built-up) via an injecting unit mounted on the barrel. With the dissolution of the PBA in the melt in the barrel of the A-extruder, a homogeneous, single-phase system is formed. If CBA (instead of PBA) exists in the polymer melt, at specific temperature and pressure, the CBA decomposes within the melt upon gas formation where a single-phase system is formed under suitable processing conditions.

    In the case of a single-line foam extrusion, the process is ended with the cooling and transfer of the single-phase system into the die. In a tandem-extrusion line, the single-phase melt is conveyed into the cooling extruder, namely B-extruder.

4. In the B-extruder, the single-phase system is cooled gradually to a temperature range that is required for optimal foaming. B-extrusion increases the residence time and

further homogenization of the melt system leading to continuity of post-modification reactions, which already started under specific temperature and pressure conditions in the A-extruder. The polymer melt in the A- and B-extruder is subjected to shear deformations due to the melting, homogenizing, conveying and plasticizing at shear rates from 100 to 1000 s^{-1} [39].

5. At the die, which can possess different geometries, such as round and slit, a pressure drop introduces a thermodynamic instability leading to foam cell nucleation and growth until the equilibrium state is reached. During cell nucleation and growth, aside from shear deformations, elongational and mainly extensional deformations occur. This results from the internal gas pressure of the foam cells featuring a biaxial expansion of the cell walls. This deformation occurs at expansion rates of 1 to 5 s^{-1} for a short period of around 2 s [39].

6. Subsequently, foam cell stabilization occurs with further cooling of the system (lower than effective T_g).

2.4.1 Effect of Melt Temperature

T_m is defined as the temperature of the foaming extrudate upon exiting the die. A too high T_m leads to rapid expansion and highest melt opening angle (α) of the extrudate close to the die exit, which can be defined as die (extrudate) swell, following by foam contraction. This results in foam extrudates having a bigger cross-section diameter (d) right after passing the die than the final extrudate (Fig. 17a). This can be explained by the "gas loss" phenomenon. As the diffusivity of BA in a polymer melt increases with increasing T_m, an easy escape of gas from the foamed extrudate is favored. Due to the high expansion ratio close to the die, thin cell walls lead to a higher gas transport rate among the cells, contributing to quicker gas escape from the foam. This results in cell coalescence and thus higher final foam densities as the amount of BA available for the cell growth is significantly reduced. In addition, a high T_m results in lower melt viscosity and strength, which also promotes cell coalescence as cells nucleated by the polymer melt with low melt strength tend to fuse together. Cell coalescence among adjacent cells occurs as cells tend to lower the total free energy by reducing their surface area.
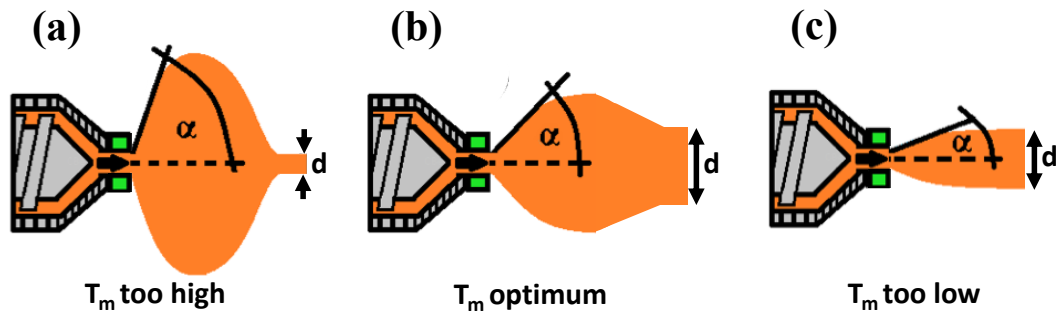
Figure 17 Effect of T_m on the foamed extrudate shape at constant die temperature. When T_m is (a) too high, (2) optimum, (3) too low. α is the melt opening angle and d is the final extrudate cross-section diameter. Reproduced from [108,135].

With decreasing T_m, melt viscosity, gas solubility and strength increase while the diffusion rate of BA in the polymer melt reduces. Therefore, the gas loss gets reduced, leading to a more controlled foam expansion with less cell coalescence (Fig. 17b). Below the optimum T_m, expansion of the melt is inhibited and α gets much smaller. At these temperatures, another phenomena "crystallization" plays an essential role in the foaming of semi-crystalline polymers such as i-PP and PBT. Crystallization, in other words, solidification occurs when T_m or the extrudate temperature after die exit equals to the crystallization temperature (T_c) due to cooling. When T_m is too low and close to the T_c, the polymer melt at the skin freezes too fast before the extrudate is fully expanded (Fig. 17c). The process reaches its limit due to a rapid increase in barrel pressure at the B-extruder once melt solidification takes place either at the B-extruder or at the die [39,135].

2.4.2 Effect of Die Temperature

When a polymer melt passes through the die with a too high die temperature (T_{die}), featuring increased melt temperature, rapid expansion of the polymer melt with the largest α (Fig. 18a) occurs due to increased diffusivity of BA in the melt. Subsequently, with the effect of gas loss, decreased melt viscosity and strength of the foamed extrudate get smaller due to cell coalescence. By decreasing the die temperature to optimum T_{die}, leading to decreased melt temperature, controlled expansion with minimum cell coalescence and thus low-density foams

with homogeneous and fine cell morphology are achieved (Fig. 18b). When T_{die} is too low (below optimum T_{die}), with the effect of crystallization of the melt, the skin of the foamed extrudate solidifies quickly and the diffusion of BA out of the melt is suppressed by the solid skin. Therefore, a proper and controlled expansion is not realizable due to the insufficient pressure of the entrapped BA in the polymer melt with a very high melt viscosity. With the effect of crystallization and increased stiffness of the skin layer, smaller α and d are obtained (Fig. 18c). This also results in high-density foams with irregular cell morphology. These foams usually possess smaller mean cell sizes due to an increased melt viscosity, given by the high-pressure build-up and pressure drop rate [136–138].
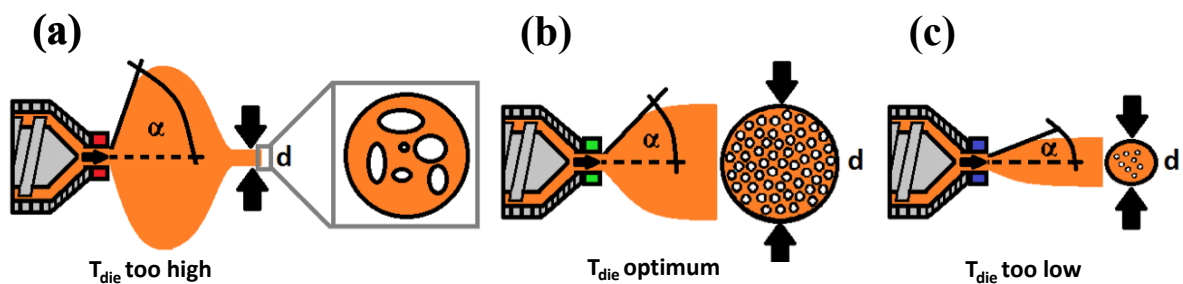
Figure 18   Effect of T_{die} on the foamed extrudate shape at optimum T_m. When T_{die} is (a) too high, (2) optimum, (3) too low. α is the melt opening angle and d is the final extrudate cross-section diameter. Reproduced from [108,135].

2.4.3 Reactive Foam Extrusion in the presence of BTAs and HNTs

The reactive foam extrusion process in the presence of BTAs and HNTs follows the same fundamental principles. The schematics of foam extrusion, corresponding melt temperature and pressure in the barrels, and concepts of foaming with BTAs and HNTs are illustrated in Figure 19.

a)

gas injection

foam
nucleation

b)

temperature

pressure

heating

RT

T_{melt}

p_{melt}

I   II   III   IV

Additive, CE
and BA
dissolved or
mixed in
polymer melt
and post-
modification

Dispersion or self-
assembly of additive into
supramolecular
nanostructures
in (polymer-gas) single
phase system and
continuity of post
modification reactions

Foaming and
crystallization
of polymer

extrusion path

c)

1 nm   1 μm   1 μm   10 μm

BTA, CE and BA
dissolved/mixed

Self-assembly of BTA

Foam cell nucleation

Foam

d)

10 nm   1 μm   1 μm   10 μm

HNTs, CE and BA
dissolved/mixed

HNTs are dispersed in
a single-phase system

Foam cell nucleation

Foam

Figure 19 Illustration of (a) a conventional reactive-tandem-foam extrusion line with (b) corresponding profiles for melt temperature (blue) and pressure (red). Concept and processing steps of foaming with (c) BTAs and (d) HNTs where the polymer matrix, CE, BA, BTAs and HNTs are shown in gray, green, blue, orange and light orange color, respectively. Reproduced from [108] and [95].

The pressure (red) and temperature profile (blue) are adapted to the particular case of foam extrusion with organic and inorganic nanoadditives such as BTAs and HNTs (Fig. 19b). The

concept and processing steps of foam extrusion based on BTAs (Fig. 19c) and HNTs (Fig. 19d) are described as follows:

Foaming with BTAs: In the A-extruder (Fig. 19b, region I-II), the cylinder temperature range is selected in a way that the BTAs can be dissolved (dispersed intimately on a molecular level) and the CE is dispersed in the polymer melt. With the injection of BA, a homogeneous single-phase mixture of polymer, BTAs and BA is formed in the melting extruder (Fig. 19b, region II). Furthermore, post-modification reactions start when the temperature and pressure reach certain values. The second extruder is not only used to build up the pressure but also for the continuity of post-modification reactions and the self-assembly of BTAs into 1D nanofibers by lowering the temperature of the single-phase system (Fig. 19b, region III). At the die, due to the pressure drop, foaming (cell nucleation and growth) starts. Subsequently, with the reduction of the temperature below T_g of the polymer, the cell growth stops. A final foam cell structure with BTA nanofibers located in the cell walls and struts is obtained (Fig. 19b, region IV).

Foaming with HNTs: In the A-extruder (Fig. 19b, region I-II), the polymer, BA, CE and HNTs are mixed under a suitable temperature range and pressure. In this extruder, the polymer is in a molten state and is able to form a single-phase system with the BA as well as the chain-extension of polymer matrix takes place. Depending on the type and concentration of HNTs, a good dispersion of HNTs in the single-phase system is provided in the A-extruder, which is preferably a twin-screw extruder. This mixed system is then transferred to the B-extruder for the continuity of the post-modification, cooling and pressure build-up (Fig. 19b, region II-III). With the effect of pressure drop, foaming of the polymer in the presence of HNTs starts at the die and continues until the cells stabilize upon cooling (Fig. 19b, region IV). HNTs are located in the walls and struts of the cells within the finally foamed structures [29,33,35,139].

2.4.4 Factors Affecting Foaming Behavior

The foaming process has a significant effect on the morphological and mechanical foam properties [140]. Therefore, for an improved processing behavior and foam properties, the control of the processing parameters is crucial. Figure 20 summarizes the factors and parameters affecting the foaming behavior.
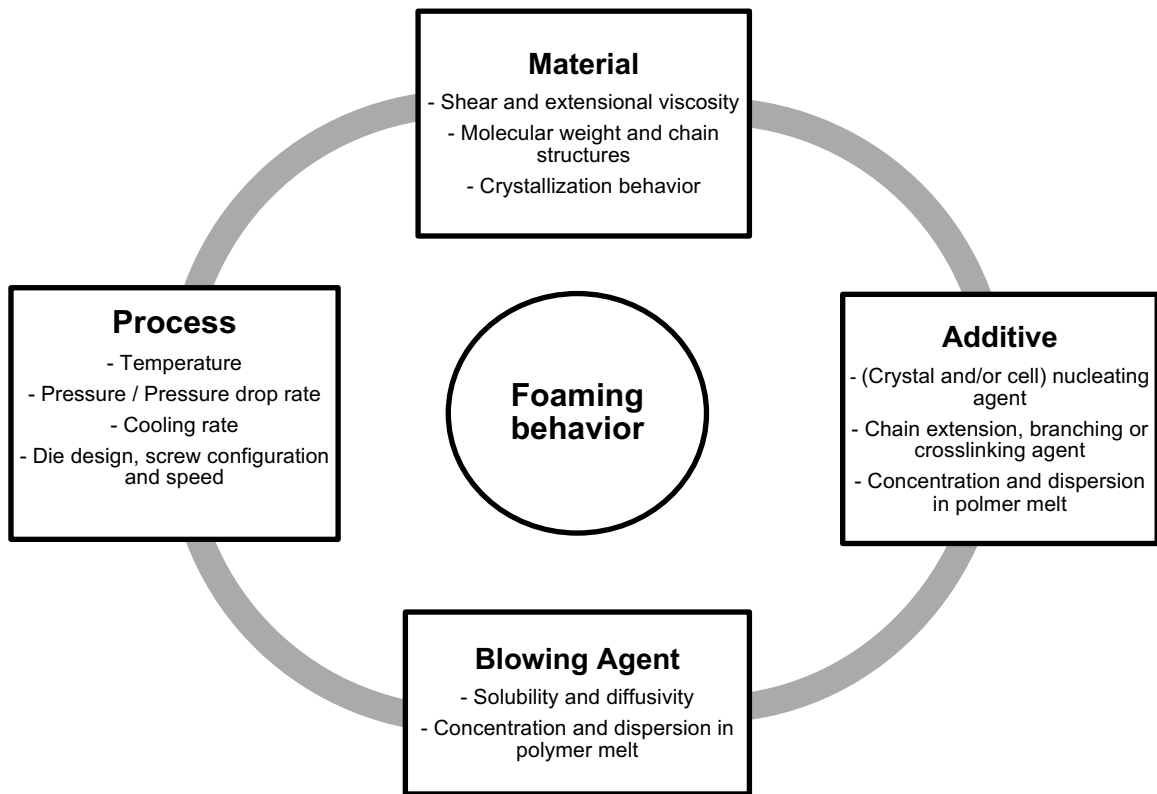
Figure 20 Summary of affecting parameters on the foaming behavior. Reproduced from [4,140,141].

Intrinsic properties of the bulk material (polymer resin), such as shear and extensional viscosity, molecular weight and chain structure (linear or branched), as well as crystallization behavior (of semi-crystalline polymers), make a significant contribution to the foamability of a single-phase system [87]. Rheological properties of the single-phase system are a function of processing conditions (e.g., T and P), solubility and diffusivity, dispersion quality and concentration of BA and additive [142]. For instance, increased melt temperature, BA concentration, nucleating agent (e.g., HNT in PS) may decrease the system's viscosity. Therefore, rheology plays a key role. Tuning rheological properties improves cell nucleation and growth and reduces cell coalescence, leading to superior morphology and enhanced properties [6,14,15]. Aside from rheology, crystallization behavior and T_g are crucial to minimize cell collapse during the stabilization step of foaming [34].

Foaming additives can be used for various purposes. For instance, chain extension and long-chain branching agents are able to increase the molecular weight and increase the melt viscosity

and melt strength of the polymer by featuring strain-hardening behavior [6,14]. To increase the molecular weight and create intrinsic entanglements in the polymer melt, reagents for post-polymerization modification reactions such as cyclic anhydrides [5,143], oxazolines [16], carbodiimides [144], isocyanates and epoxides [17,145] are used.

Nanoadditives are usually used as heterogeneous foam cell nucleating agents. They could widen the processing temperature window, improve foamability, increase the cell density and lead to a homogeneous foam morphology. Depending on the type, aspect ratio, shape and concentration of the nanoadditive, insulation and mechanical properties can be improved. Nanoadditives (e.g., BTA in i-PP) may also be used as crystal nucleating agents, where they control the crystallization behavior of the polymer by increasing the crystallization temperature. An increased crystallization temperature can be beneficial for the stabilization step of foaming [78].

BAs are also one of the critical parameters for cell nucleation and growth properties. Dissolved BAs in a polymer melt can act as plasticizers depending on their type, solubility, diffusivity, and concentration. The strong plasticizing effect leads to altered thermal and rheological properties of the polymer, such as reduced T_g and melt viscosity (more than 50 %), and thus enhanced foaming behavior and properties [142,146,147].

Processing parameters, for example, melt temperature, is crucial as it strongly affects melt viscosity while melt-pressure has an influence on both solubility and diffusivity of BA and pressure build-up during foaming. In foam extrusion, screw configuration and speed are responsible for the dispersion of the BA and additives. Controlling the process parameters governs the foaming behavior and determines the cellular structure of the foam [108].

2.5 Mechanical Properties of Rigid Polymer Foams

2.5.1 Importance of Mechanical Performance for Applications

Due to their superior mechanical performance, such as high stiffness, strength and fatigue resistance, rigid polymer foams (e.g., polymethacrylamide (PMI), styrene acrylonitrile (SAN), polyvinyl chloride (PVC), PET, PS) are very interesting for diverse applications. For instance,

they can be used as packaging materials for fish and seafood boxes, as core material for sandwich structures in aircraft, wind energy systems, automobiles, satellites, ships and architectural constructions [3,18,19].

Depending on their applications, they are subjected to various loads, including compression (e.g., packaging, sandwich structures), shear and bending (e.g., sandwich structures). Most applications of foams involve compressive loading. <u>In this thesis, a strong emphasis is put on the behavior of the polymer foams under compressive loading, which is of great importance for most of the mentioned applications</u>.

Figure 21 gives an overview of the compressive modulus and strength of the commonly used rigid polymer foams for varying foam densities and Table 2 exhibits the elastic modulus of (compact) matrix materials of those foams.
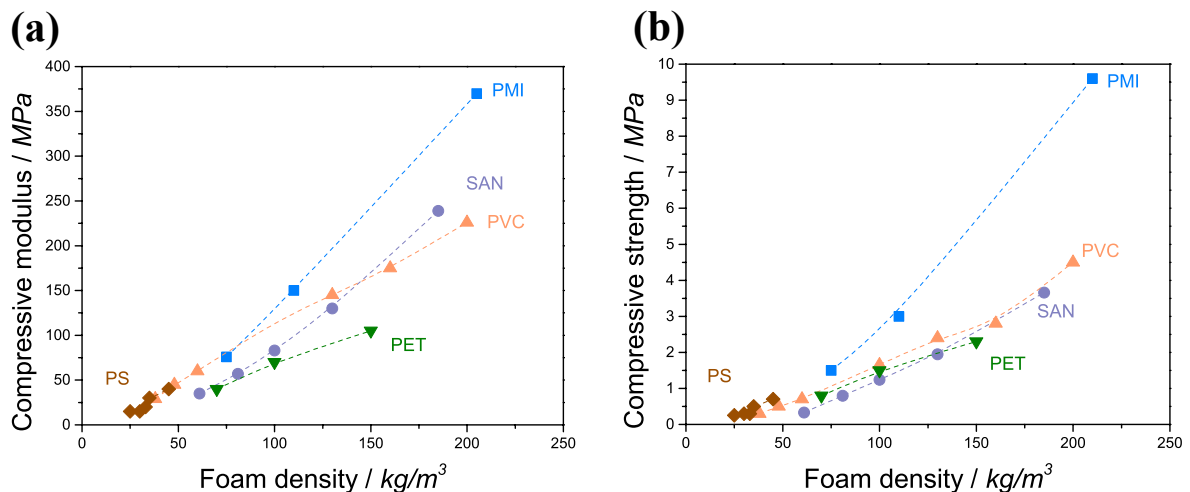
Figure 21   Overview of (a) compressive modulus and (b) compressive strength of various rigid polymer foams with different foam densities (values taken from the manufacturers' technical datasheets [d-h]).

Table 2   Density and elastic modulus of the (compact) matrix materials (values taken from the manufacturers' technical datasheets [i-m].

	PMI	PVC	SAN	PS	PET
Density [kg/m^3]	1200	1480	1070	1050	1380
Elastic Modulus [MPa]	6000	3300	3448	3300	3000

PMI foams, one of the most commonly used rigid foam as core material for sandwich constructions, show the best performance in terms of foam properties. From an economic perspective, PVC foams are cheaper than PMI, showing similar mechanical performance at low densities (< 100 kg/m^3) [n]. SAN foams are an excellent alternative to PVC foams in many applications. They show similar impact toughness and fatigue resistance yet have a better performance at higher temperatures and better static properties showing high ductility. However, they show low chemical and environmental resistance and their applications are still more limited than PVC foams, such as large, high-end luxury yachts fabricated with epoxy prepregs and SAN core.

On the other hand, PS foams are one of the most economical foams featuring very low densities and are mainly used in constructions and buildings for thermal insulation. However, their mechanical performance at these densities is insufficient to replace rigid polyester foams, such as PET used as core materials in sandwich structures. Due to their high-temperature dimensional stability, strength and stiffness, polyester foams (e.g., PET and PBT) are very interesting for many applications. In particular, PET foams can be reused by recycling at significantly lowered total production costs. As a result, the price of PET foams is far below the price range in the 2000s, when the first PET foams were introduced to the foam market.

Comparing the mechanical performance of various foams, it is worthy to note that elastic modulus of the matrix (compact) materials plays a significant role. Looking at Fig. 21a and the values from Table 2, it can be supposed that elastic modulus of the matrix materials is proportional to modulus of the foams at certain density values.

Aside from mentioned rigid foams, PBT suggests an interesting property profile for its foams. However, up to now, no commercially available PBT foams are found yet. The benefits of PBT

and a detailed literature survey on the foamability of PBT and resulting PBT foams will be reported in *Chapter 2.6*.

2.5.2 Principles Affecting the Compressive Properties of Foams

The compressive properties of the foam are dependent on its microstructural characteristics. The principles which influence the compressive properties can be divided into three main classes [148]:

- The properties of the bulk material of which the foam is made (e.g., solid properties: yield strength, modulus, ductility, brittleness).
- The cell topology (connectivity) and shape (e.g., wood-like cell shape (anisotropic elongated cells): stretch-dominated behavior; honey-comb-like morphology (isotropic cells): bending-dominated behavior).
- The relative density (e.g., cell edge (strut) length, cell edge thickness).

2.5.3 Compressive Behavior and Deformation Mechanisms of Closed-Cell Rigid Foams

2.5.3.1 Gibson and Ashby Model

In order to predict compressive behavior of cellular materials, numerous cell models have been proposed. The models can be categorized into two main sections: (1) **Bending-dominated deformation models** by Ko [149], Triantafillou et al. [149], Zhu et al. [150,151], Maiti et al. [152], Huber and Gibson [152] reporting that the deformation is governed by bending of the cell struts and walls, leading to a quadratic dependence of foam stiffness on density. This type of deformation is usually seen in foams with "low nodal connectivity" which means that cell struts have a high tendency to bend under compression (Fig. 22b). Most of the foams show a bending-dominated deformation mechanism. (2) **Stretch-dominated deformation models** by Gent and Thomas [153,154], Lederman [155], Cunningham [156], Christensen [157] and Kanakkkanatt [158] suggesting that the microscopic deformation mechanism of the foam cells involve deformation along the strut length, including stretching (in tension) and axial compression (buckling) of the cell struts and walls (Fig. 22c). This is resulting in a linear dependence of stiffness on foam density. The foams with cell orientation or "high nodal connectivity" (which hinders the struts from bending) follow this deformation mechanism.

Nevertheless, the microscopic deformation mechanism of foams may involve the combination of both bending and stretching. One of the most famous and extensive models, namely a cubic cell model, was developed by Gibson and Ashby [1], illustrated in Figure 22.
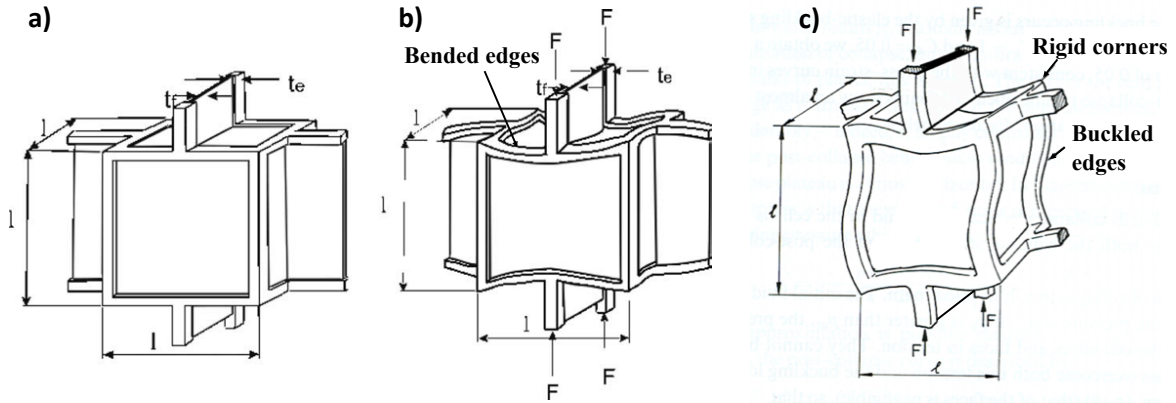
Figure 22 Gibson-Ashby cubic cell model for (a) undeformed closed-cell foam, (b) bending-dominated deformation (c) stretch-dominated deformation of closed-cell foam under compressive loading, showing the edge thickness t_e, face thickness t_f, edge length l, and compression force F.

This model is valid at relative densities up to 0.3 (foam density of up to 390 kg/m^3 for PBT) considers both effects of bending and stretching as well as the effect of the internal gas pressure (for closed-cell foams) [159]. According to Gibson and Ashby, the stiffness of closed-cell foam results from three contributions: The first component is **edge bending** stiffness, which determines the elastic modulus. The second component is **face stretching** and cell wall elastic buckling, which causes elastic collapse. The final component is the **internal gas compression** of the closed cells, which is ignorable when internal pressure equals to the atmospheric pressure (except for elastomeric closed-cell foams) [160]. The sum of the three components can be expressed by Equation 16:

$$\frac{E_f}{E_s} = \phi_s^2 \left(\frac{\rho_f}{\rho_s}\right)^2 + (1 - \phi_s)\left(\frac{\rho_f}{\rho_s}\right) + \frac{p_0(1 - 2\nu_f)}{E_s(1 - \frac{\rho_f}{\rho_s})} \tag{16}$$

where E_f is the elastic modulus of foams, E_s is the elastic modulus of solid materials, ρ_f is the foam density, ρ_s is the solid polymer density, ϕ_s is the fraction of polymer contained in cell

struts, and thus $1 - \phi_s$ is the solid fraction in cell walls, p_0 is the internal gas pressure of the cells and ν_f is Poisson's ratio.

This equation shows that the compressive modulus is influenced by bulk material properties, porosity, foam density, and cell wall/strut fraction in foam cells. The following simplified Equation 17 can be derived from Equation 16, showing a power-law relationship describing the functional dependence of the modulus on the foam density [160].

$$E \propto \rho^n \qquad (17)$$

where n is the density exponent of the foam. For bulk materials, the density exponent is 1, suggesting a linear relationship between modulus and solid material density. For open-cell foams, the density exponent is 2, as there is no solid fraction in cell walls $(1 - \phi = 0)$. For closed-cell foams, the value of n should be between 1 and 2.

2.5.3.2 Deformation Mechanism: Stress-Strain Diagram

Besides bulk material properties and foam density, the deformation mechanism of the foams also depends on cellular structure (cell size, topology, and shape), which can be affected by the foam extrusion process. When the polymer melt exits the die, the fast expansion and foaming occur during processing, leading to more elongated than spherical cell shapes in the extrusion direction. This anisotropy in the foam cell structure can be attributed to the anisotropic compressive properties of extruded foams. A recent fundamental study by Fathi [161] gives a deep understanding of the anisotropy associated with the deformation mechanism of extruded PET foam. The deformation mechanisms of PET foam in three loading directions are shown in Figure 23.
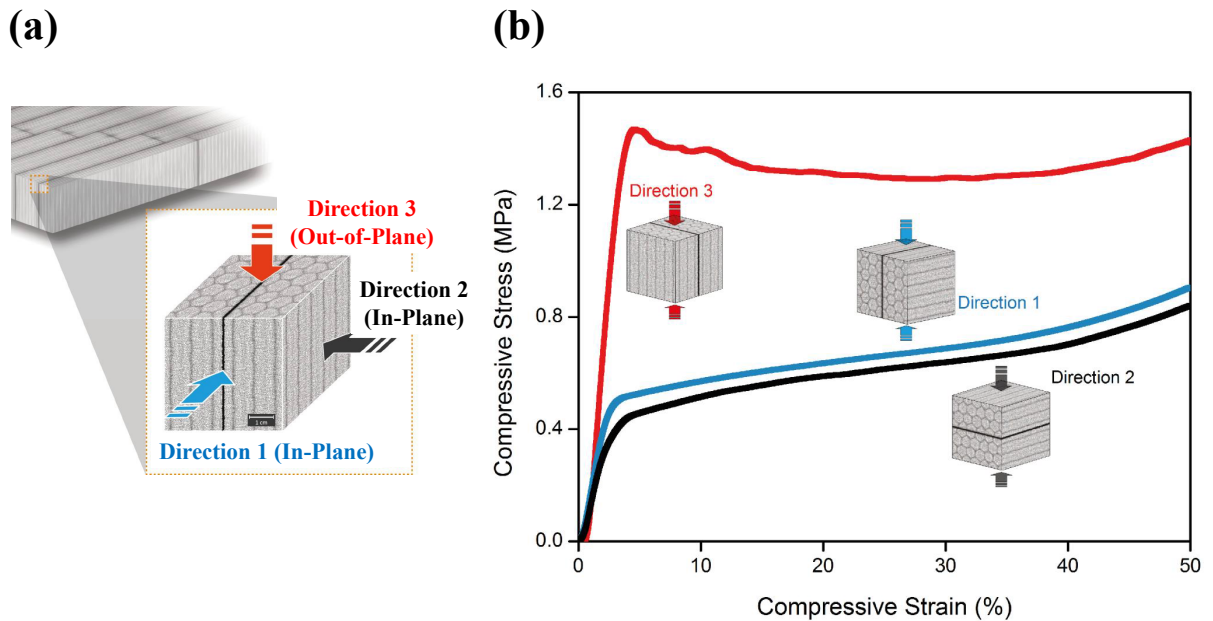
Figure 23 (a) Loading directions of PET foam (b) Compressive stress-strain curves of extruded PET foams in three loading directions. Reproduced from [161].

It was reported that extruded PET foams have combinations of wood-like morphology with highly elongated and oriented cell shape in out-of-plane (parallel to the extrusion) direction and honeycomb-like morphology with hexagonal cell shape in the in-plane (perpendicular to the extrusion) direction. This morphological anisotropy resulted in two fundamental deformation mechanisms. It was claimed that when PET foam is subjected to the load in directions 1 and 2, the honeycomb-like cellular structure shows a typical bending-dominated deformation (Fig. 22b). When loaded out-of-plane (direction 3), the wood-like cellular structure exhibits typical stretch-dominated deformation where the deformation starts with a strong axial response, followed by local plastic buckling of the cell walls and struts (Fig. 22c). These two different deformation mechanisms resulted in different stress-strain curves. The deformation curves of in-plane directions (lines in blue and black, Fig. 23b) were more orderly and regular, which was attributed to uniform hexagonal cell shapes.

In contrast, the cell deformation mechanism in the out-of-plane direction (red line, Fig. 23b) showed a linear behavior until the yield point, followed by a slight or marginal decrease in stress, continued with variations in stress level until a sharp increase with densification takes place. These changes in stress between the yield point and densification are attributed to the interlocked, irregularly elongated cells. Nevertheless, comparing both deformation

mechanisms, the modulus and initial collapse strength of stretch-dominated (direction 3) lattices are much higher than bending-dominated (direction 1 and 2) lattices at the same relative density. This is due to the different failure modes which are involved with two different deformation mechanisms. "Hard mode" failure is induced by stretching and axial compression in stretch-dominated deformation leading to higher modulus and collapse strength, while "soft mode" failure involves bending. This makes stretch-dominated wood-like cellular structures an excellent choice for lightweight structural applications [148].

This thesis will investigate extruded PBT foams' deformation mechanism that has a similar anisotropic cellular structure as extruded PET foams. It will mainly focus on the stretch-dominated deformation mechanism induced by a compressive loading in an out-of-plane direction.

Figure 24 exhibits the picture of the cubic mPBT foam sample with the length of 10 mm, which was prepared from the foam strand, and Figure 25 shows the stress-strain curve of this cubic foam loaded in an out-of-plane direction with a test speed of 1 mm/min.

Figure 24   Picture the foam strand and the cubic foam sample with the length of 10 mm.
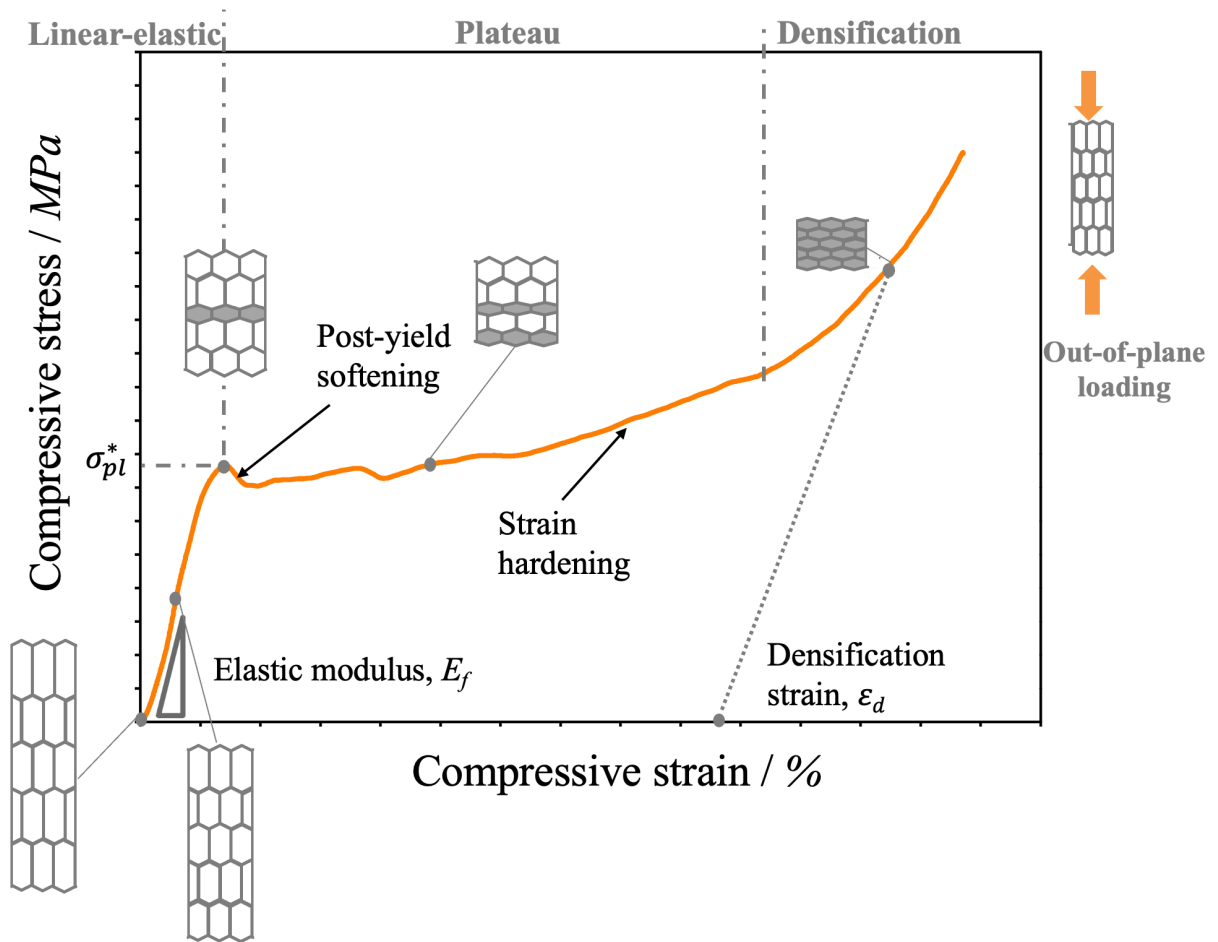
Figure 25 Compressive stress-strain curve of an extruded mPBT foam in the out-of-plane loading direction. σ_{pl}^* is plastic collapse stress. The curve was obtained using self-manufactured mPBT foam sample and reproduced from [162].

Similar to PET, extruded PBT foam also shows a typical stress-strain curve induced by stretch-dominated deformation when loaded in an out-of-plane direction. This curve is generally composed of three regions, namely (1) linear elastic, (2) plateau and (3) densification region.

The first region is controlled by elastic bending or cell wall-stretching. The initial slope of this region gives the elastic (Young`s) modulus, E_f. If the strains are small, the foam only shows an elastic response. The elastic modulus for stretch-dominated deformation mechanism can be expressed by Equation 18 [163]:

$$E_f \approx \frac{1}{3}\left(\frac{\rho_f}{\rho_s}\right) E_s \tag{18}$$

where E_s is the elastic modulus of the cell wall (bulk) material and $\frac{\rho_f}{\rho_s}$ is the relative density.

The second (plateau) region starts from the yield point, namely plastic collapse stress, σ_{pl}^*, where the stress reaches its peak. The local peak or σ_{pl}^* is associated with the initiation of cell collapse with the effect of buckling and/or plastic hinge formation. The plastic collapse stress for a stretch-dominated deformation mechanism is given in Equation 19 [163].

$$\sigma_{pl}^* \approx \frac{1}{3}\left(\frac{\rho_f}{\rho_s}\right) \sigma_{y,s} \tag{19}$$

where $\sigma_{y,s}$ is the yield strength of the cell wall material. The relative density for closed-cell foams can be related to the cell shape, including cell wall edge (strut) thickness t_w, and strut length l_s as given in Equation 20. This relation is usually valid for low-density foams (where $t_w << l_s$) [1].

$$\left(\frac{\rho_f}{\rho_s}\right) = \left(\frac{t_w}{l_s}\right)^2 \tag{20}$$

Initial yield is then followed by the "post-yield softening", which is a sharp drop in the stress with increasing strain due to the localization of the strains in distinct regions of the foams. These highly localized deformations can be local plastic buckling, collapse of the cell struts and shear deformation zones (shear bending or yielding) [148]. With increasing stress levels, cell collapse continues and local densifications cause "strain hardening" which is a rapid increase in stress with increasing strain [164]. In contrast to the bending-dominated deformation, the plateau region does not show a long, flat plateau, which is not very advantageous for energy-absorbing applications [148].

The third region involves densification of the foam associated with the complete failure of the foam cells throughout the sample. With the cell wall collapse, the opposite cell walls start touching each other, and stress increases sharply. In an ideal case, after sufficient densification, the foam sample behaves like a compact material [164].

2.5.4   Strategies to improve Compressive Properties of Foams

The compressive properties of polymer foams are influenced mainly by foam density. Achieving rigid foams with improved compressive strength and stiffness at low-density ($80 – 100$ kg/m^3) is a key challenge. Foaming methods and rheological properties of the bulk material (modification) also play an important role in obtaining lightweight core materials [165]. In addition, reduced cell sizes (< 100 μm) and a homogeneous cellular structure composed of durable cell walls and struts are also targets for mechanical enhancement [26]. Therefore, nanoadditives as reinforcing and foam nucleating agents have a high potential and are one of the most frequently used strategies to decrease and homogenize the sizes.

2.5.4.1 Potential of BTAs on improving Mechanical Properties

The influence of BTAs as a foam and crystal nucleating agent on foam morphologies of semi-crystalline i-PP and amorphous PS was mentioned in *Chapter 2.3.1*. Stumpf et al. [94] produced BTA-based foam injection-molded samples and investigated the effect of BTAs on the mechanical properties of the foams. It was reported that BTAs could lead to improved mechanical properties such as specific flexural strength and specific flexural modulus. Afterwards, Mörl et al. [94] showed that only small amounts of BTA (e.g., 0.02 wt%) could improve the specific compressive strength of extruded i-PP by around 100 % in out-of-plane direction. The improved mechanical properties were associated with the cell size reduction and more homogeneous cell morphology as well as the effect of BTA fibers located on the cell walls and struts. In another study [166], amorphous PS foams, including BTAs were manufactured via foam extrusion. It was found that 0.2 wt% BTA increased the normalized compression modulus by about 23 %. Similar to the study of [94], the enhancement was attributed to nanofibers' additional stress contribution, which might retard the foams' face stretching and edge bending.

2.5.4.2 Potential of HNTs on improving Mechanical Properties

The effect of HNTs on the improvement of the morphology of PLA [29], PP [34] and PBS [35] foams have already been reported, as stated previously (*Chapter 2.3.2*). Furthermore, Eryildiz

et al. [33] showed that 0.5 wt% HNT could increase tensile strength and elongation of injection molded PLA foams by approximately 50 % and 77 %, respectively. The improved mechanical properties were attributed to the intrinsic reinforcing effect of HNTs and an enhanced foam morphology with small cells and uniform structures induced by homogeneously dispersed HNT nanoparticles [33]. Besides thermoplastic polymer foams, HNT was also used as a foaming additive for thermoset polymers and rubbers. Dando and Salem [167] prepared HNT-based syntactic epoxy foams by using thermoplastic micro balloons. 0.5 wt% HNT led to 165 % and 244 % increase of compressive strength and modulus, respectively [167]. In addition, Lee et al. [139] showed that HNTs could improve the morphology and stiffness of rubber foams. The researchers prepared ethylene–propylene–diene monomer (EPDM) foams including 3, 5, 7 and 10 wt% HNT by batch foaming with sc-CO_2. It was found that HNTs can act as both nucleating agents and reinforcing additives. With increasing concentration of up to 10 wt% HNT, the smallest mean cell size of 7.8 µm, the highest cell density of 1.5×10^{10} cells/cm^3 and the highest compressive modulus of 2.43 ± 0.05 MPa were achieved [139]. However, to the best of my knowledge, research on the effect of HNTs on foamability, morphology and compressive properties of foams made from the engineering polymer PBT does not exist in literature.

2.6   Literature Survey on PBT Foams

In contrast to PET foams, the number of studies in literature on PBT foams is very limited [2,3,15,18,19,165,168–170]. Yet, PBT is a promising candidate to be used in the polymer foam market due to its multiple beneficial properties. For instance, the flexible and mobile butylene groups of PBT increase the crystallization efficiency to generate a well-ordered molecular structure. This ordered molecular structure can contribute to enhancing the mechanical properties. In addition, the unique crystallization behavior, the faster crystallization kinetics compared to PET and the small-sized crystallites of PBT are advantageous to achieve a fine-cellular morphology and enhanced mechanical properties upon foaming. Due to their high-temperature dimensional stability, high heat deflection temperature (up to 150 °C), chemical and abrasion resistance, PBT foams are a good alternative to i-PP foams having lower temperatures dimensional stability and PET possessing slower crystallization kinetics [165]. Nevertheless, as for all semi-crystalline polymers, the foaming process of PBT remains

challenging compared to amorphous polymers due to its low-melt viscosity, strength and narrower processing-temperature window.

The first example on PBT foams was presented by Klotzer et al. [170]. The researchers produced PBT foams with a coarse cell morphology for membrane applications. Afterwards, Song et al. [19] attempted to produce open-celled PBT foams by using a technology called "Dynamic Decompression and Cooling (DDC) Process", which is an unconventional foaming method compared to the extrusion foaming. More systematic studies including conventional foaming techniques were then reported by Jeong et al. [3,18]. The authors first developed PBT foams by using a lab-scale foam extrusion process and the chemical BA 5-Phenyltetrazole. Rheological and thermal properties of PBT and correlations with the resulting foam morphology were also presented. PBT foams with a relatively high foam density of around 600 kg/m^3 and a mean cell size of 500 μm were obtained. This, coarse cell morphology and the high foam densities were obtained due to the low melt viscosity and low melt strength. To address this, the researchers improved the melt strength of PBT by using the chain extender (CE) triglycidyl isocyanurate (TGIC). In this case, the PBA isobutane was used. By doing so, they achieved extruded PBT foams with an intermediate density of around 330 kg/m^3 and a more homogeneous foam morphology with the smallest mean cell size of 91 μm. Nevertheless, no further efforts have been reported to improve foamability, foam morphology, and properties by using nucleating agents. Furthermore, Köppl [4] studied the foamability of PBT by using industrially relevant processes including foam extrusion, bead foaming and foam injection molding in his thesis. The common challenge observed during processing was insufficient foam stabilization resulting from the poor melt strength of PBT. This led to high foam densities, cell coalescence and inhomogeneous foam morphologies. By process optimization, PBT foam strands with the smallest foam density of 170 kg/m^3 were achieved in the literature. It was proposed that with a 4 °C decrease in melt temperature (from 224 °C to 220 °C), foam densities decreased from about 720 to 170 kg/m^3. However, the mean cell size increased from 60 to 315 μm. Given this, a material optimization was performed with 2 wt% talc as foam nucleating agent to generate fine-celled foams at lower densities. As a result, a minimum mean cell size of 5 μm, yet a maximum foam density of about 980 kg/m^3 was obtained. By applying underwater granulation (UWG), better foam stabilization was achieved by rapid cooling with water. Consequently, foamed beads having a density of 230 kg/m^3 and mean cell size of 250 μm were produced. Further density and cell size reduction by using the same system were not

realizable. As a continuity study to the bead foaming of PBT, Standau et al.[15] used 1 wt% CE to increase melt strength and foamability of PBT by long-chain branching. The improved melt strength and process optimization (e.g., die temperature, PBA concentration, water temperature and blade speed of the UWG) led to foamed beads with a reduced foam density of 179 kg/m^3, cell size of 155 µm and more homogeneous foam morphology. For the first time, steam chest molding of beads was successfully implemented and bead foam parts with the minimum foam density in literature (170 kg/m^3) were achieved. Moreover, a comparison study of [168] expanded-PP (e-PP) and expanded-PBT (e-PBT) bead foams was reported where the thermo-mechanical properties and burning behavior of the foams were compared. The tensile modulus of e-PBT parts was similar, and compressive strength at elevated temperatures was higher than that of e-PP [168].

Aside from foam extrusion and bead foaming, Köppl [4] also demonstrated the applicability of foam injection molding of PBT with a breathing mold technology in his Ph.D. thesis. Using nitrogen as a physical blowing agent led to a maximum foam density reduction of 50 % and a minimum mean cell size of 60 µm. Furthermore, by using aluminum diethyl phosphinate (AlPi-Et) as a flame retardant, the structure-property relationships of flame-retarded injection-molded PBT foams were established. With 6 wt% AlPi-Et a higher number of smaller cells and more uniform morphology than the neat PBT foam were observed. Further increase in AlPi-Et concentration (20 wt%) led to a larger number of particle agglomerates and an increased mean cell size of 130 µm as well as a more inhomogeneous foam morphology. This resulted in deteriorated mechanical properties. It was concluded that AlPi-Et is a very effective flame retardant. However, depending on the concentration, it significantly reduced the strength and toughness of the foams and can therefore not be used without an impact modifier.

However, to the best of my knowledge, a fundamental study on the effect of nanoadditives on foamability, morphology and compressive properties of the extruded PBT foam strand is still missing in the literature.

3 Aims and Structure of the Thesis

As reported in *Chapter 2.6*, in the previous study on PBT foams, Köppl was able to produce PBT foam strands with the smallest density of 170 kg/m^3 via foam extrusion process. Very narrow process temperatures and insufficient foam stabilization induced by the low melt strength of PBT were the main challenges during the process. This led to extruded foams with a coarse morphology. Therefore, it was proposed that the chemical modification (long-chain branching) of PBT with CE is a suitable solution for an increased melt strength and thus for an improved foamability and as a consequence enhanced foam morphology and properties. Furthermore, the use of a micro-scale foam nucleating agent (talc) was shown to be effective for cell size reduction. However, with decreasing cell size, the foam density also increased. Since the PBT foam strands produced by Köppl were very inhomogeneous, no mechanical properties of these strands could be reported. Based on the findings of the previous study, the goals of this thesis are set.

Prior to foaming, the PBT matrix will be chemically modified with a CE (designated as mPBT) to increase melt strength, foam stability, and widen the processing temperature window. *The ultimate goal of this thesis is to obtain low-density (< 100 kg/m^3) extruded strand foams of mPBT with a fine-cellular and homogeneous morphology (< 500 μm).* With the use of organic (BTA) and inorganic (HNTs) nanoadditives as polymer crystal nucleating agents as well as nucleating agents for foam cells, an improvement in mechanical properties compared to the reference foam (neat mPBT from without nanoadditives) is aimed. A decreased foam density is essential for insulation properties, while mechanical properties play a significant role for rigid foams in numerous applications. For the first time, structure-property relationships of mPBT foamed strands influenced by the nanoadditives regarding melt strength, foamability and crystallization kinetics of mPBT will be established.

As shown in literature, organic nanoadditives, particularly BTAs, are soluble in the PBT melt at specific concentrations and process temperatures [171]. Upon cooling, BTAs can self-assemble and form network-like structures of nanofibers. These nanofibers can act in the polymer foam as efficient nucleating agents for polymer crystals (for instance, for i-PP) as well as foam cells (for instance, for PS and i-PP) [26,94,95,166] leading to foams with smaller cells.

The individual chemical structure of BTAs has a significant effect on the resulting nanofiber size and nucleation efficiency, whereby some of the BTAs provided an increase in crystallization temperature of PBT. In contrast, other BTAs are present as nanofibers but could not nucleate PBT at all [171]. Herein, for the first time, a commercially available BTA (BTA1) and a laboratory-scale, tailor-made BTA (BTA2) were used in PBT to control the cell nucleation, foam morphology and mechanical properties. Both BTAs are known to form nanofibers upon cooling within the PBT polymer melt at different concentrations. However, they feature different chemical structures and solubility behavior and thus, both result in nanofibers of different diameters. Therefore, it is crucial to investigate the influence of type and concentrations of BTAs on the crystallization and rheological properties of mPBT as well as foamability, morphology and the resulting mechanical properties of mPBT foams.

The use of inorganic nanoadditives, particularly HNTs as nucleating agents for polymer crystals as well as cell nucleating agents for foamed polymers, such as PLA [29] and PP [34], have been reported in the literature. In this study, HNTs were used to control the crystallization behavior and the foam cell nucleation of PBT for the first time. Reduction of the mean cell size and a uniform foam morphology with the addition of different concentrations of HNTs (lower than 1 wt%) are focused in this thesis to improve the resulting compressive properties of the foams by increasing the buckling resistance.

Mainly, the following points are stating the individual aims within this thesis:

1. **<u>Effect of CE on the rheological properties and foamability of PBT, as well as on density and morphology of PBT foams.</u>**

   - Understanding the effect of CE concentration on the complex viscosity and strain hardening behavior of PBT.
   - Influence of rheological properties of PBT induced by different CE concentrations on process temperature window, foam density and morphology.

2. **<u>Understanding of the influence of BTAs and HNTs on the crystallization behavior and rheological properties of mPBT.</u>**

   - Evaluation of the influence of BTA type (chemical structure and resulting fiber diameter) and concentration of BTAs and HNTs on the crystal nucleation behavior (activation energy) of the mPBT resin.

- Establishing relationships between the strain hardening behavior and foamability.

3. **<u>Understanding the cell nucleation behavior and morphology development in BTA-</u>**
   <u>and HNT-nucleated mPBT foams compared to the neat mPBT foam as reference.</u>

- Defining the optimum process temperature window featuring the optimum foams with the lowest density and improved morphology.
- Evaluation of the influence of BTA type and concentrations of BTAs and HNTs on the foam morphology.
- To point out correlations between strain hardening behavior tuned by nanoadditives and the resulting foam morphology.

4. **<u>Improving the compressive properties of mPBT foams with BTAs and/or HNTs at</u>**
   <u>low foam densities.</u>

- Evaluation of the micromechanical deformation mechanism of BTA- and HNT-nucleated mPBT foams in out-of-plane direction loading, compared to the neat mPBT as a reference.
- Understanding the effect of foam density on the compressive properties of the foams.
- Investigating the influence of the cellular morphology (cell size, strut length and strut thickness) on compressive properties of the foams.
- Confirming the hypothesis of having synergistic effects by combining BTAs and HNTs at their optimum concentrations to achieve foams with superior compressive properties.

Figure 26 exhibits a schematic overview on the strategy considered for the experimental workflow in this thesis. Material analysis, including the selection of the optimum PBT grade and CE concentration for the modification of PBT, will be discussed in Chapter 5.1. In Chapter 5.2, mPBT foams nucleated with BTA1 and BTA2 at various concentrations will be produced. The optimum processing temperature windows for the foam extrusion will be determined. The effect of type and concentrations of BTAs on melt strength (strain hardening behavior), foam morphology and compressive properties will be investigated. The optimum BTA type and concentration leading to the best foam properties will be selected based on the findings. In Chapter 5.3, the same concentrations, processing conditions and characterization steps will be implemented by using HNTs to compare the influence of HNTs on cell nucleation efficiency and resulting morphology and compressive properties. Based on the results obtained from this chapter, an optimum HNT concentration resulting in foams with the lowest foam density, finest morphology and the best mechanical performance will be chosen. The validation of the

synergistic effects by using different types of nanoadditives in mPBT foams, and their effect on cell nucleation behavior, foam morphology and properties will be discussed in Chapter 5.4.

The contents of Chapters 5.1 and 5.2 are partially published by the author in the form of one peer-reviewed journal contribution, in the journal of *Polymers*, having an open-access license. As the article is licensed under a license CC BY 4.0, the permission to reprint any text and figures is given upon citation, where applicable.
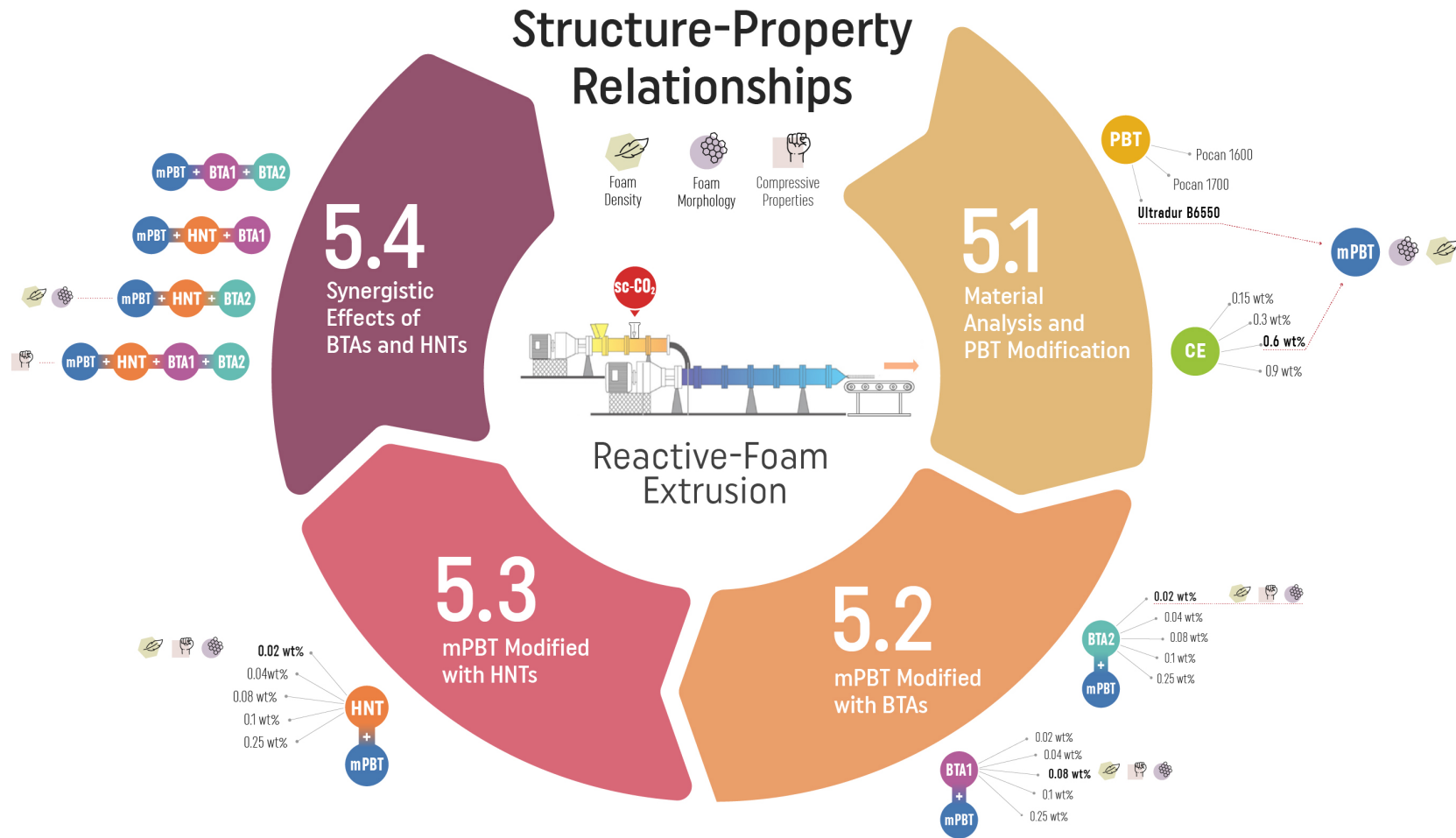
Figure 26 Graphical abstract of the thesis summarizing the results and discussions chapter.

4 Experimental

4.1 Materials

In this work, three different grades of PBT were used. The information, including trade name, name of the supplier, weight-averaged molecular weight (M_w), number-average molecular weight (M_n), polydispersity index (PDI) and melt volume rate (MVR) of the grades are listed in Table 3.

Table 3   General information about the PBT grades.

Trade name	Supplier	M_w [g/mol] [*]	M_n [g/mol] [*]	PDI [*]	MVR [cm^3/10 min] [**]
POCAN® B 1600 000000	LANXESS GmbH, Leverkusen, Germany	51,000	27,000	1.88	14
POCAN® B 1700 000000	LANXESS GmbH, Leverkusen, Germany	55,000	28,000	1.96	8
Ultradur® B 6550	BASF SE, Ludwigshafen, Germany	90,000	34,000	2.65	9.5

[*] Data provided by suppliers [o,p]

[**] Data from the supplier`s material datasheet. MVR of Pocan grades and Ultradur® were determined at 250 °C and 2.16 kg.

All PBT grades have a density of 1300 kg/m³ [q-s]. Prior to processing, PBT was dried overnight at 120 °C under vacuum.

For the post-modification of PBT, an epoxy-based multifunctional, reactive copolymer was used (CE). This CE (Joncryl® ADR 4468) was purchased from BASF SE (Ludwigshafen, Germany). It has an M_w of 6,978 g/mol and an epoxy equivalent weight of 315 g/mol [t]. The chemical structures of PBT and CE are illustrated in Figures 27a and 27b.

(a)   **(b)**
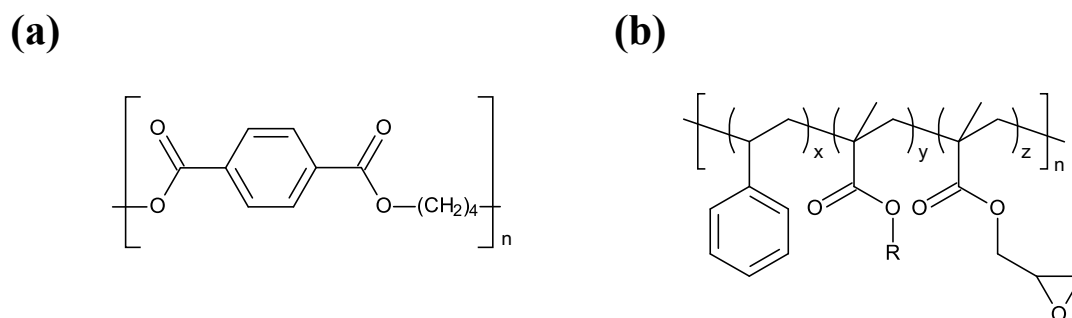
Figure 27   Chemical structures of (a) PBT (b) Joncryl® ADR 4468.

Two possible post-modification reactions of PBT with an epoxy-based CE are known, as illustrated in Figure 28 [3].

(a)

Carboxyl group   Epoxy group
of PBT   of CE

(b)

Hydroxyl group   Epoxy group
of PBT   of CE
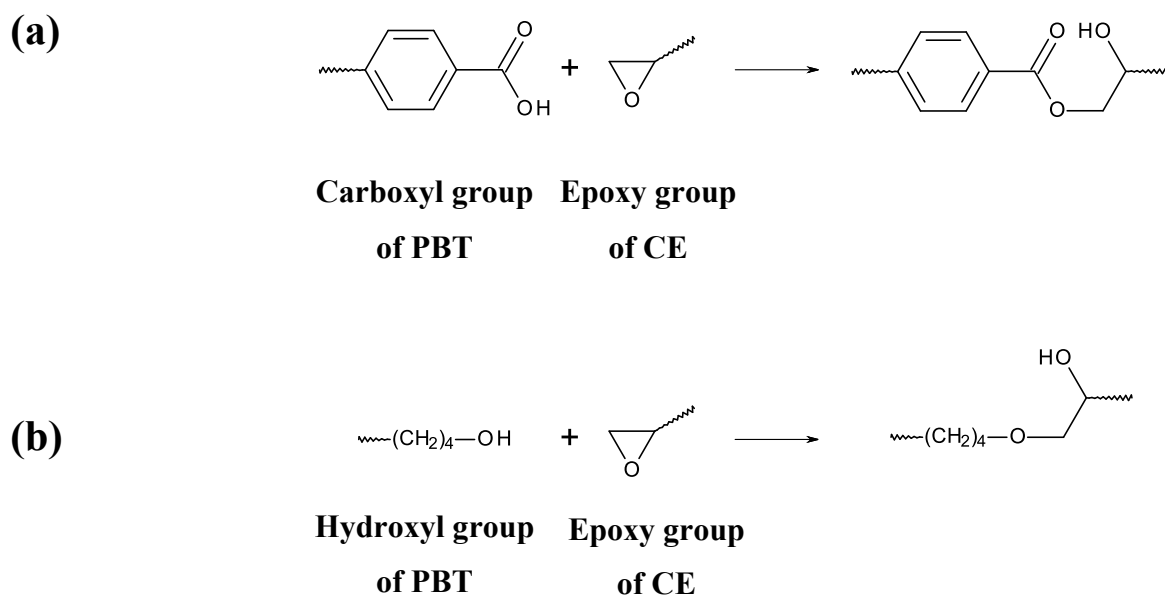
Figure 28   General scheme of two types of post-modification reactions between the terminal end groups of PBT and an epoxy-based CE: (a) esterification and (b) etherification.

The epoxide-moieties of the CE can react either with the carboxy-terminal groups of the PBT (esterification) or with the hydroxyl-terminal groups of the PBT (etherification). Considering

the epoxy equivalent weight of the CE, a relevant concentration range of CE used for post-modification of PBT was calculated. Based on this, CE concentrations were selected as 0.15, 0.3, 0.6 and 0.9 wt%.

In the melt supramolecular polymer additives based on 1,3,5-benzenetrisamide (BTA) were used as soluble additives. The commercially available Irgaclear® XT 386 with the following composition, N,N',N''-1,3,5-benzenetriyltris(2,2-dimethylpropanamide) (BTA1), was provided by BASF SE (Ludwigshafen, Germany). N,N',N''-tert-octyl-1,3,5-benzene-tricarboxylic acid (BTA2) is an experimental additive, synthesized and characterized at the Department of Macromolecular Chemistry I, University of Bayreuth according to literature procedures described in [172–174]. BTA1 and BTA2 were selected for this work. Both BTA1 and BTA2 are known to form nanofibers in the PBT polymer melt but feature a different chemical structure and solubility behavior and thus reveal nanofibers with different diameters [171]. The dissolution and self-assembly temperatures of the selected BTAs having different concentrations were reported in the study of Richter et al., systematically [171]. Based on these findings from literature and pre-trials of BTA based PBT foam extrusion, BTA concentrations for this study were selected as 0.02, 0.04, 0.08, 0.1 and 0.25 wt%.

The chemical structures of BTA1 and BTA2 are shown in Figures 29a and 29b, respectively.
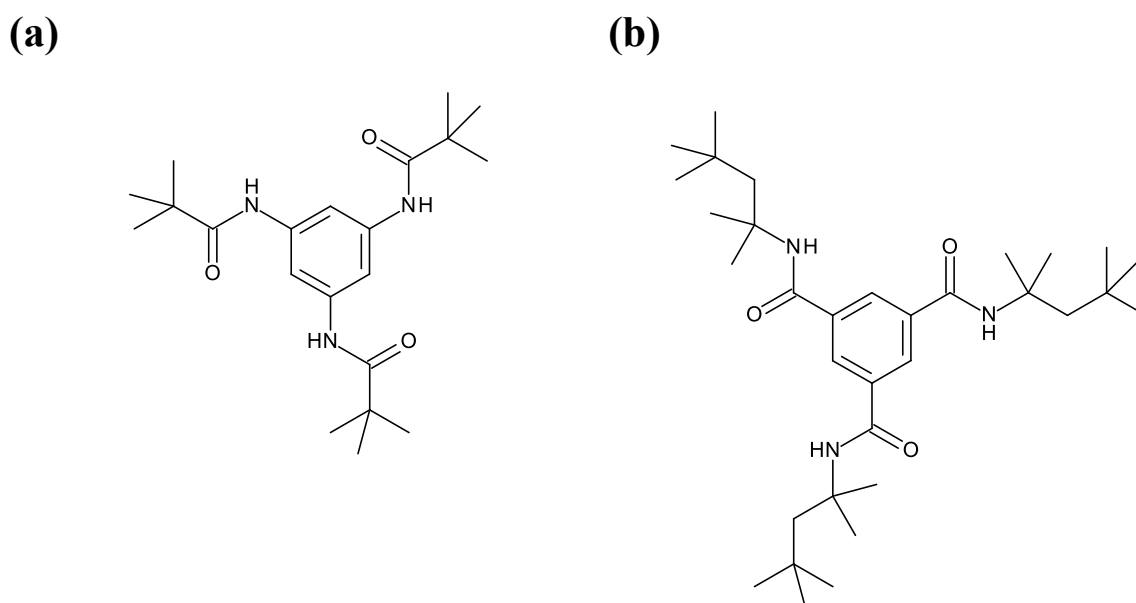
Figure 29 Chemical structures of (a) BTA1 and (b) BTA2.

HNT (MF5, DURTEC GmbH, Germany) was used as an insoluble additive in this work. For the sake of better comparison of HNTs with BTAs, same concentrations of 0.02, 0.04, 0.08, 0.1 and 0.25 wt% were selected.

The characteristic properties and a TEM image of the nanotubes are shown in Table 4 and Figure 30, respectively.

Table 4   Some characteristics of the HNT used for this work.

Name	Mineral content	Length	Inner diameter	Outer diameter	Aspect ratio
	[%]	[μm]	[nm]	[nm]	
HNT	> 95	0.4 – 1	15	80	10

200 nm
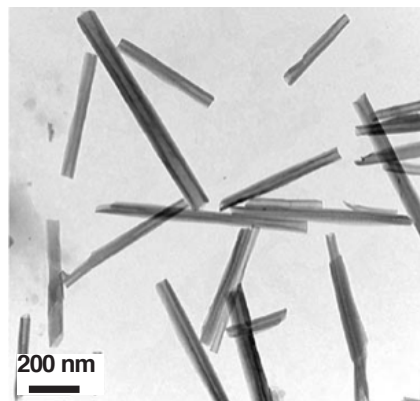
Figure 30   TEM image of MF5 nanotubes. Reproduced from [175].

In order to obtain foams of neat mPBT, mPBT foams with BTAs and HNT, 2 wt% s-CO_2 was used as a physical blowing agent.

4.2 Sample Preparation

4.2.1 Preparation of Powder Mixtures

As the additive concentrations used in this work are smaller than 1 wt%, prior to melt compounding and foam extrusion processes, the powder-mixtures of PBT, CE and BTAs were prepared for each BTA and HNT concentration. PBT granulates were first cryo-milled into powder with the size around 1000 μm by ultra-centrifugal mill (ZM 200, RETSCH GmbH, Haan, Germany), at a rotation speed of 8000 rotation per minute (rpm). CE pellets were ground into a fine powder using a pestle and mortar. Depending on formulations with different CE, BTA and HNT concentrations, powder mixtures were filled into glass bottles. The weight of the mixtures ranged from 40 to 70 g, occupying slightly half the volume of the glass bottles. As a reference, the powder mixture of PBT and CE was also prepared identically. Before mixing, PBT powder, BTAs and HNTs were dried overnight under vacuum at 120, 100 and 170 °C, respectively. The glass bottles were conducted to be mixed homogeneously at 15 rpm with the help of a self-made rotating apparatus (Fig. 31).

Figure 31   Self-made rotating apparatus for powder mixture preparation [100].

4.2.2 Reactive Extrusion

For thermal and rheological characterization tests, compact granulates of mPBT and mPBT containing 0.02, 0.04, 0.08, 0.1 and 0.25 wt% additives were produced via reactive extrusion.

A tandem extrusion line from Dr. Collin GmbH (Ebersberg, Germany) (twin-screw extruder [A-extruder] with 25 mm screw diameter and L/D= 42; single-screw extruder [B-extruder] with 45 mm screw diameter and L/D= 30) equipped with a round-die having a diameter of 3 mm was used. To better compare the compounded materials with the final foam samples, the same machine and similar temperature profiles were conducted to keep the thermal histories constant. Prior to processing, PBT granulates were dried overnight at 120 °C. For the processing of each compound, dried powder mixtures comprising the respective amount of PBT, CE and additive were fed by a powder hopper, while the PBT granulates were fed by a granulate hopper to the A-extruder. Uniform dissolution of BTAs or dispersion of HNT in the PBT melt as well as the post-modification of PBT with the CE took place in the A-extruder. A maximum temperature of 260°C at the A-extruder was selected to assure the complete solubility of BTA in the polymer melt. After cooling the polymer melt mixture in the B-extruder, the strand was quenched in a water bath and subsequently granulated with the help of a granulator. To remove the excess water, the granulates were then dried overnight at 80 °C. The standard temperature profiles (with a deviation of ± 5 °C) and parameters for the compounding of the materials are listed in Table 5.

Table 5   Parameters for reactive extrusion of the materials.

Throughput [kg/h]	5
Screw speed at A-extruder [rpm]	135-145
Temperature profile at A-extruder [°C]	35, 180, 210, 230, 250, 260, 260, 260, 260, 260, 260
Screw speed at the B-extruder [rpm]	6-8
Temperature profile at B-extruder [°C]	236, 231, 230, 230, 230, 230
Melt temperature at the die [°C]	232-236
The temperature at the die [°C]	250

4.2.3 Compression Molding

The specimens for rheological characterization were prepared by compression molding. For plate-plate shear rheology measurements, circular samples with a diameter of 25 mm and a thickness of 2 mm; for extensional viscosity measurement, rectangular specimens with 10 mm

width, 18 mm length and 0.8 mm thickness were pressed by using hot/cold electrohydraulic lab presses (Weber PW10, Remschalden, Germany). Prior to compression molding, the granulated materials were dried overnight at 120 °C under vacuum. The dried granulates were first hot pressed for 2.5 mins at 260 °C with 10 kN. Then, the force was increased to 60 kN for 4 min, and subsequently cold pressed for 4 min at room temperature with 20 kN to become solidified.

4.2.4 Reactive Foam Extrusion

To produce all foams of neat mPBT and mPBT with 0.02, 0.04, 0.08, 0.1 and 0.25 wt% nanoadditive (BTA1, BTA2, HNT and their combinations), the same tandem extrusion line was used. Powder mixtures of PBT, CE and additive were fed by powder hopper. As in the reactive extrusion, the overnight-dried PBT granulates were hopped at the same position. As a physical blowing agent, 2 wt% sc-CO_2 was injected into the polymer melt mixture using a positive displacement syringe pump connected to a gas-dosing unit (Maximator DSD 500, Nordhausen, Germany). Intimate mixing of CE, additive and sc-CO_2 was provided in the A-extruder under pressure. The highest temperature in the A-extruder was set as 260 °C to assure the dissolution of BTA1 and BTA2. The temperature profile was kept the same to produce HNT-based mPBT foams to compare the effect of additives on the final properties of the foams. The melt mixture was transferred to the B-extruder for cooling down to the melt temperature providing optimum foamability, foam morphology and properties. The detailed optimization study, where melt temperatures were varied to define process temperature window and parameter optimization, is described in the results and discussion chapter *(see Chapter 5.1.3 and 5.2.1)*. Cylindrical foam strands were obtained by using a round die with a diameter of 3 mm. At the exit of the die, the foam samples were collected with the help of a conveyor belt (SK25-K55, Schulz Fördertechnik GmbH, Waldmohr, Germany). The standard temperature profiles (with a deviation of $\pm$ 5 °C) and parameters for the foaming of the materials are listed in Table 6.

Table 6   Parameters for reactive foam extrusion of the materials.

Throughput [kg/h]	4
Screw speed at the A-extruder [rpm]	135-145
Temperature profile at the A-extruder [°C]	35,180,210,230,250,260,260,260,260,260,260
Screw speed at the B-extruder [rpm]	6–8
Temperature profile at the B-extruder [°C]	223, 218, 217, 217, 217, 217
Melt temperature at the die [°C]	223-227
Temperature at the die [°C]	235
Pressure at the exit of the die [bar]	90-140

4.3 Material Characterization

4.3.1 Thermal Analysis

In this thesis, differential scanning calorimetry (DSC) was used to determine the melting and crystallization behavior of the materials. The measurements were performed using a Mettler Toledo DSC/SDTA 821 e (Columbus, United States). The standard method consists of a heating-cooling-heating cycle in a temperature range from 25 °C to 260 °C with a heating or cooling rate of 10 K/min under nitrogen atmosphere (flow rate: 50 ml/min). Between each cycle, the temperature was kept constant for three minutes. The crystallization temperature of the samples was evaluated from the cooling cycle with the help of the Mettler Toledo STARe software.

For crystallization kinetics measurements, the method consisting of a heating-cooling cycle under nitrogen atmosphere (flow rate: 50 ml/min) was used. The temperature was ranged between 25 °C and 260 °C with a heating rate of 10 K/min. For cooling from 260 °C to 25 °C, various cooling rates of 2, 4, 8, 16 K/min were applied. Between each cycle, the temperature was kept constant for three minutes. The non-isothermal crystallization activation energies of the samples were estimated by the Kissinger equation (Eqn. 21) [176,177].

$$\frac{\mathrm{d}\ln\left(\phi/T_p^2\right)}{\mathrm{d}\left(1/T_p\right)} = -\frac{\Delta E}{R_i} \tag{21}$$

where ϕ is the cooling rate, R_i is ideal gas constant, T_p is the peak temperature, which can be determined automatically with the help of the Mettler Toledo STARe software. The crystallization activation energy (ΔE) of the samples was obtained from the slope of the plot of $\ln\left(\phi/T_p^2\right)$ versus $1/T_p$.

4.3.2 Rheological Analysis

4.3.2.1 Shear Rheology

The shear rheology measurements of the pressed circular samples (25 mm x 2 mm) were conducted using a plate-plate rotational rheometer Anton Paar MCR702 (Graz, Austria). At first, the strain where linear viscoelastic behavior is present was determined by dynamic strain-controlled sweep measurements at 260 °C, at a deformation range from 0.1 to 100 %, at a frequency of 1 rad/s. Afterward, the complex viscosity of the samples was measured within the linear viscoelastic region at 260 °C by frequency sweeps ranging from 0.1 to 100 rad/s. At least three samples were tested to minimize the experimental errors.

4.3.2.2 Start-up Shear Experiments

Start-up shear experiments for each pressed circular sample (25 mm x 2 mm) at a strain rate of 0.001 s^{-1} and a temperature of 230 °C were conducted using an Anton Paar MCR702 (Graz, Austria). These measurements were performed to determine if the time-dependent transient shear viscosity ($\eta^+(t)$) of the samples exists in the linear viscoelastic region. At least three samples were tested to minimize the experimental errors.

4.3.2.3 Extensional Viscosity Fixture

The extensional viscosity fixture measurements of the pressed rectangular samples (10 mm x 18 mm 0.8 mm) were performed using a stress-controlled dynamic-mechanical rheometer (RDA III, Rheometrics Scientific, Piscataway, NJ, US) equipped with a universal extension viscosity fixture tool consists of a fixed drum and a rotating drum that winds the sample at a constant Hencky rate, measuring the force generated in the sample. The transient extensional viscosity (η_E^+ $(t, \dot{\varepsilon})$)) of the samples as a function of time was determined at 230 °C under nitrogen atmosphere. A Hencky strain rate of 1 s^{-1} was applied since strain rates during foaming processes appear around 1 s^{-1}[178,179].

Calculation of Strain Hardening Coefficient

The strain hardening coefficient S, is defined as a deviation from the Trouton relation towards higher extensional viscosities (Equation 21). According to the Trouton relation [180], the transient extensional viscosity (η_E^+ $(t, \dot{\varepsilon})$)) (from extensional viscosity measurements) equals three times the transient shear viscosity ($\eta^+(t)$) (from start-up shear experiments). Equation 22 shows the calculation of time-dependent coefficient S $(t, \dot{\varepsilon})$ [181]:

$$S(t, \dot{\varepsilon}) = \frac{\eta_E^+ \ (t, \dot{\varepsilon})}{3\eta^+(t)} \tag{22}$$

where η_E^+ $(t, \dot{\varepsilon})$ is the transient extensional viscosity as a function of time (t) and Hencky strain ($\dot{\varepsilon}$), and $\eta^+(t)$ is the transient shear viscosity in the linear viscoelastic region. The S values were calculated at t = 2 s, which is relevant to the foam extrusion process as the foam expansion time is approximately 2 s [39]. At least three samples were tested to minimize the experimental errors.

4.4 Foam Characterization

Different characterization methods were conducted for analyzing the microstructure of the foam cells and their properties. Here, it is noteworthy that cubic shaped samples with the length of

10 mm (see Fig. 24) were cut from the core of the extruded foam strands by cutting the skin layers for the determination of foam density, open-cell content and compressive strength.

4.4.1 Foam Density

Before compression tests, the bulk densities of cubic shaped foam samples were measured using an AG245 analytical balance with a density kit (Mettler Toledo, Colombus, US). The measurements were carried out by applying the water displacement method (Archimedes' principle) according to ISO 1183-1. The foam density values were then calculated from Equation 23.

$$\rho_f = \left(\frac{m_a}{m_a - m_w}\right)\rho_w \tag{23}$$

where ρ_f is foam density, ρ_w is the density of water, m_a and m_w are weights of the foam sample in air and water, respectively. At least five samples from various locations of the foam strand were measured and the average values are reported.

4.4.2 Foam Morphology

4.4.2.1 Micro-Computer Tomography (μ-CT)

The morphology of the cylindrical foam strands was visualized by μ-CT (Skyscan 1072-100kV, Bruker microCT, Kontich, Belgium) with the resolution of 5 µm/pixel. The X-ray source had an acceleration voltage of 100 kV and a tubular flow of 90 µA. The reconstructed X-ray projections of the foam strands' cross-sections were used to estimate the total foam cell areas A_t, with the aid of the software ImageJ. With the assumption of all cells being circular, the cell diameter D_C and cell density ρ_c of the foam samples were calculated from Equation 24 and 25, respectively [95].

$$D_C = 2\sqrt{A_t/\pi} \tag{24}$$

$$\rho_c = \left(\frac{N_c}{A_s}\right)^{\frac{3}{2}} \tag{25}$$

where N_c is the number of cells in the selected area and A_s is the area of the selected section. Data analysis on the cell size and density were determined based on the total number of cells per cross-section of the foam strand.

For the sake of the more precise interpretation of the compressive properties, cell edge (strut) thickness and strut length of the foam samples were determined. To determine the strut thickness, the manual size analysis was performed by using the software ImageJ on the 2D μ-CT images taken from the cross-section of the foam strands. Strut length (l_s) of the foam samples was estimated by using the following correlation (Eqn. 26) [182].

$$l_s = 0.4490280 \, D_c \tag{26}$$

4.4.2.2 Field Emission Scanning Electron Microscopy (FE-SEM)

To visualize the crystal structure of mPBT, the characteristics (length and diameter) and orientation of the BTA and HNT fibers in the cell walls and struts, the FE-SEM Zeiss LEO 1530 from Carl Zeiss AG (Jena, Germany) with an acceleration voltage of 3 kV was used. With the purpose of precise imaging, the amorphous phase of the mPBT was partially removed via the hydrolyzation process. The foam samples were hydrolyzed in a slowly stirred 10 wt% sodium hydroxide (NaOH) solution in deionized water (DI-H_2O) for 2.5 h at 110 °C. Subsequently, the hydrolyzed samples were washed with water to remove residual NaOH and overnight dried at room temperature and atmospheric pressure. Before microscopical imaging, the samples were coated with a platinum layer thickness of 0.8 nm using a high-resolution sputter coater Cressington 208HR (Watford, United Kingdom).

4.4.3 Degree of Crystallinity

The foam samples were tested by using the same DSC from *Chapter 4.3.1.* under nitrogen atmosphere with a heating rate of 10 K/min from room temperature to 260 °C. The degree of

crystallinity was then calculated with the help of the Mettler Toledo STARe software using enthalpy of fusion of 140 J/g for 100 % crystalline PBT [183].

4.4.4 Open Cell Content

Open cell content (OCC) of the foam samples were estimated in agreement to DIN ISO 4590 by using a gas pycnometer Ultrafoam 1000, UPY-15F, Quantochrome Instruments (Florida, Unites States). Cubic-shaped foam samples were replaced in a cell with a volume of 10 cm^3. The samples (placed in the closed cell) were exposed to a nitrogen atmosphere at 0.6 bar for a designated period. At least three samples from various locations of foam strand were analyzed and the average values are reported. The OCC values were then calculated based on Equation 27 [184]:

$$OCC = \left(\frac{V_{geometric} - V_{diffused}}{V_{diffused}} \right) x \; 100 \tag{27}$$

where $V_{geometric}$ is the geometric volume of the sample and $V_{diffused}$ is the volume of the sample into which nitrogen diffused.

4.4.5 Compressive Properties

Characteristic stress-strain behaviors of the cubic shaped foam samples (10 mm x 10 mm x 10 mm) were analyzed by a universal compression test machine (Z050, ZwickRoell GmbH & Co. KG, Ulm, Germany) in agreement with the test standard DIN 53421, ISO 844. The compressive loads were applied in out-of-plane direction to the foam samples. The compression strain was limited to 30 %, which was sufficient for characterizing each sample's compressive modulus and strength. The test speed was 1 mm/min with a preload of 0.5 N to assure a complete contact between the sample surfaces and plates of the test machine. To find the most representative stress-strain curve, at least eight samples per material were tested and the average compressive strength values are reported.

5   Results and Discussion

5.1   Material Analysis and PBT Modification

This chapter will determine the selection of one PBT grade showing the best rheological properties (complex and extensional viscosity). Eventually, modification of the selected PBT grade with different CE concentrations will reveal the influence of CE amount on the strain hardening behavior, foamability, and thus morphology and density of the foams. Based on the findings, optimum CE concentration will be chosen and used to modify PBT for the rest of this work. Consequently, the optimization study of the process parameters, including melt temperature at the exit of the die, will be conducted.

5.1.1   Selection of PBT Grade

Complex viscosity measurements at the maximum processing temperature under shear forces can give an insight into the melting behavior at the extruder during processing. Furthermore, extensional viscosity tests at the temperatures where the foaming at the die starts to take place might indicate the foamability of the polymer and foam stabilization. Therefore, to confirm the most suitable PBT grade for the foaming trials, it is crucial to check the rheological behavior of the materials. Figure 32a shows the complex viscosities over frequency, while Figure 32b indicates the relationship between extensional viscosities and time.
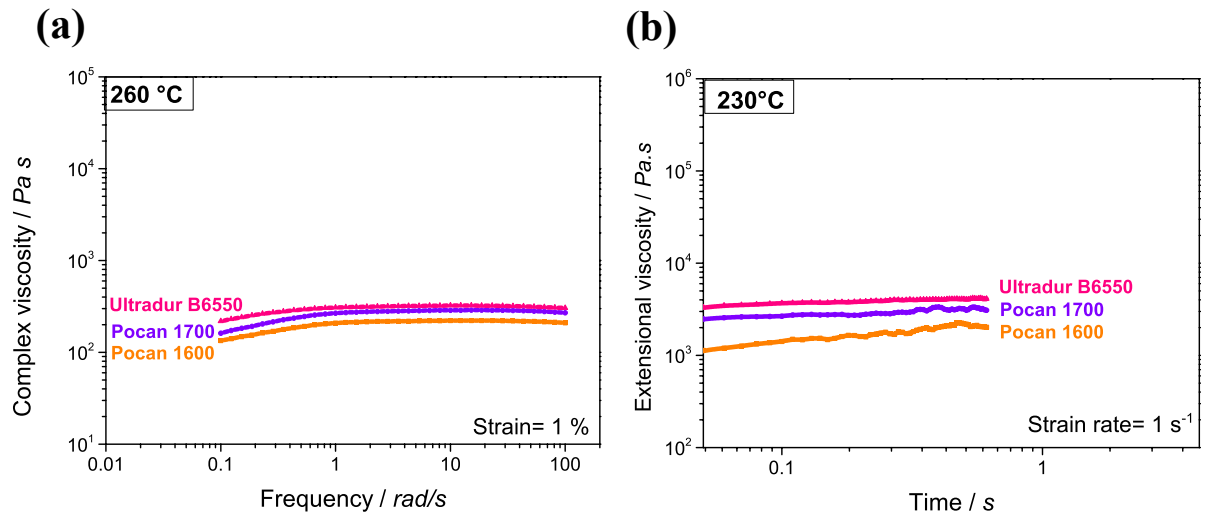
Figure 32 (a) Complex viscosities and (b) extensional viscosities of different PBT grades.

According to the complex viscosity versus frequency graph (Fig. 32a), quasi-Newtonian behavior is shown for all three PBT grades at the maximum processing temperature of 260 °C in the A-Extruder. Furthermore, Ultradur B6550 exhibits relatively higher complex viscosity values in the whole frequency range, in particular at lower frequencies, than the other grades. This can be associated with the higher molecular weight of Ultradur B6550 (M_w = 90,000 g/mol) compared to the other two grades of Pocan 1700 (M_w = 55,000 g/mol) and Pocan 1600 (M_w = 51,000 g/mol).

It is well known in the literature that linear polymers, such as PBT, show low melt strength and weak strain-hardening behavior [185]. As shown in Figure 32b, all three extensional viscosities of PBT grades increase slightly over time, exhibiting almost no strain hardening as expected. Similar to complex viscosity, Ultradur B6550 has the highest extensional viscosity due to its highest M_w. The higher the molecular weight, the more entanglements exist in polymers, making the deformation more difficult which is better for foaming.

Therefore, based on the rheological findings, Ultradur B6550 was selected as a polymer matrix for foaming for the rest of the work, which is designated as PBT in the following sections.

5.1.2 PBT Modification and Effect of CE Concentration

Influence of CE Concentration on Rheological Properties of PBT Melt

Melt properties of linear PBT can be improved through post-modification reactions, in other words, long-chain branching with CE [15]. In order to determine the optimum CE concentration in terms of complex viscosity and melt strength, four different concentrations (0.15, 0.3, 0.6 and 0.9 wt%) of CE were used for the modification of PBT. Figure 33a and Figure 33b represent the effect of CE concentration on the complex viscosity over frequency and extensional viscosity over time, respectively.
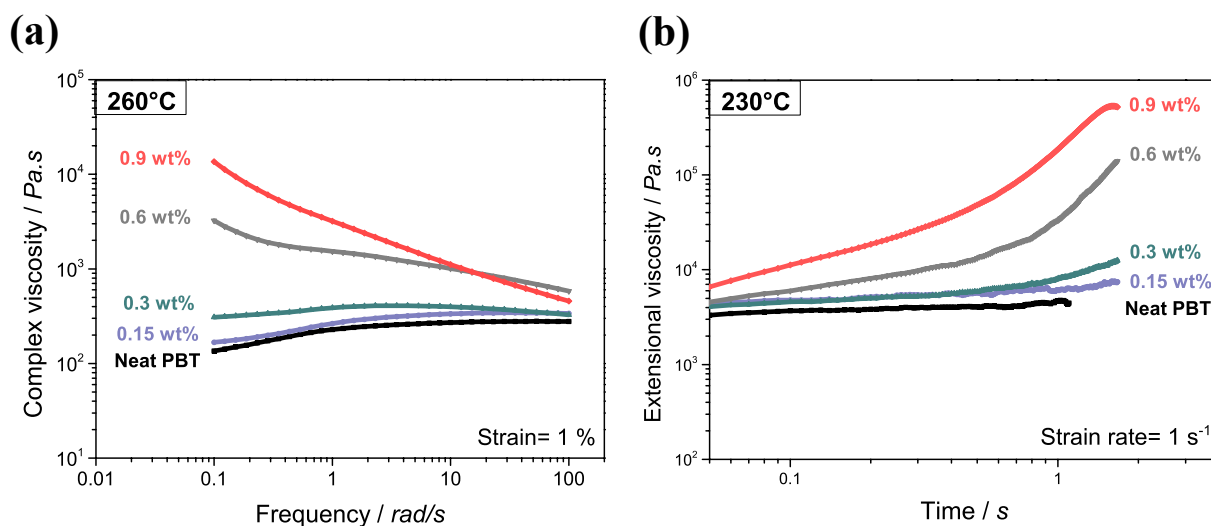
Figure 33   (a) Complex viscosities and (b) extensional viscosities of the neat PBT and PBT modified with 0.15, 0.3, 0.6 and 0.9 wt% of the epoxy-based CE.

According to Figure 33a, all modified samples exhibit an increased zero-shear viscosity compared to one of the neat PBT (around 100 Pa·s), which can be attributed to the increased M_W and intrinsic entanglements in the PBT melt induced by the long-chain branching. From lowest to highest CE concentration, this effect gets more noticeable. At 0.15 wt% CE, a quasi-Newtonian behavior is present, while 0.3 wt% CE follows the Newtonian behavior, where the complex viscosity remains constant over the frequency range from 100 to 0.1 rad/s. From 0.6 wt% CE, long-chain branching starts to get more pronounced, resulting in shear-thinning

behavior, where increasing frequency leads to a decrease in viscosity. At the high-frequency range (around 100 rad/s), PBT with 0.6 wt% CE leads to slightly higher viscosity values than those of 0.9 wt% CE. This might be due to the too high melt viscosity of PBT with 0.9 wt% CE, leading to higher torque in the extruder. Therefore, the shear-induced chain scission of PBT at high frequencies and thus decreased melt viscosity occur. Similar side effects caused by the high CE concentration have already been shown elsewhere [15,186].

Chain extension or long-chain branching is one of the most strategies for polyesters, PET and PBT, as chemically modified polymer melt offers higher extensional viscosity and melt strength leading to more improved foamability and foams with more stable cells [3,15,187]. Melt strength can be correlated with the polymer's strain hardening (extensional thickening) behavior, where a quick increase in extensional viscosity with increasing time is observed. Therefore, polymer melt with more pronounced strain hardening is expected to have the highest melt strength resulting in foams with the most improved foamability as well as foam morphology. The influence of CE concentration on foam morphology will be discussed in the next section. Figure 33b shows that 0.15 wt% of the CE is not sufficient to provide a strain hardening, where the extensional viscosity remains constant over time. Although PBT with 0.3 wt% CE indicates a noticeable strain hardening, more pronounced strain hardening is visible with 0.6 and 0.9 wt% CE concentrations. This finding is compatible with the previous complex viscosity results.

Influence of CE Concentration on Foam Morphology and Density

Figure 34 exhibits the overview of the morphology of the neat PBT foam and PBT foams modified with 0.15, 0.3, 0.6 and 0.9 wt% CE together with the corresponding foam densities.
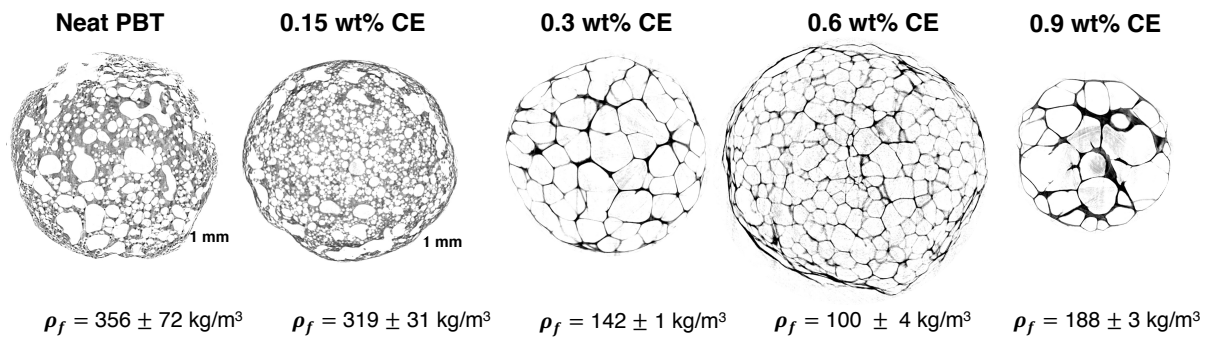
Figure 34 μ-CT images of the neat PBT foam and PBT foams modified with 0.15, 0.3, 0.6 and 0.9 wt% CE.

Neat PBT foam shows improper and coarse foam morphology with partially non-foamed areas resulting in a very high foam density of around 356 kg/m^3. This might be due to the very poor melt viscosity and strength as well as foamability. A similar finding has already been reported in Köppl`s dissertation [4]. Up to 0.3 wt% CE, almost no improvement in foam morphology and density is present, which can be attributed to an insufficient increase in complex viscosity and melt strength due to the very low amount of CE (0.15 wt%). The modification with 0.3 wt% CE features a significant decrease (around 1.6 times) in foam density while foam morphology becomes noticeably more homogeneous than those of the neat PBT and PBT with 0.15 wt% CE. Further increase in CE concentration to 0.6 wt% increases the expansion ratio leading to lighter foams with a density of around 100 kg/m^3 and increased cell density with much smaller cells. Improved foam density and morphology induced by 0.6 wt% CE might be associated with the significantly increased zero shear viscosity as well as more pronounced strain hardening behavior compared to the foams with lower CE concentrations. Surprisingly, increasing the CE amount to 0.9 wt% results in non-uniform PBT foams with a higher foam density of around 188 kg/m^3. This can be attributed to the increased torque in the extruder due to suddenly increased chain extension and intrinsic entanglements as well as deteriorated process stability. Figure 35 summarizes the influence of CE concentration on the resulting PBT foam density.
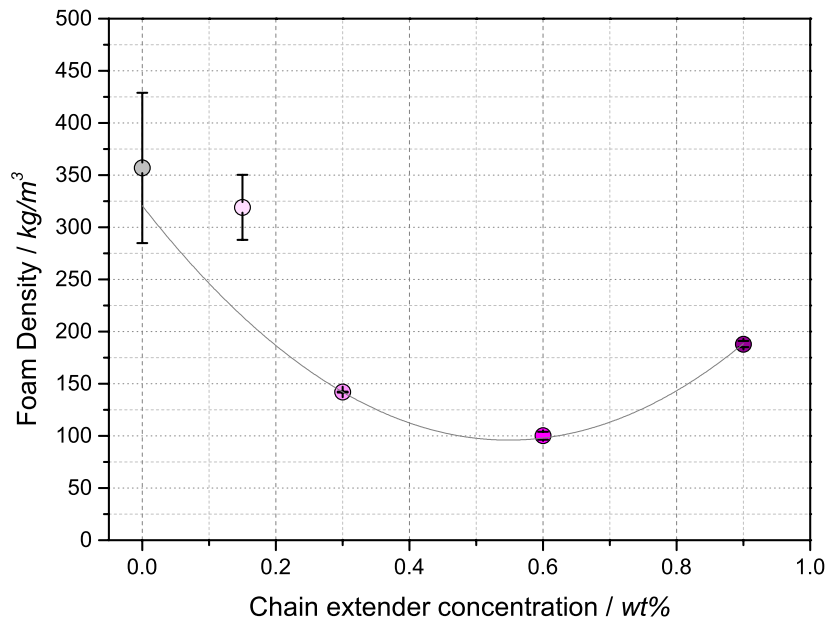
Figure 35   Foam densities of the neat PBT and PBT modified with 0.15, 0.3, 0.6 and 0.9 wt% of the epoxy-based CE.

According to Figure 35, compared to the foam density of neat PBT foam, the foam densities of all modified PBT foams are lower, which shows the necessity of modifying the PBT to reach light-weight foams. From 0.15 to 0.6 wt% CE, an increase in CE amount leads to a decrease in foam density. However, a further increase in CE concentration to 0.9 wt% causes an increase in foam density.

All in all, based on the findings from rheological, morphological and foam density analysis as well as observations during processing, 0.6 wt% CE is selected to be the optimum CE concentration for the modification of the PBT. Only modified PBT with 0.6 wt% of CE is used in the following, which is designated as mPBT.

5.1.3 Influence of Melt Temperature on the Foam Density

The significant effect of the melt temperature at the exit of the die on the foam stabilization and resulting foam density have already been reported in the doctoral study of Köppl [4]. It was claimed that a few degrees change in melt temperature results in significantly different foam densities. With this knowledge, the process optimization study was conducted for the current

material systems, such as neat mPBT and neat PBT as reference. The influence of melt temperature on the density of the neat PBT and neat mPBT foams at the constant die temperature of 235 °C is shown in Figure 36.
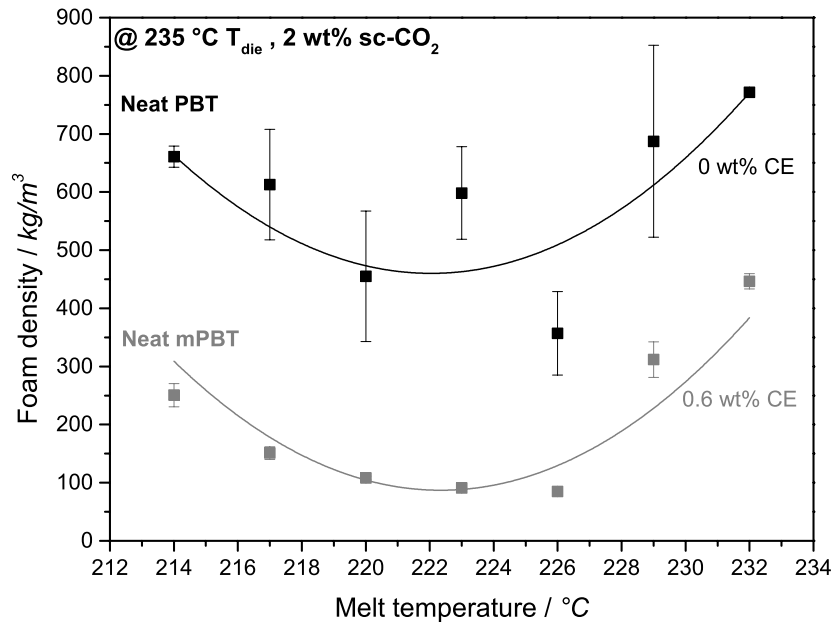
Figure 36   Change in foam density of the neat PBT (0 wt% CE) and the neat mPBT (0.6 wt% CE) by altering melt temperatures at the exit of the die at the constant die temperature of 235 °C. For the density measurements, the samples were directly cut as slices from foam strands and the solid lines are guides to the eye.

Looking at the density values of the neat PBT over the whole melt temperature range, a significant deviation in the values is visible, which might be attributed to the very narrow processing temperature window of PBT induced by very poor melt properties (Fig. 36). The smallest foam density is obtained at 226 °C. In contrast, temperatures lower than 226 °C result in increased foam densities, which might be associated with the faster solidification of the PBT melt, which restricts a proper expansion. Higher melt temperatures (> 226 °C) lead to an increase in foam density values. This might result from a noticeable decrease in melt viscosity and strength leading to fast diffusion of CO_2 out of the extrudate and cell coalescence [188].

In contrast to the neat PBT, the density values of the neat mPBT foams possess minor deviations indicating that the foam samples are more uniform. More homogeneous foams with

significantly decreased foam densities can be explained by the improved melt viscosity and strength induced by the chemical modification of the PBT. Similar to the neat PBT foams, there is an optimum melt temperature (around 226 °C), leading to the minimum foam density.

5.1.4 Summary

Among three PBT grades, Ultradur B6550 is selected as the most promising polymer matrix for foaming due to its relatively higher M_w and thus, complex and extensional viscosity values. Nevertheless, poor melt strength and foamability of the neat PBT resulted in improper foam morphology with partially non-foamed areas as well as very high foam densities (> 300 kg/m^3). Therefore, post-modification (long-chain branching) of Ultradur B6550 is found crucial to obtain low-density foams (< 100 kg/m^3). Based on rheological findings and foaming trials, among four different CE concentrations (0.15, 0.3, 0.6 and 0.9 wt%), 0.6 wt% CE is selected as optimal concentration leading to the best foaming performance and the lowest foam density of around 100 kg/m^3. For this reason, mPBT (PBT modified with 0.6 wt% CE) foams will be used as reference material for the rest of the work.

5.2 mPBT Modified with BTAs

This chapter includes, on the one hand, the understanding of the role of BTAs as a crystal nucleating agent for the mPBT resin based on the determination of the crystallization activation energies of compact mPBT samples with 0.08 wt% BTA1 and 0.02 wt% BTA2. On the other hand, the influence of type and concentrations of BTAs on the shear viscosity and strain hardening behavior of the compact mPBT will be covered in this chapter.

After understanding the effect of BTAs on crystallization behavior and melt properties of the compact mPBT, the role of BTA1 and BTA2 as a cell nucleating agent for mPBT foams at the concentrations of 0.02, 0.04, 0.08, 0.1 and 0.25 wt% will be investigated. By applying various characterization methods, the influence of BTA1 and BTA2 having different concentrations on the morphology, density, compressive properties as well as crystallinity of foams and OCC will be discussed.

5.2.1 Compact Material

Effect of BTAs on the Crystallization Activation Energy of the Compact mPBT

The extrusion foaming process of polymers takes place under non-isothermal conditions. There are close relations between the crystallization behavior of the mPBT resin during processing and the foaming quality, including foam expansion, stabilization, and resulting foam morphology and properties. Therefore, it is crucial to investigate the influence of BTAs on the non-isothermal melt crystallization behavior without blowing agent. To address this, the concentrations of 0.08 wt% BTA1 and 0.02 wt% BTA2 are particularly of interest for this section as the best foamability and foam properties are achieved with these concentrations. These will be reported in detail in the following sections.

Figure 37 shows the activation energy of the neat mPBT resin and the mPBT resin with 0.08 wt% BTA1 and 0.02 wt% BTA2. Furthermore, the activation energy of the neat PBT resin is also demonstrated to consider the effect of the post-modification on the crystallization behavior. The activation energies were obtained according to the macro-kinetic model described elsewhere by Kissinger [177].
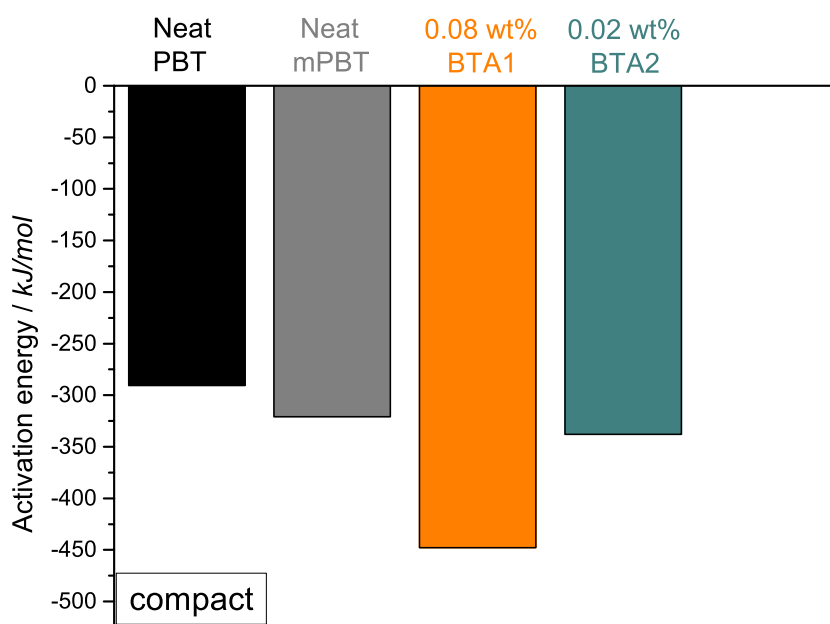
Figure 37 Crystallization activation energies of the neat PBT, mPBT resin as well as mPBT resin with 0.08 wt% BTA1 and 0.02 wt% BTA2.

The negative activation energies for non-isothermal crystallization of PBT systems (shown in Fig. 37) indicate that the crystallization mechanisms are induced by decreasing the temperature. Similarly, the negative activation energies for the non-isothermal crystallization of i-PP [189] and PBT [190] have been reported in the literature. The lower activation energy value of neat mPBT compared to the one from neat PBT indicates that the ramification, induced by long-chain branching, acts as a nucleating agent for the PBT crystals. 0.08 wt% BTA1 in mPBT leads to a significant decrease (around 40 %) in the activation energy compared to the neat mPBT showing its contribution to the crystal nucleation of mPBT. Nevertheless, the mPBT with 0.02 wt% BTA2 shows similar values with the neat mPBT, showing that BTA2 do not contribute to crystal nucleation significantly. These findings are in good agreement with the literature, where the solubility and self-assembly behavior of BTAs as well as their suitability to provide an epitaxial surface for polymer crystallization, have been studied comprehensively [171]. It was found that the resulting BTA size and nucleation efficiency are strongly dependent on the individual chemical structure of BTA. BTA1 can act as a nucleating agent and increase the crystallization temperature of PBT, while BTA2 exists as nanofibers but is not able to nucleate PBT [171]. Therefore, in this work, BTA1 is considered as a nucleating agent for both

crystal and foam cells, while BTA2 acts as only a nucleating agent for foam cells. The role of BTAs as nucleating agents for mPBT foam cells will be discussed in *Chapter 5.2.2*.

Effect of BTAs on the Complex Viscosity of the mPBT Melt

Organic nanoadditives, such as BTAs, are well-known for their ability of intimate dispersion in polymer melt without changing the melt viscosity of the polymer dramatically. However, it is noteworthy to mention that the concentration, chemical nature of the nanoadditive as well as processing conditions (e.g., temperature and pressure) play a significant role in the complex viscosity of the polymer melt.

Figure 38 depicts the complex viscosities of the neat PBT, the neat mPBT and mPBT resins including BTA1 (Fig. 38a) and BTA2 (Fig. 38b) at the concentrations of 0.02, 0.04, 0.08, 0.1 and 0.25 wt% at 260 °C. This is the maximum processing temperature in the A-extruder and at this temperature, BTAs are assumed to be present as intimately dissolved in PBT melt.

(a)   **(b)**

Figure 38 Complex viscosities of the neat PBT, the neat mPBT, mPBT with various concentrations of (a) BTA1 and (b) BTA2.
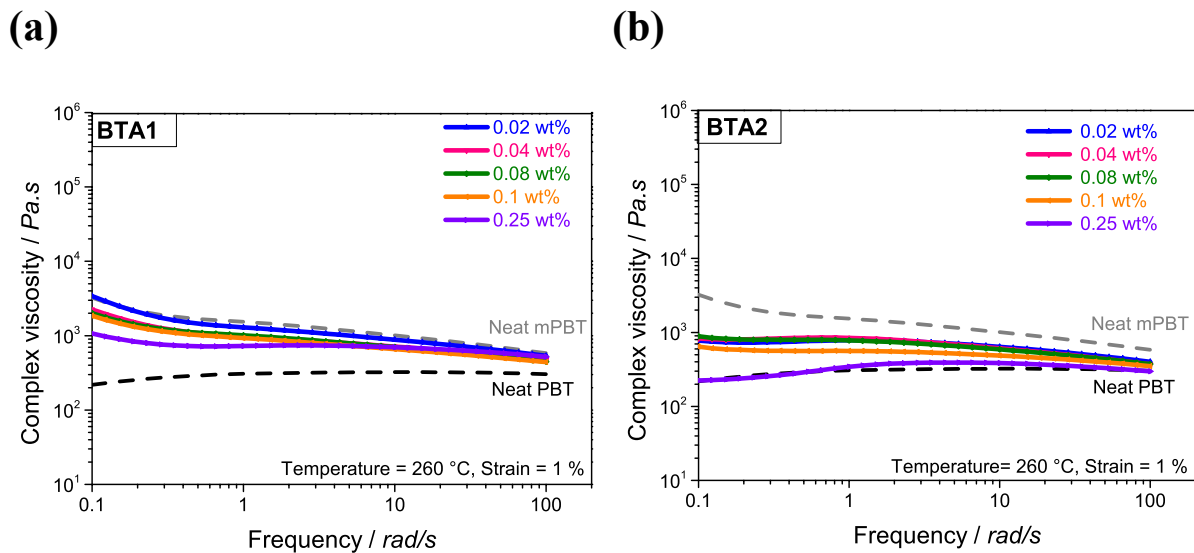
Figure 38a exhibits that neat mPBT resin and mPBT resins containing BTA1 at every concentration show pseudoplastic behavior, where complex viscosity of resins decreases with increasing frequency. This behavior is more pronounced at lower frequencies (< 1 rad/s). Looking at the flow curves of the neat PBT and mPBT resins from 1 rad/s to 0.1 rad/s, a dramatic increase in complex viscosity is visible. This is attributed to the long-chain branching of PBT in the presence of CE, getting less pronounced and negligible at higher frequency values (from 1 rad/s to 100 rad/s).

Furthermore, apart from 0.02 wt% BTA1, a change in BTA1 concentration has a noticeable effect on the viscosity values at minimum frequencies. The viscosities of mPBT resins with 0.04, 0.08 and 0.1 wt% at the lowest frequency of 0.1 rad/s are found to be very similar and smaller than those of the neat mPBT and mPBT with 0.02 wt% BTA1. Further increase in BTA1 concentration to 0.25 wt% BTA1 leads to a significant decrease in viscosity at 0.1 rad/s. This might result from an incomplete solubility of the BTA in mPBT melt due to the too high concentration. These non-dissolved remaining aggregates may interfere with the branched chains and act as a plasticizer causing a decreased viscosity at low frequencies. At higher frequencies (around 100 rad/s), the shear stress increases and is high enough to disentangle the molecules. Disentangled molecules can flow fast each other easier, thereby decreasing the viscosity. At these frequencies closer to the processing frequencies, it is assumed that the presence and the concentration of BTA1 do not influence the complex viscosity noticeably. This is one of the most crucial benefits of organic, soluble nanoadditives as they provide easy processing.

With the addition of BTA2, the pseudoplastic behavior of mPBT resins gets less pronounced than the one of the neat mPBT and the orientation of chains in the presence of BTA2 seems different than BTA1 (Fig. 38b). Like the neat PBT, the complex viscosity of the highest BTA2 concentration of 0.25 wt% BTA2 follows the quasi-Newtonian behavior. In contrast to BTA1, at the lowest frequency, a significant reduction in viscosity at a very low concentration of 0.02 wt% BTA2 compared to the neat mPBT is present. 0.04 and 0.08 wt% BTA2 also exhibit very close values of the viscosity at 0.1 rad/s to 0.02 wt% BTA2. This difference might be attributed to different solubility of BTAs in the mPBT melt resulted from their different chemical natures. An increase in BTA2 concentration to 0.1 wt% leads a to decrease in viscosity at 0.1 rad/s which is still higher than the neat PBT. Furthermore, 0.25 wt% BTA2 results in much lower viscosity value at low frequencies than BTA1 at the same concentration, which

might be induced by different chemical structures and solubilities of BTAs in mPBT melt. A dramatic decrease in viscosity at low frequency region can be explained again with the non-dissolved remaining aggregates of BTA acting as plasticizers in mPBT melt. At higher frequencies (around 100 rad/s), mPBT resins with BTA2 show similar complex viscosity values, closer to the neat PBT's viscosity than neat mPBT.

Comparing the effect of BTA1 and BTA2, both BTAs lead to a decrease in viscosity values at low frequencies compared to the neat mPBT. Up to 0.25 wt%, the change in viscosity with increasing frequency remains similar for both BTA1 and BTA2. Too high BTA concentration of 0.25 wt% results in a dramatic decrease in viscosity of mPBT resin with BTA1 at the lowest frequency of 0.1 rad/s. Apparently, this effect is seen much more pronounced for BTA2 at 0.25 wt%, causing the viscosity values similar to the neat PBT. This might be due to the interference of BTA2 in the organization of mPBT polymer chains by inhibiting the anchoring of branches, which leads to diminish of dramatic increase in viscosity at low frequencies in contrast to the neat mPBT. The different flow behaviors of the mPBT resins at the same BTAs concentration may be attributed to the different chemical structures and solubilities of BTAs in mPBT melt affecting the disentanglement of the molecules when they encounter with the shear stress.

Effect of BTAs on the Extensional Viscosity and Strain Hardening Behavior of the mPBT Melt

Extensional viscosity and strain hardening behavior of mPBT resin give significant insight into the foamability of mPBT and foam cell stabilization. The strain hardening behavior of the polymers can be quantitatively estimated. As a result, the various materials' strain hardening coefficient (S) for a particular value of time and Hencky strain is obtained. If the S value is higher, it is an indication of improved melt strength. Compared to the polymer melt with lower S, the one with higher melt strength performs better when exposed to the elongational and extensional deformations during the foam extrusion process. Therefore, superior foamability and foam stabilization and thus finer foam morphology are expected with increasing S value.

Figure 39 shows the extensional viscosity curves of the neat PBT, neat mPBT and mPBT with different concentrations of BTA1 (Fig. 39a) and BTA2 (Fig. 39b) at 230 °C and strain rate of $1\ s^{-1}$.
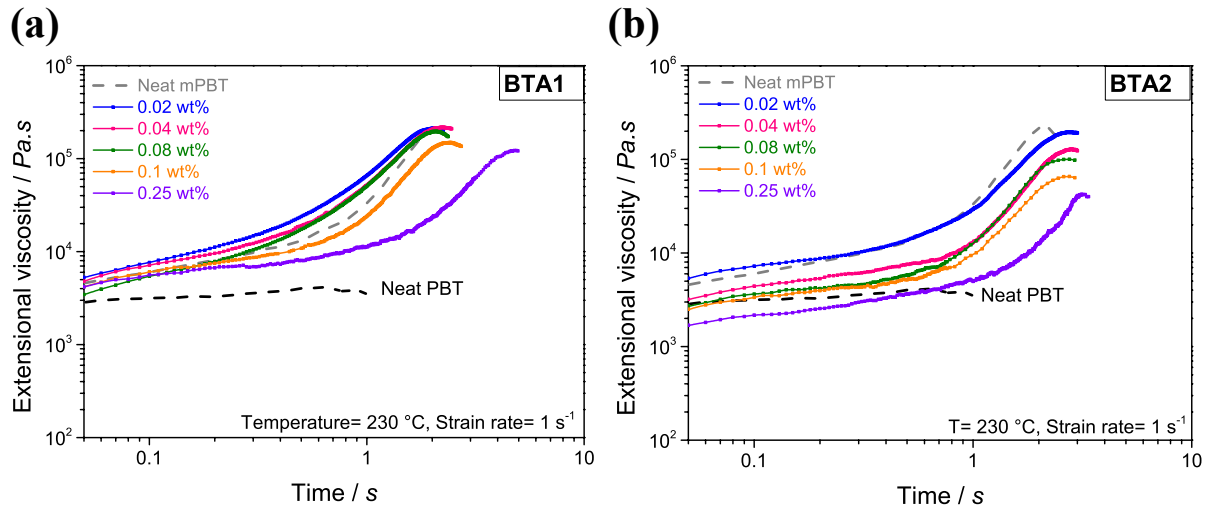
Figure 39 Extensional viscosities of the neat PBT, the neat mPBT, mPBT with various concentrations of (a) BTA1 and (b) BTA2.

Expectedly, all mPBT resins show strain hardening behavior, except for neat PBT. The effect of CE-induced long-chain branching on strain hardening behavior of PBT has already been reported in detail in *Chapter 5.1.2* and literature [15]. The addition of BTA1 with concentrations up to 0.08 wt% provides moderately higher extensional viscosities than the one from neat mPBT, as shown in Figure 39a. Further increase in BTA1 concentration to 0.1 and 0.25 wt% leads to a reduction in extensional viscosity and retarded strain hardening behavior, where a sudden increase in viscosity starts a few seconds later compared to the other materials. Similar to the complex viscosity results, the incomplete solubility of the BTA1 with too high concentration might result in decreased extensional viscosity and retarded strain hardening behavior. This might be associated with the aggregates of non-dissolved BTAs, which may interfere with the branched chains and act as a plasticizer [191]. Figure 39b exhibits the influence of BTA2 concentration on the change in extensional viscosity of the mPBT resins by time. The smallest BTA2 concentration shows similar extensional viscosity with the neat mPBT but a retarded strain hardening behavior. The sudden increase in extensional viscosity of the mPBT with 0.02 wt% is observed at around 2 s, which is an approximate time required for the expansion during the extrusion foaming process [39]. Therefore, this retardation with 0.02 wt% BTA2 might be considered beneficial for the expansion and stabilization of the foam during processing and thus resulting in a better foam morphology. The BTA2 concentrations larger

than 0.02 wt% result in a significant decrease in extensional viscosity compared to those of the neat mPBT and mPBT with 0.02 wt% BTA2. A retarded strain hardening behavior and much lower viscosity are noticeable with the 0.25 wt% BTA2, which may be attributed to the similar case seen in BTA1.

To analyze the influence of BTAs on melt strength quantitatively, S values of the mPBT resins were determined, as described in *Chapter 4.3.2*, for Hencky strain rate of 1 s^{-1} and a time of 2 s. Figure 40 depicts the calculated S values of the neat mPBT, mPBT with 0.02, 0.04, 0.08, 0.1 and 0.25 wt% BTA1 and BTA2.
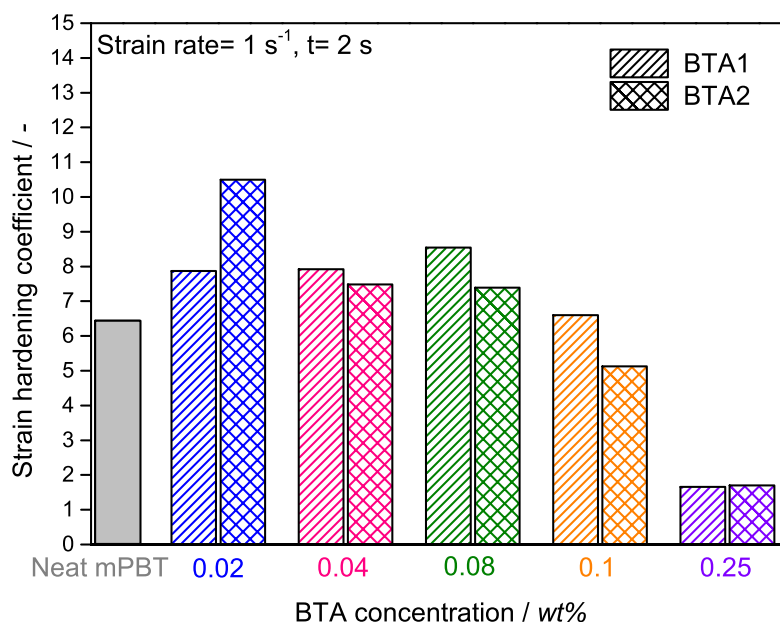
Figure 40 Strain hardening coefficients of the neat mPBT, mPBT with various concentrations of BTA1 and BTA2 for a Hencky strain rate of 1 s^{-1} and a time of 2 s.

Below 0.25 wt%, BTA1 enhances melt strength where the S coefficients are larger than the neat mPBT. The S coefficient value gets larger with increasing BTA1 concentration from 0.02 to 0.08 wt%. The maximum increase of 32 % is achieved with 0.08 wt% BTA1 compared to the neat mPBT. Further increase in BTA1 concentration to 0.1 wt% features decrease in S value. It gets much smaller (lower than the neat mPBT) at 0.25 wt% BTA1, which can be explained by the lower extensional viscosity and retarded strain hardening behavior. A similar phenomenon

is also present with the S coefficient of mPBT with 0.25 wt% BTA2. Furthermore, compared with the neat mPBT, the highest increase of 64 % in melt strength is obtained with 0.02 wt% BTA2. The larger concentrations of 0.04, 0.08 and 0.1 wt% as well as 0.25 wt% BTA2 result in lower S values and thus deteriorated melt strength. It is believed that the different BTA concentrations (0.08 wt% for BTA1 and 0.02 wt% for BTA2) leading to maximum S coefficients are associated with the difference in chemical structures of BTAs. For instance, BTA1 is based on 1,3,5-triaminobenzene and shows better solubility than BTA2 trimesic acid in PBT melt [171]. The different solubilities, concentrations and cooling rate of BTAs affect the self-assembly behavior and thus resulting fiber diameter [171].

All in all, it can be assumed that a percolated network like BTA fibers having sub-micron diameters in polymer melt are able to provide an additional improvement of the melt strength of mPBT.

5.2.2 Foamed Material

Effect of BTAs on the Process Temperature Window of mPBT Foams

The process temperature windows of the mPBT resins with the BTA concentrations leading to the highest melt strength values are established and depicted in Figure 41. The melt temperatures of the neat mPBT, mPBT with 0.08 wt% BTA1 and 0.02 wt% BTA2 resins were varied at the constant die temperature of 235 °C.
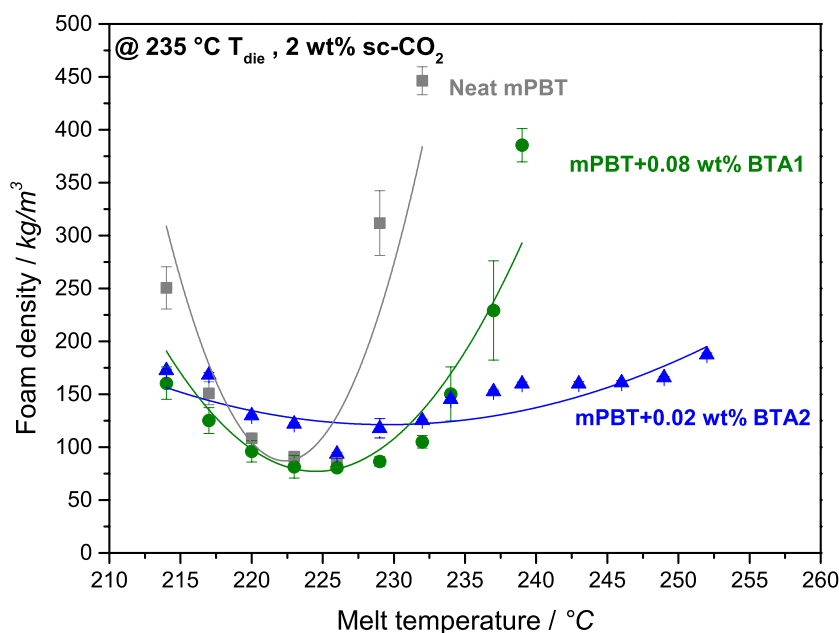
Figure 41   Change in foam density of the neat mPBT, mPBT with 0.08 wt% BTA1 and 0.02 wt% BTA2 by altering melt temperatures at the exit of the die at the constant die temperature of 235 °C. For the density measurements, the samples were directly cut as slices from foam strands and the solid lines are guides to the eye.

Looking at the curve of neat mPBT, there is only a small processing temperature window between 216 °C and 226 °C featuring the foams with a low foam density of around 100 kg/m³. Addition of 0.08 wt% BTA1 results in a more stable and broader processing temperature window (between 216 °C and 232 °C) as well as mPBT foams with a much lower foam density of around 80 kg/m³ compared to the one of the neat mPBT. A sudden increase in foam density at 234 °C might result from non-assembled or disassembled nanofibers of BTA1 at these high temperatures. Furthermore, the most stable and the widest processing temperature window in the range of 220 °C and 260 °C is obtained with 0.02 wt% BTA2. The lowest foam density of mPBT foams containing 0.02 wt% BTA2 is found as around 100 kg/m³, which is similar to the one of the neat mPBT and a little higher than the one of the mPBT with 0.08 wt% BTA1.

Noticeably, BTAs provide a wider processing temperature window of mPBT, leading to much more controlled foamability than the neat mPBT. This may be associated with the larger strain hardening coefficients induced by the presence of supramolecular nanofibers. The melt temperature range around 226 °C seems to be optimum to achieve mPBT foams based on selected concentrations of BTA1 and BTA2.

Effect of BTAs on the Morphology of mPBT Foams

To understand the influence of BTA type and concentration on the morphological properties of mPBT foams, μ-CT images of each foam specimen (in the out-of-plane direction) were reconstructed. As PBT foams based on the neat reference PBT result in very improper and coarse foam morphology as well as too high foam densities (Figure 34), it was not possible to determine average cell size and cell density from the μ-CT images of those foams. Figure 42 gives a morphological overview of the μ-CT images of the neat mPBT foam and mPBT with 0.02, 0.04, 0.08, 0.1 and 0.25 wt% BTA1 and BTA2 with the corresponding mean cell sizes, cell densities and foam densities as well as histograms of the cell sizes. All foam samples were processed at the melt temperature at around 226 °C and the die temperature of 235 °C.

Neat mPBT

743 ± 284 µm
1.4 x 10^5 cells/cm^3
81 ± 1 kg/m^3

BTA1 **BTA2**

0.02 wt%

1011 ± 433 µm
5.2 x 10^4 cells/cm^3
86 ± 2 kg/m^3

0.02 wt%

707 ± 197 µm
1.8 x 10^5 cells/cm^3
93 ± 1 kg/m^3

0.04 wt%

893 ± 350 µm
7.5 x 10^4 cells/cm^3
97 ± 1 kg/m^3

0.04 wt%

1220 ± 514 µm
2.9 x 10^4 cells/cm^3
105 ± 1 kg/m^3

0.08 wt%

689 ± 227 µm
1.5 x 10^5 cells/cm^3
80 ± 1 kg/m^3

0.08 wt%

1209 ± 433 µm
3.5 x 10^4 cells/cm^3
107 ± 2 kg/m^3

0.1 wt%

1899 ± 878 µm
8.4 x 10^3 cells/cm^3
137 ± 4 kg/m^3

0.1 wt%

1157 ± 426 µm
3.4 x 10^4 cells/cm^3
98 ± 2 kg/m^3

0.25 wt%

1288 ± 489 µm
2.8 x 10^4 cells/cm^3
99 ± 6 kg/m^3

0.25 wt%
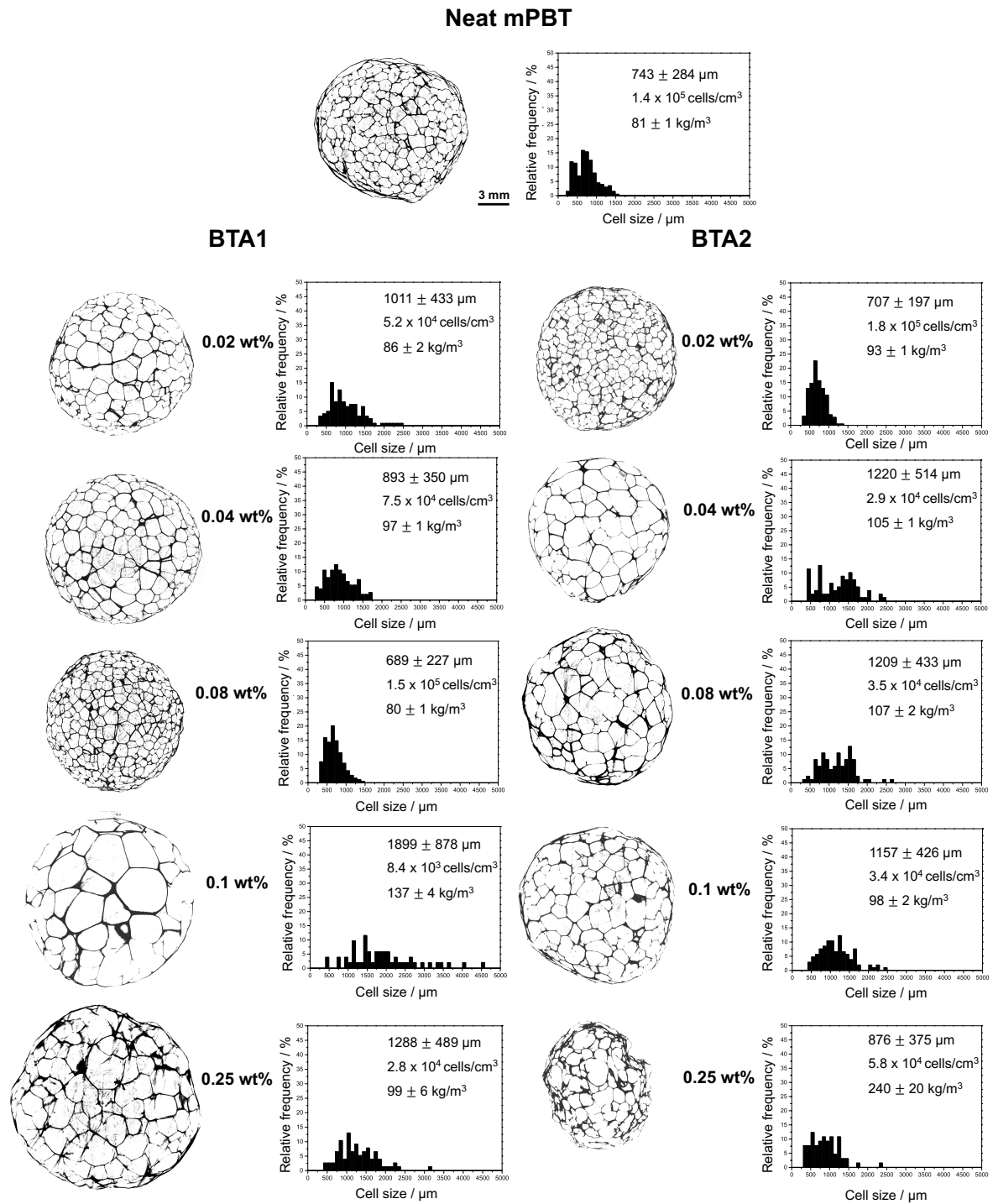
876 ± 375 µm
5.8 x 10^4 cells/cm^3
240 ± 20 kg/m^3

Figure 42 Overview of the µ-CT images, histograms of cell sizes including mean cell size, cell density and foam density of the neat mPBT foam and mPBT foams with 0.02, 0.04, 0.08, 0.1 and 0.25 wt% BTA1 (left) and BTA2 (right). The same scale bar (3 mm) is shown for all images.

As expected, the mPBT foams nucleated with the optimum BTA concentrations of 0.08 wt% BTA1 and 0.02 wt% BTA2 leading to the most stable foamability and largest strain hardening coefficients, also show the best morphology with the smallest mean cell size. Compared to the neat mPBT foams, 0.02 and 0.04 wt% BTA1 feature larger mean cell sizes with broader cell size distribution while 0.08 wt% BTA1 leads to a 7 % decrease in mean cell size of 689 ± 227 µm and foams with the highest cell density of 1.5×10^5 cells/cm³ at the similar foam densities of 80 kg/m³. To the best of my knowledge, this is the lowest achieved foam density for PBT foams with the smallest cell size and narrowest cell size distribution in literature. Much more coarse and inhomogeneous foam morphology as well as increased foam density are obtained at higher BTA1 concentrations of 0.1 and 0.25 wt%. Surprisingly, these foams with much larger cells do not show lower foam densities than those of the neat mPBT foam and mPBT with 0.08 wt% BTA1 foams. It is noteworthy to mention here that during the processing, for the sake of the process stability, the screw speed of the B-Extruder had to be adjusted to the melt properties of each material to avoid a rapid increase in barrel pressure and sudden shutdown of the extruder. Thus, at 0.1 and 0.25 wt% BTA1, the screw speed was increased to 7 rpm, while for the neat mPBT and lower BTA1 concentrations (0.02, 0.04 and 0.08 wt%), 6 rpm was used.

Nevertheless, an increase in screw speed results in larger shear forces and shorter residence time of the polymer in the extruder. As a result, worsened foam stability, cell coalescence and thus increased density mPBT foams with thicker cell walls and struts are obtained. In the case of BTA2, 0.02 wt% leads to the smallest cell size of 707 ± 197 µm and highest cell density of 1.8×10^5 cells/cm³ and the narrowest cell size distribution compared to those of the neat mPBT foam and mPBT foams at higher BTA2 concentrations. Similarly, an increase in BTA2 concentration features foams with larger cells and relatively higher foam densities.

Effect of BTAs on the Deformation Mechanism and Compressive Properties of mPBT Foams

Similar to extruded PET foams, extruded mPBT foams are also composed of an anisotropic cellular structure resulting in different deformation mechanisms when loaded in in-plane directions (a bending-dominated mechanism) and out-of-plane direction (a stretch-dominated

mechanism). As stretch-dominated wood-like cellular structures are more relevant for lightweight structural applications, the influence of BTAs on the deformation mechanism of mPBT foams in the <u>out-of-plane direction</u> is the main focus in this section [148].

Figure 43 demonstrates <u>the most representative compressive stress-strain curves</u> of the neat mPBT foam and mPBT foams with various concentrations of BTA1 (Fig. 43a) and BTA2 (Fig. 43b) together with the corresponding foam densities. For the sake of better comparison, the stress-strain curve of the mPBT with 0.25 wt% BTA2 is excluded from Figure 43b due to the very large compressive strength induced by more than 3-times higher foam density compared to the other foams. Yet, it is shown in the Appendix (Figure A1) for completeness.

(a)   **(b)**
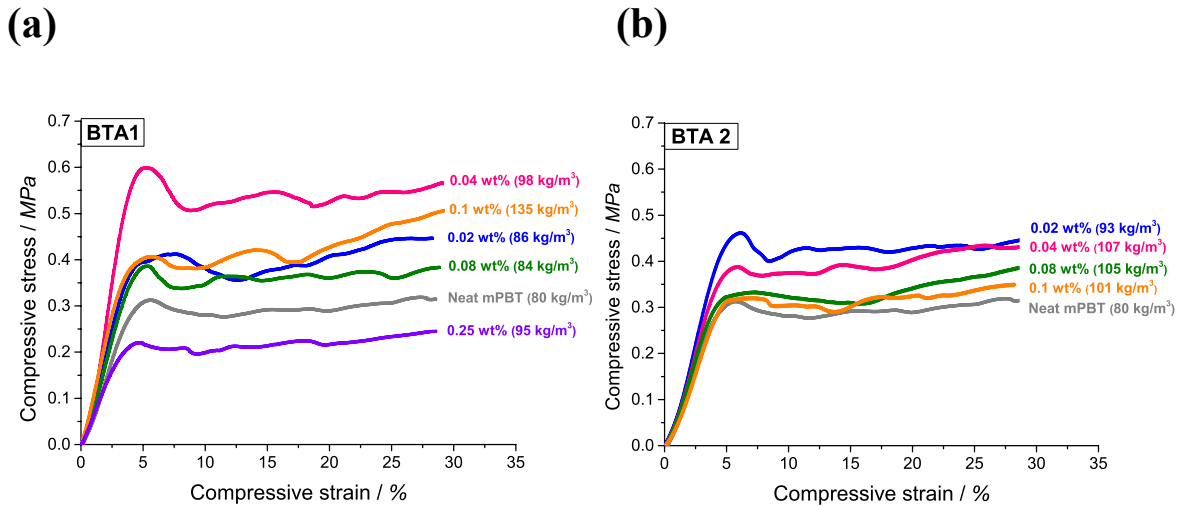
Figure 43   Compressive stress-strain curves of the neat mPBT foam and mPBT foams with various concentrations of (a) BTA1 and (b) BTA2 without 0.25 wt%.

The curves of all foam samples show a typical stretch-dominated deformation behavior (out-of-plane direction), in which (1) stress increases linearly until the yield point, (2) followed by a noticeable decrease in stress, (3) continued with variations in stress level until a sharp increase with densification due to the interlocked, irregularly elongated cells. The slope of the tangent at the linear region gives the compressive (elastic) modulus, E_f of the foam. The stress, where plastic collapse initiated by the buckling of the cells and/or plastic hinge formation, is defined as compressive strength (plastic collapse stress, σ_{pl}^*). Obviously, the compressive modulus of the foams strongly depends on foam density and elastic modulus of the cell wall material (Eqn. 18), while the compressive strength of foams is mainly affected by the ratio of the strut

thickness to strut length as well as the yield strength of the cell wall material (Eqn. 20). In addition, OCC and degree of crystallinity of the foam samples are also significant foam characteristics affecting compressive properties. Figure 44 shows the change in average compressive modulus by changing the average density of the neat mPBT foam samples and mPBT foam samples, including various concentrations of BTA1 and BTA2.
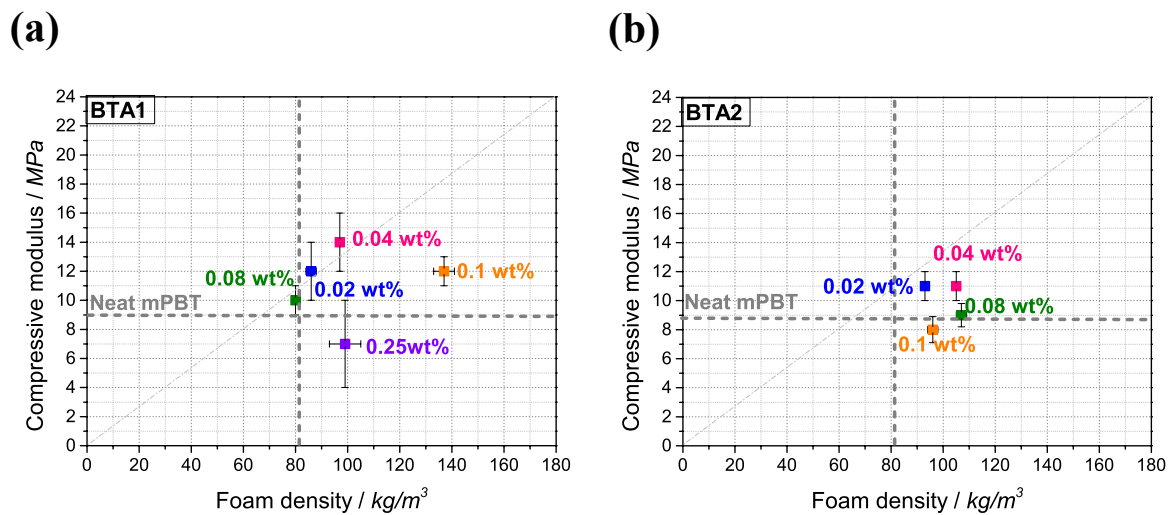
Figure 44   Change in compressive modulus with changing foam density for the neat mPBT foam and mPBT foams with (a) BTA1 and (b) BTA2 without 0.25 wt%.

Figure 44a shows that, as expected, compressive modulus gives rise with increasing foam density apart from mPBT with 0.1 and 0.25 wt% BTA1. There is a slight increase in modulus of the mPBT foam with 0.08 wt% BTA1 compared to the neat mPBT foam having the same foam density (around 80 kg/m³). It is supposed that this improvement at the same foam densities might be resulted from more homogeneous foam morphology and better orientation of the cells through the compression direction. According to Okamoto et al. [192] high-aspect-ratio nanoadditives (4 wt% clay particles) might improve the modulus to a greater extent in a foam due to the well-aligned particles along the cell walls. Nevertheless, this seems not to be the case for the systems of mPBT foam with BTAs as neither a large increase in modulus values nor the change in the degree of crystallinity of the foams compared to the neat mPBT foam is visible (Table A1). This might be attributed to the very low concentrations of BTAs in mPBT and having the elastic modulus of BTA fibers (around 2.3 GPa [193] in the same range as the one of the bulk material of PBT (about 2.6 GPa [s]). This also results in similar elastic modulus

values of the compact cell wall materials. For instance, the compact neat mPBT has an elastic modulus of 1860 ± 127 MPa, whereas mPBT with 0.08 wt% BTA1 and 0.02 wt% BTA2 show the value of 1810 ± 180 MPa and 1833 ± 123 MPa, respectively. In addition, independent from the foam density, the moduli of the mPBT foams with 0.25 wt% BTA1 (Fig. 44a) and 0.08 wt% as well as 0.1 wt% BTA2 (Fig. 44b) show a slight decrease compared to the neat mPBT foam. This might be resulted from higher OCC values induced by cell opening due to the high concentration of BTA (Table A1)[1]. Besides, the coarse and more heterogeneous foam morphology with a wider cell size distribution also leads to improper cell orientation through the compression direction and thus reduced modulus. Figure 45 demonstrates the effect of the strut thickness to strut length ratio on the compressive strength of the neat mPBT foams and mPBT foams, including various concentrations of BTA1 and BTA2.

(a) **(b)**
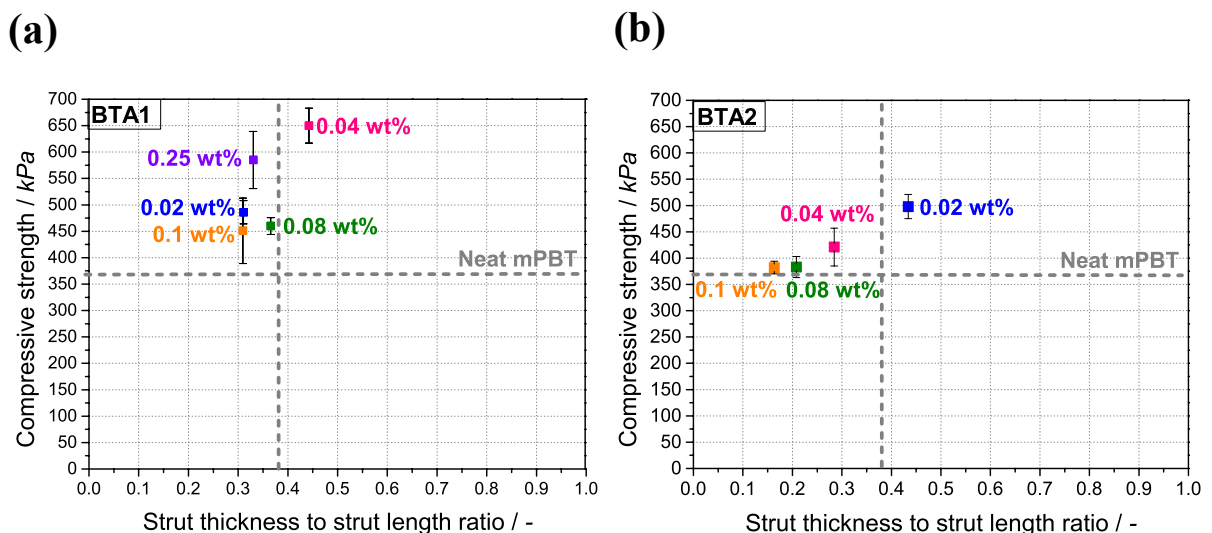
Figure 45   Influence of the ratio of average strut thickness to average strut length on the compressive strength of the neat mPBT foam and mPBT foams with (a) BTA1 and (b) BTA2 without 0.25 wt%.

According to Figure 45, no matter what type or concentration of BTA, the compressive strength of mPBT foams gives rise to the addition of the BTA fibers compared to the one of neat mPBT foam. BTA1 leads to more significant improvements in strength values, while BTA2 results in relatively smaller changes. The highest increase in compressive strength (around 76 %) is seen with 0.04 wt% BTA1, which can be correlated with the largest ratio of strut thickness to strut length, also leading to a larger foam density of around 20 % than the one of the neat mPBT

(Fig. 45a). An increase in foam density with the addition of 0.04 wt% is not desired for this study as the key challenge here is increasing compressive strength with improving the foam morphology (by lowering the mean cell size and narrowing the cell size distribution) while keeping the strut thickness to length ratio as well as the foam density, constant or very similar. Aside from that, comparing the neat mPBT foam and mPBT foam with 0.08 wt% BTA1 having almost the same foam density of around 81 kg/m^3, 0.08 wt% BTA1 features a significant increase (25 %) in compressive strength despite the lower ratio of the strut thickness to length of around 0.36 than the one of the neat mPBT (0.38).

Moreover, the yield strength values of the compact neat mPBT and mPBT with 0.08 wt% BTA1 are found as 55 ± 3 kPa and 59 ± 3 kPa, respectively. As the yield strength values of the cell wall materials, the degree of crystallinity as well as the OCC values of the neat mPBT and mPBT with 0.08 wt% BTA1 foams exhibit very similar values (Table A1), this enhancement might be attributed to the intrinsic reinforcing effect of BTA1 fibers playing a significant role in increasing buckling resistance by retarding the edge bending and face stretching. It is claimed that these percolated network-like nanofibers, located on the cell walls (Fig. 46a) and struts, contribute to the stress transfer through the foam featuring the increase in compressive strength. The similar intrinsic reinforcing effect of BTA fibers leading to the increased compressive strength of extruded PS and i-PP foams has already been reported elsewhere [26,166].

Furthermore, in the case of BTA2, the highest increase (around 35 %) in compressive strength is achieved with mPBT foam 0.02 wt% BTA2, which has higher strut thickness to length ratio of 0.43 and foam density of around 93 kg/m^3 compared to the neat mPBT foam. These higher values might mainly explain the larger strength value. Obviously, the yield strength of the (compact) cell wall material and the degree of crystallinity of the foam do not have an influence on the increased compressive strength value of mPBT with 0.02 wt% BTA2 since it has almost the same value as the one from the neat mPBT foam (Table A1). Nevertheless, it is supposed that the following factors might also contribute to the reinforcement of mPBT foam by means of the addition of 0.02 wt% BTA2:

- Improved foam morphology, including reduced mean cell size and narrower cell size distribution, compared to the neat mPBT foam
- Around 28% less OCC compared to the neat mPBT (Table A1)

- Like BTA1, the intrinsic reinforcing effect of the BTA2 fibers embedded in the cell walls (Fig. 46b) and struts increase buckling resistance by retarding edge bending and face stretching.

(a)   **(b)**
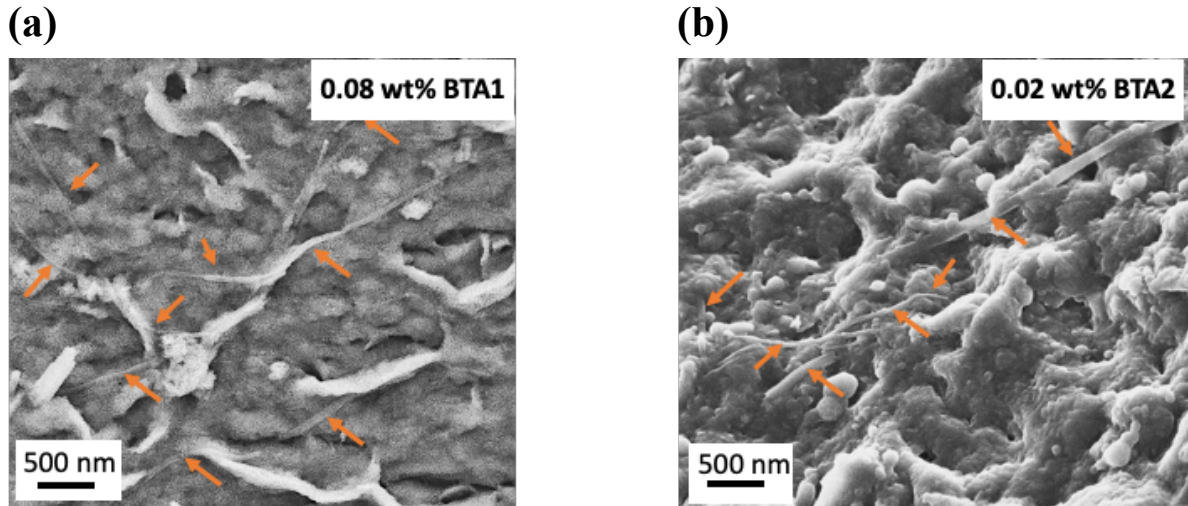
Figure 46   FE-SEM micrographs of the hydrolyzed mPBT foam with (a) 0.08 wt% BTA1 and (b) 0.02 wt% BTA2. Orange arrows on the images show BTA nanofibers on the cell wall.

Figure 46a and 46b exhibit the percolated network-like BTA1 and BTA2 nanofibers, respectively, which are embedded within the cell walls of the mPBT foams. The mean diameter of BTA1 nanofibers is found to be in the range of 75-85 nm, whereas the mean BTA2 nanofiber is around 45-55 nm. This difference might be attributed to the BTA1 concentration (0.08 wt%) being 4-times as high as the concentration of BTA2 (0.02 wt%) as well as their different solubility in the mPBT melt resulted from their different chemical natures.

5.2.3 Summary

Compact Material

Compact resins of mPBT at various concentrations of BTA1 and BTA2 were obtained via reactive extrusion. According to the crystal nucleation investigations, long-chain branching of PBT with 0.6 wt% CE leads to decrease in activation energy compared to the neat PBT. Further decrease (around 40 %) in the activation energy is observed with 0.08 wt% BTA1 whereas 0.02 wt% BTA2 do not result in significant change in activation energy value in comparison with the neat mPBT. Hence, BTA1 nanofibers serve as nucleating agent for mPBT polymer crystals while BTA2 only forms nanofibers but does not nucleate mPBT. Complex viscosity results show that use of BTAs at all concentrations leads to decrease in viscosity values at lower frequency range. This gets more pronounced with increasing BTA concentration (in particular at 0.25 wt%), which can be associated with non-dissolved aggregates of BTAs showing plasticizer effect. At higher frequency range, which is closer to processing frequencies, presence of BTAs in mPBT melt do not change the rheological properties of polymer melt dramatically. The difference in complex viscosity values at certain frequencies and additive concentrations of BTA1 and BTA2 is attributed to the different chemical nature and solubility behavior of BTAs in mPBT melt. Based on the findings from extensional viscosity fixture, long-chain branching of PBT with 0.6 wt% CE features strain hardening behavior. Use of BTA1 at the concentrations below 0.1 wt% leads to increase in extensional viscosity compared to the neat mPBT. However, higher BTA1 concentrations result in decreased viscosity values as well as retarded strain hardening. In the case of BTA2, the minimum concentration of 0.02 wt% features similar extensional viscosity with the neat mPBT whereas increase in concentration up to 0.25 wt% leads to noticeably lower viscosity values and retardation in strain hardening. Like the complex viscosity results, these decrease in viscosity values and retarded strain hardening at too high BTA concentrations are attributed to having non-dissolved aggregates due to the incomplete solubility of BTAs in mPBT melt. Comparing S coefficients of the neat mPBT resin and mPBT resins including various concentrations of BTAs, mPBT modified with 0.08 wt% BTA1 and 0.02 wt% BTA2 exhibit the highest melt strength values when compared with the neat mPBT and the other concentrations. The higher melt strength

values compared to the neat mPBT resin are explained by a percolated network like BTA nanofibers in polymer melt reinforcing the melt strength.

Foamed Material

Process temperature optimization study with a focus on foam density shows that modification with BTAs enables mPBT to have wider processing temperature window compared to neat mPBT. This features a foamability in a more controlled manner. The lowest densities of mPBT foams including BTAs are achieved at the melt temperature of around 226 °C. Besides, the morphological findings agree with the extensional viscosity curves (Fig. 39) and resulting S coefficients (Fig. 40). Therefore, it is claimed that BTAs with optimum concentration can improve the melt strength of mPBT by forming network like nanofibers in the polymer melt and provide superior foamability as well as foam morphology. Comparing the performance of BTA1 and BTA2 as nucleating agents for the cells of the best mPBT foams, both BTAs give rise to similar mean cell sizes. More uniform mPBT foams having mean cell size with lower standard deviation (707 ± 197 µm) is obtained with only 0.02 wt% (a quarter of the BTA1 concentration), whereas foams possessing much lower density (14 %) are achieved with 0.08 wt% BTA1 concentration. Compressive results show that the characteristic stress-strain diagrams of all foam samples show typical stretch-dominated deformation behavior (out-of-plane direction). The elastic modulus of the BTA-based foams is mainly affected by changing foam density. Due to the very low nanoadditive concentrations and having the modulus of BTA fibers in the same range as the bulk material, no significant changes in elastic modulus of the mPBT foams with the addition of BTAs are observed. In addition, the degree of crystallinity of all foam samples are mainly influenced by high strain induced forces during the foam extrusion process rather than BTAs. Similar behavior for i-PP foams has also been reported in the study of Mörl et al. [26]. Aside from that, OCC is another important phenomenon affecting the compressive properties of the foams. It is worthy to note that the ratio of strut thickness to strut length plays a significant role in the compressive strength of the mPBT foams. Although 0.04 wt% BTA1 leads to the highest compressive strength value due to the largest strut thickness to strut length ratio, 0.08 wt% is found to be the optimum BTA1 concentration featuring 25 % reinforcement at the same foam density compared to the one of the neat mPBT. As the yield strength of the bulk materials, OCC and degree of crystallinity values of these foams are in the same range, the improvement in the compressive strength is explained with the

finer and more uniform foam morphology as well as the intrinsic reinforcing effect of the BTA1 fibers which are embedded in the cell walls and struts making the foam more buckling resistant. Furthermore, 0.02 wt% is found to be the optimum BTA2 concentration leading to the foams with 35 % increased compressive strength compared to the one of the neat mPBT foam. It is assumed that an improved foam morphology, increased cell density, higher strut thickness to strut length ratio and foam density, lower OCC as well as the intrinsic reinforcing effect of BTA2 fibers might contribute to this reinforcement. Comparing the performance of 0.08 wt% BTA1 and 0.02 wt% BTA2 in mPBT foams, both BTAs lead to increased compressive strength values. 35 % increase (compared to the neat mPBT) is obtained with only 0.02 wt% (a quarter of the BTA1 concentration), while a 25 % increase is achieved at a much lower density (14%) with 0.08 wt% BTA1.

Considering all factors, particularly the improved mechanical performance of the foams at the low-foam density and commercial availability of the nanoadditive, mPBT foam with 0.08 wt% BTA1 is selected as the optimum material. Because it shows a significant enhancement in compressive strength at the lowest foam density among all materials.

5.3 mPBT Modified with HNTs

In this chapter, the role of insoluble nanoadditive HNTs as a crystal nucleating agent for the compact mPBT resin will be investigated by means of determination of the crystallization activation energies of neat PBT, neat mPBT and mPBT with 0.02 wt% HNT samples. After explaining the selection of HNT concentrations considering literature and BTA results, effect of different HNT concentrations (0.02, 0.04, 0.08, 0.1 and 0.25 wt%) on the rheological properties, including complex and extensional viscosity, of mPBT resin without blowing agent will be analyzed. Afterwards, the role of HNTs as a cell nucleating agent for mPBT foams at various concentrations will be covered. After implementing various characterization tests, the effect of HNTs at different concentrations on the morphology, density, degree of crystallinity, OCC as well as compressive behavior of the foam samples will be discussed.

5.3.1 Compact Material

Effect of HNTs on the Crystallization Activation Energy of the Compact mPBT

Similar to BTAs, it is significant to analyze the effect of HNTs on the non-isothermal melt crystallization behavior to determine whether inorganic nanoadditive HNTs act as a nucleating agent for PBT crystals. To do so, the impact of HNT on the crystallization activation energy of mPBT resin was determined with the help of the Kissinger macro-kinetic model [177]. 0.02 wt% HNT was selected as this concentration gives the best melt and foam properties which will be reported in detail in the following sections.

Figure 47 exhibits the activation energy of the neat mPBT resin and mPBT resin with 0.02 wt% HNT. Besides, the activation energy of the neat PBT resin and mPBT resin with 0.08 wt% BTA1 and 0.02 wt% BTA2 are also included to get a better insight into the effect of post-modification as well as the influence of different nanoadditives on the crystallization behavior.
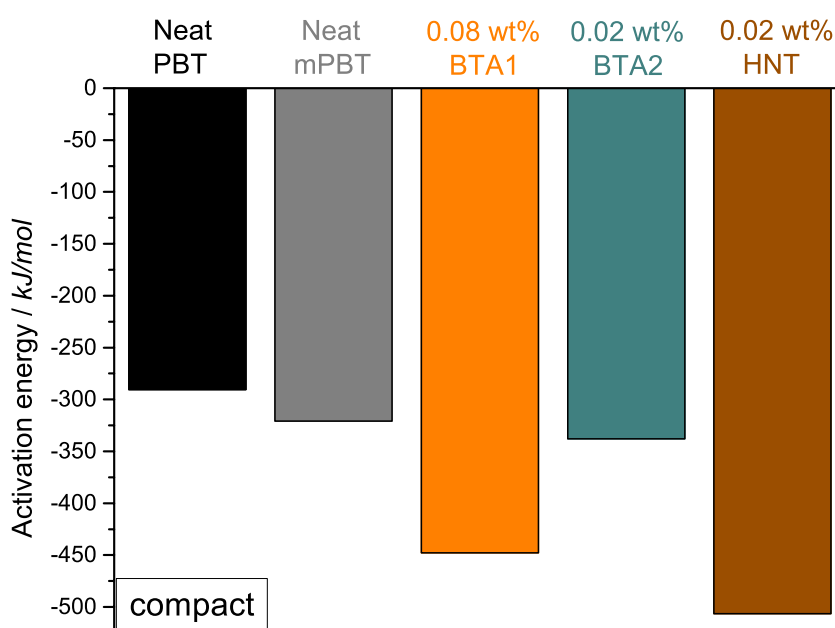
Figure 47   Crystallization activation energies of the neat PBT, mPBT resin as well as mPBT resin with 0.08 wt% BTA1, 0.02 wt% BTA2 and 0.02 wt% HNT.

Looking at the activation energies of the neat mPBT resin and mPBT with HNT, it is seen that 0.02 wt% HNT in mPBT results in a noticeable decrease of 38 %, which is even much higher than the decrease (around 20 %) induced by 0.08 wt% BTA1. Based on this finding, it can be attributed that HNTs in mPBT resin can act as nucleating agents at even very low concentrations like 0.02 wt% and contribute to the crystal nucleation of mPBT as 0.08 wt% BTA1 does. The role of HNTs as a nucleating agent for PBT and their influence on the crystallization behavior has already been reported elsewhere [194] showing that this finding is in good agreement with the literature.

Therefore, in this work, the insoluble nanoadditive HNT is considered as a nucleating agent for both crystals of mPBT resin and cells of mPBT foams. Their role as nucleating agents for mPBT foam cells will be discussed in *Chapter 5.3*.

Effect of HNTs on the Complex Viscosity of the mPBT Melt

In contrast to BTAs (organic nanoadditives), inorganic insoluble nanoadditives, like HNTs, are known for their significant contribution to conformational changes in polymer molecules affecting the rheological properties of the resin under certain circumstances. Concentration, aspect ratio of the nanoadditive as well as processing conditions are decisive parameters influencing the complex viscosity of the polymer melt. [29,34,35].

To determine whether the melt viscosity of mPBT is affected by the HNTs, the complex viscosities of the neat PBT, neat mPBT resin and mPBT resins with various concentrations of HNTs (0.02, 0.04, 0.08, 0.1 and 0.25 wt%) were determined at 260 °C and are shown in Figure 48.
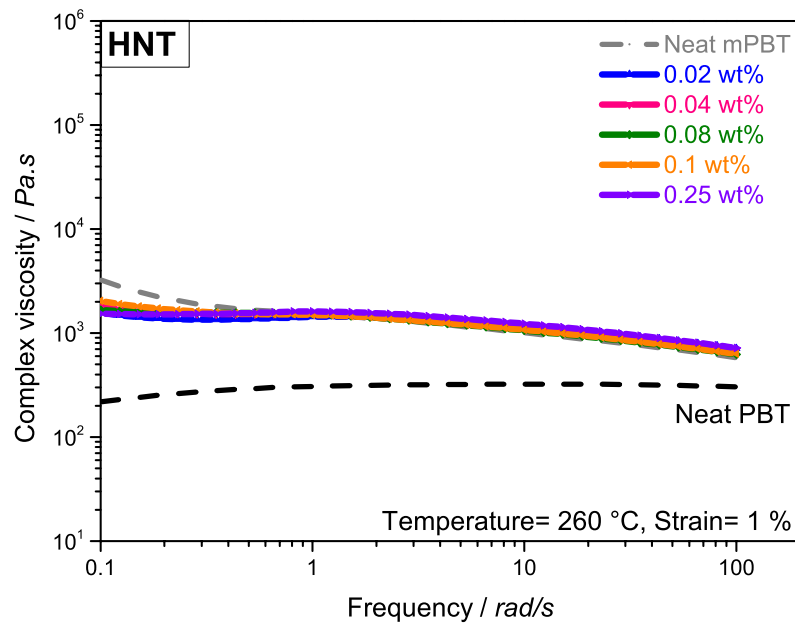
Figure 48 Complex viscosities of the neat PBT, the neat mPBT, mPBT with various concentrations of HNT.

As mentioned in *Chapter 5.1.2*, long-chain branching of the neat PBT resin with 0.6 wt% CE features an increase in melt viscosity, changing the melting behavior from quasi-Newtonian to pseudoplastic behavior. Neat mPBT resin exhibits a distinct pseudoplastic curve, whereas mPBT resins with various concentrations of HNTs possess quasi-Newtonian behavior. Looking at viscosity values of the neat mPBT and mPBT with HNTs at low frequencies, a significant drop in the viscosity of the mPBT resins due to HNTs is noticeable. This might be attributed to the interference of the nanoadditives with the branched chains leading to an increase in free volume and thus decreased intra-molecular friction and viscosity. However, at higher frequencies, the addition of the HNTs and increase in HNT concentration do not affect the complex viscosity of the mPBT as much. One can expect that the addition of insoluble nanoadditives increases the viscosity, in particular, at low frequencies, as the solid nanoadditives (second phase) in mPBT melt (first phase) are not deformable. Therefore, more stress is required to deform the polymer melt. Obviously, the HNT concentrations used in this study are not high enough to form a percolation network and dramatically increase the viscosity. However, this behavior is seen at much higher filler concentrations like 20 wt%, limiting the flow and thus processing which is not desired [195].

Effect of HNTs on the Extensional Viscosity and Strain Hardening Behavior of the mPBT Melt

To determine the role of HNTs as well as the HNT concentration on the melt strength, strain hardening behavior and foamability, extensional viscosity curves and S coefficients of the HNT-based mPBT resins were obtained in the same way as reported for the BTA-based mPBT resins (*Chapter 5.2*).

Figure 49 depicts the extensional viscosity curves of the neat PBT, neat mPBT and mPBT with different concentrations of HNTs at 230 °C and strain rate of 1 s^{-1}.
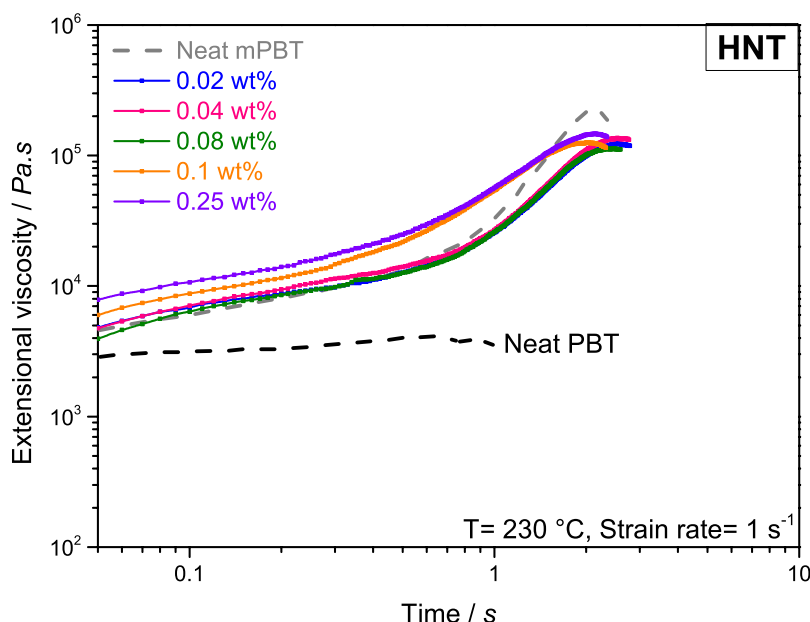
Figure 49   Extensional viscosities of the neat PBT, the neat mPBT, mPBT with various concentrations of HNT.

Looking at the curve of the neat PBT resin and the other curves, independent of the presence of HNT and HNT concentration, mPBT resins show a strain hardening behavior that might be attributed to the long-chain branching as reported for BTA-based mPBT resins. The mPBT resins with HNT concentrations up to 0.08 wt% feature similar extensional viscosity curves until the first second followed by noticeable retardation of the strain hardening closer to the time of 2 s (approximate time required for the expansion during the extrusion foaming

process [39]) compared to the one of the neat mPBT. This retardation is advantageous for the expansion and foam cell stabilization during foam extrusion to obtain foams with improved foam morphology and thus properties. Further increase in HNT concentration to 0.1 and 0.25 wt% provides significantly higher extensional viscosities than the neat mPBT until around 1.5 second. However, the neat mPBT resin exhibits more distinct strain hardening behavior resulting in higher extensional viscosities at a time of 2 s compared to the viscosities of mPBT with 0.1 and 0.25 wt% HNT. As a result, at these concentrations, worsened foamability and foam morphologies compared to the lower HNT concentrations are expected. Yet, more detailed findings of the influence of HNT concentrations on the foam morphologies will be reported in the following section. Figure 50 shows the calculated S values of the neat mPBT, mPBT with 0.02, 0.04, 0.08, 0.1 and 0.25 wt% HNT for Hencky strain rate of 1 s^{-1} and a time of 2 s.
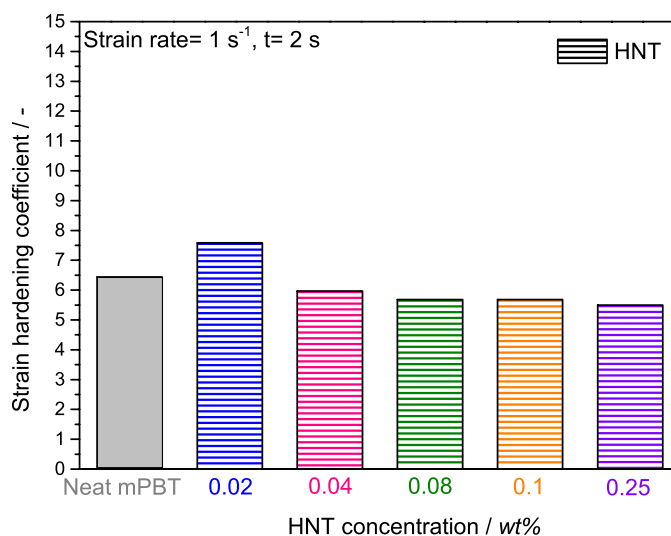
Figure 50   Strain hardening coefficients of the neat mPBT, mPBT with various concentrations of HNT for a Hencky strain rate of 1 s^{-1} and a time of 2 s.

According to Figure 50, the minimum amount of HNT of 0.02 wt% provides the highest melt strength resulting in the largest S value of around 18 % higher than the neat mPBT. Further increase in HNT concentration leads to a slight decrease in S values compared to the neat mPBT. Apparently, 0.02 wt% HNT is optimal for providing the highest melt strength for

mPBT, which might be attributed to the well dispersed and aligned nanotubes in polymer melt [196]. It is assumed that a larger HNT concentration might result in partially bigger aggregates composed of several single nanotubes and worsened HNT dispersion in the polymer melt. As a result, neither an improvement in melt strength nor larger S coefficients are present.

Based on these findings, it is expected that an improvement in foamability, best foam cell stabilization and thus finest foam morphology might be obtained with 0.02 wt% HNT concentration, whereas the other concentrations might feature foams with similar or worse foam morphologies compared to the one of the neat mPBT.

5.3.2 Foamed Material

Effect of HNTs on the Morphology of mPBT Foams

To gain an understanding of the role of HNTs as a nucleating agent for foam cells and the effect of HNT concentration on the morphology of mPBT foams, μ-CT images of each foam specimen were reconstructed identically with BTA-based foam samples. Figure 51 exhibits the morphological overview of the neat mPBT foam and mPBT foam with 0.02, 0.04, 0.08, 0.1 and 0.25 wt% HNT, including the corresponding mean cell sizes, cell densities and foam densities as well as histograms of the cell sizes. All foam samples were processed at the melt temperature at around 226 °C and the die temperature of 235 °C.

Neat mPBT

743 ± 284 µm

1.4 x 10^5 cells/cm^3

81 ± 1 kg/m^3

HNT

0.02 wt%

330 ± 82 µm

6.5 x 10^5 cells/cm^3

81 ± 1 kg/m^3

0.04 wt%

546 ± 192 µm

2.3 x10^5 cells/cm^3

85 ± 1 kg/m^3

0.08 wt%

1372 ± 528 µm

1.8 x 10^4 cells/cm^3

108 ± 2 kg/m^3

0.1 wt%

1422 ± 597 µm

1.5 x 10^4 cells/cm^3

116 ± 1 kg/m^3

0.25 wt%

1213 ± 651 µm

3.1 x 10^4 cells/cm^3

113 ± 3 kg/m^3

Figure 51   Overview of the µ-CT images, histograms of cell sizes including mean cell size, cell density and foam density of the neat mPBT foam and mPBT foams with 0.02, 0.04, 0.08, 0.1 and 0.25 wt% HNT. The same scale bar (3 mm) is shown for all images.

Among neat mPBT and all HNT-based mPBT foams, mPBT with 0.02 wt% HNT shows the most homogeneous foam morphology having the narrowest cell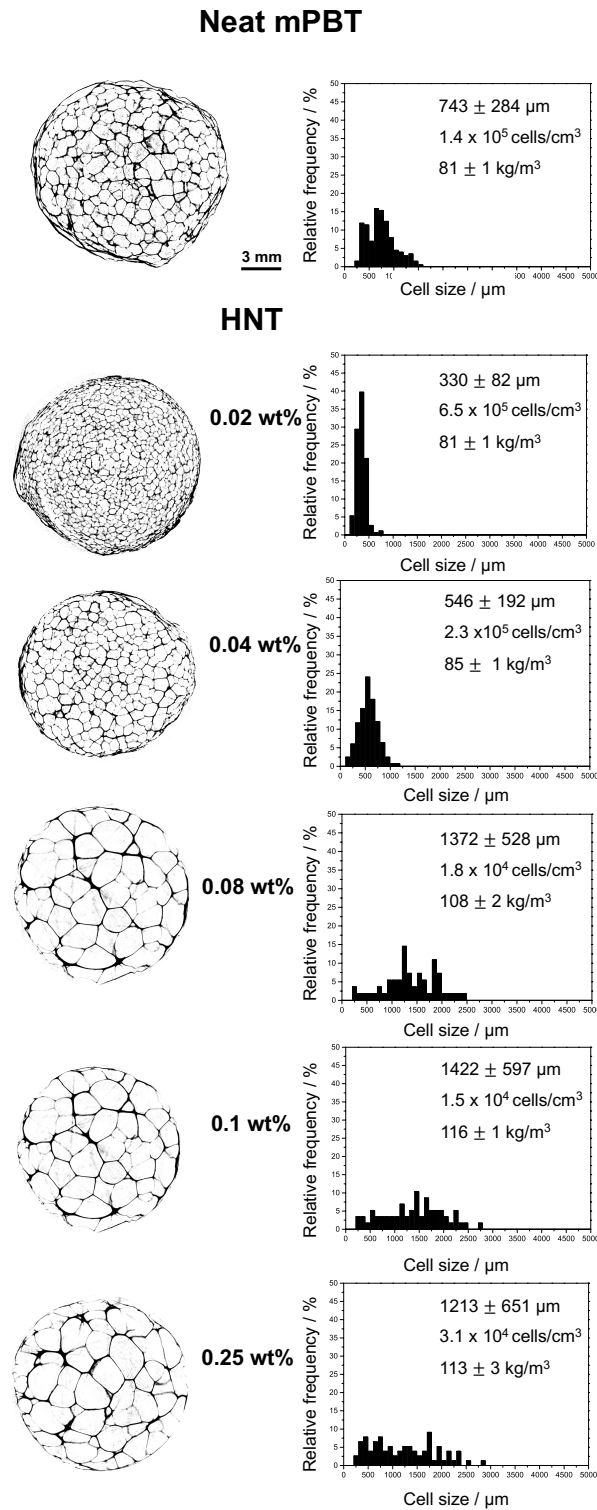 size distribution and the smallest mean cell size of 330 ± 83 µm. It is worth noting that this is half of the smallest achieved cell size of the mPBT foam with 0.08 wt% BTA1 at the same foam density. In addition, compared to the neat mPBT foam, 0.02 wt% HNT leads to around 56 % decrease in mean cell size and 3.6 times greater cell density while the foam density remains unchanged. This is advantageous for applications where low-density foams with promising mechanical properties are required. Further increase in HNT concentration results in coarse foam structure and increased foam density. This might be due to the lower melt strength and smaller S coefficients induced by HNTs at higher concentrations promoting the CO_2 diffusion, which subsequently features larger cells. Like mPBT foams with BTAs at larger concentrations, foam density does not reduce with increasing mean cell size. For better process stability, the screw speed of the B-Extruder was adjusted according to the melt viscosity of each material with different HNT concentrations to prevent a rapid barrel pressure increase. Therefore, at 0.04 and 0.08 wt% HNT and 0.1 and 0.25 wt%, the screw speed was increased to 7 rpm and 8 rpm, respectively, whereas for the neat mPBT and 0.02 wt% HNT 6 rpm was used. It is supposed that higher screw speeds lead to larger shear forces and shorter residence time of the polymer in the extruder, and thus worsened cell stabilization during foaming as well as more cell coalescence are obtained. As a result, mPBT foams with coarse morphology, including thicker cell walls and larger foam densities are present.

In short, the morphological findings agree with the S coefficients of the corresponding material. The lowest concentration of 0.02 wt% is found to be the optimum HNT concentration leading to a high number of nucleating sites, featuring mPBT foam with the finest achieved cell size and the most uniform foam morphology at the lowest foam density so far.

Effect of HNTs on the Deformation Mechanism and Compressive Properties of mPBT Foams

This section aims to understand the effect of HNT concentration on the stretch-dominated deformation mechanisms of the mPBT foams loaded in the out-of-plane direction in the same manner as the BTA-based mPBT foams.

Figure 52 shows <u>the most representative compressive stress-strain curves</u> of the neat mPBT foam and mPBT foams with various concentrations of HNT together with the corresponding foam densities.
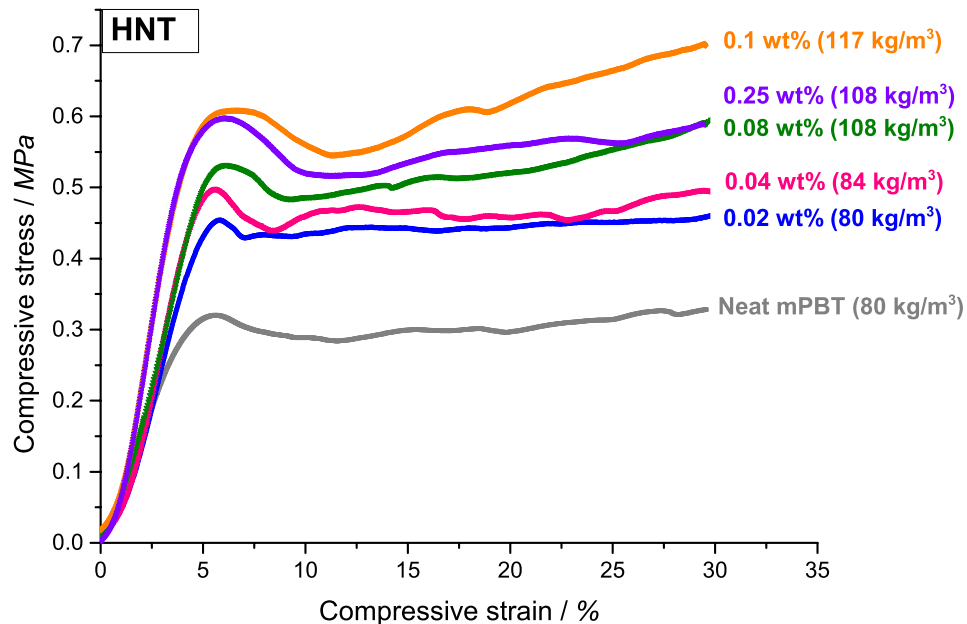
Figure 52 Compressive stress-strain curves of the neat mPBT foam and mPBT foams with various concentrations of HNT.

According to Figure 52, all mPBT foam samples follow a typical stretch-dominated deformation mechanism exhibiting curves where a linear increase until the yield point and then a remarkable decrease in stress, followed by large or small fluctuations in stress level occur Apparently, the addition of HNT leads to a noticeable improvement in compression properties, including compressive modulus and strength, of mPBT foams compared to those of the neat mPBT foam. Looking at the deformation curves of the neat mPBT and mPBT with 0.02 wt% HNT foams at the same foam densities, there is a significant reinforcement induced by HNTs. Apart from 0.02 wt% HNT, the compressive properties of the mPBT foam samples with higher HNT concentrations are proportional to the foam density values. Compressive properties, including modulus and strength values of the foams with different HNT concentrations can be found in Appendix (Table A1).

To gain a better understanding of the influence of HNT concentration on the compressive modulus of mPBT foams, average compressive modulus versus average density of the neat mPBT foam samples and foam samples with 0.02, 0.04, 0.08, 0.1 and 0.25 wt% HNT are shown in Figure 53.
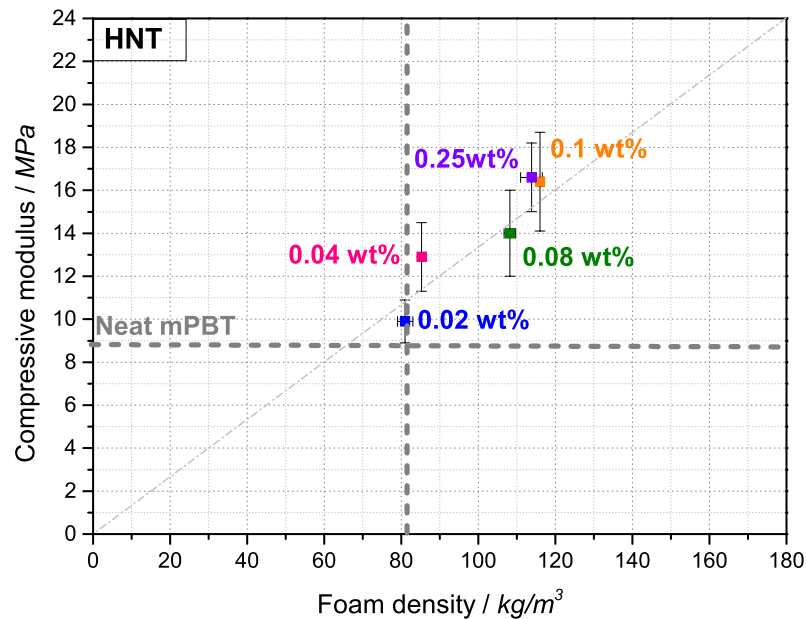
Figure 53 Change in compressive modulus with changing foam density for the neat mPBT foam and mPBT foams with HNT.

Figure 53 exhibits that the compressive modulus of the HNT-based mPBT foams strongly depends on foam density. Apart from mPBT with 0.02 wt% HNT, the modulus of the foams gives rise to increasing foam density. Looking at the neat mPBT foam and mPBT foam with 0.02 wt% HNT, both materials have the same density and the elastic modulus of the (compact) cell wall materials are in the same range (1860 ± 127 MPa for neat mPBT and 1721 ± 112 MPa for mPBT+0.02 wt% HNT). However, there is a slight increase in the compressive modulus of mPBT foam with the addition of 0.02 wt% HNT. This might be attributed to the more homogeneous foam morphology and better orientation of the cells through the compression direction. Obviously, among the other factors, larger OCC (69 ± 3 %) of mPBT foam with 0.02 wt% HNT than the one (42 ± 1 %) of the neat mPBT does not have a significant influence

on modulus values. Furthermore, it seems like at 0.04 wt% HNT, the increase in modulus is higher than expected from the higher density. This might be due to the smaller OCC value (46 $\pm$ 5 %) of mPBT foam with 0.04 wt% HNT compared to the one (69 $\pm$ 3 %) with 0.02 wt% HNT. The effect of the degree of crystallinity is not considered here as all foam samples possess values in the same range (Table A1).

Figure 54 depicts the change in the compressive strength of the neat mPBT foams and mPBT foams with 0.02, 0.04, 0.08, 0.1 and 0.25 wt% HNT with the ratio of strut thickness to strut length.
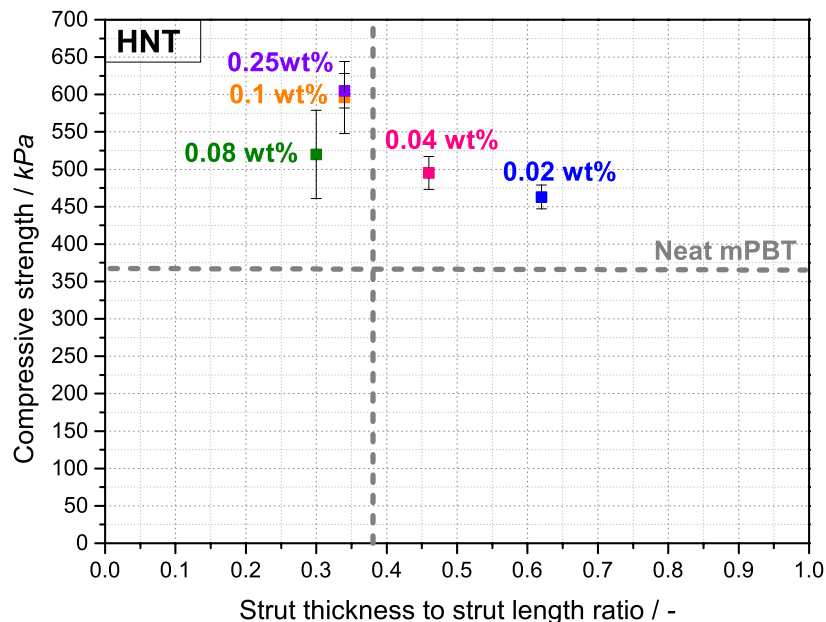
Figure 54 Influence the ratio of average strut thickness to average strut length on the compressive strength of the neat mPBT foam and mPBT foams with HNT.

As seen in Figure 54, all HNT concentrations in mPBT foam samples increase compressive strength compared to the neat mPBT. mPBT foam with larger HNT concentrations of 0.08, 0.1 and 0.25 wt% show higher compressive strength values than the one of the neat mPBT foam. This might be mainly the resulted by larger foam density values (around 38 %) despite lower strut thickness the length ratio compared to the neat mPBT. Besides, the foam sample with 0.04 wt% HNT exhibit greater strut thickness to strut length ratio as well as foam density than

the neat mPBT foam which might be the reason for the improved compressive strength. It is worthy to note that the smallest amount of 0.02 wt% HNT in mPBT leads to around 26 % improvement in compressive strength compared to the one of the neat mPBT foam at the same foam density. This might be induced by the higher ratio (63 %) of strut thickness to strut length of mPBT foam with 0.02 wt% HNT. Although this ratio is higher than those of the mPBT foams with 0.1 and 0.25 wt% HNT, the increase in compressive strength values is smaller, which might be due to the larger OCC (69 $\pm$ 3 %) of the foam with 0.02 wt% HNT. According to Wu et al. [35], larger OCC of mPBT foam with HNT might be resulted during the cell growth process when the cell walls are critically thin and are damaged by the stress induced by HNTs. This stress is occurred due to the different stretching behavior of the rigid HNT and the polymer [35]. Therefore, the largest OCC of mPBT foam with 0.02 wt% HNT might be associated with its small cell wall thickness of 37 $\pm$ 12 μm.

Furthermore, no significant influence from the yield strength of the (compact) cell wall materials as well as the degree of crystallinity on compressive strength of the foams is expected, as the yield strength values for the neat mPBT (55 $\pm$ 3 kPa) and the mPBT+0.02 wt% HNT (58 $\pm$ 3 kPa) and the degree of crystallinity values of both foams (Table A1) are in the same range. Thus, the improvement of the compressive strength with 0.02 wt% HNT is mainly attributed to the finer and very homogeneous foam morphology, including cells having a larger ratio of strut thickness to the strut length as well as an increased number of cells through compression direction compared to the reference foam. In addition, there might be an additional intrinsic reinforcing effect of HNTs dispersed and embedded in the cell walls (Fig. 55) and struts of the mPBT foam featuring an increase in buckling resistance by acting as stress transfer points through foams.

(a)

(b)
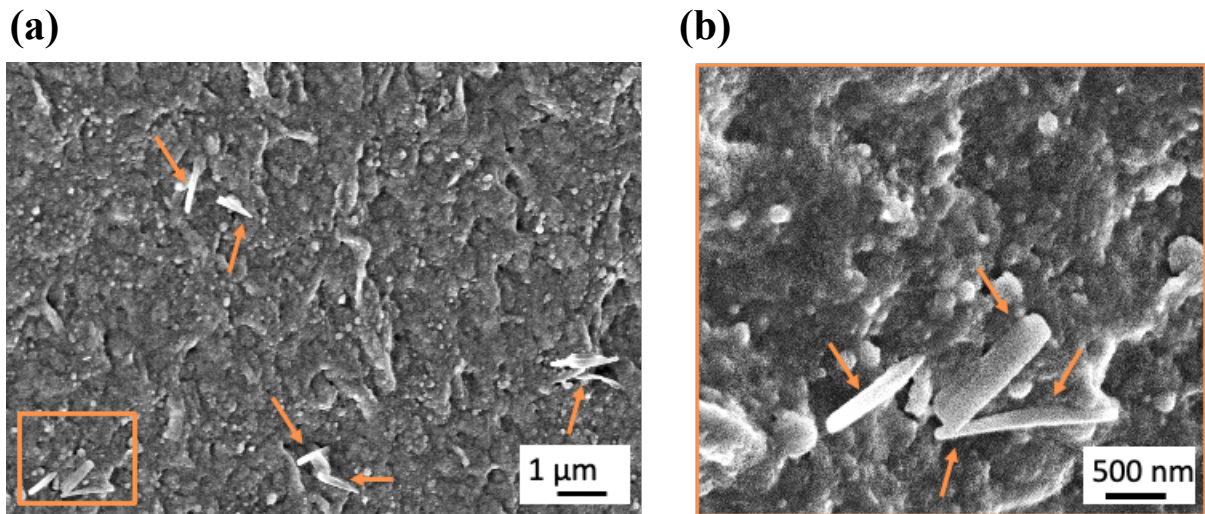
Figure 55 FE-SEM micrographs of the hydrolyzed mPBT foam having 0.02 wt% HNT with (a) lower magnification and (b) larger magnification. Orange arrows on the images show HNT nanoadditives on the cell wall.

5.3.3 Summary

Compact Material

For the sake of better comparison, mPBT resins including HNTs at the same concentrations with BTAs are produced in the same manner as BTA-based mPBT. The findings from non-isothermal melt crystallization analysis exhibits that similar to BTA1, HNT also act as nucleating agent by decreasing the activation energy of mPBT around 38 %. No matter what concentration of HNT, complex viscosity of HNT modified mPBT resins show lower complex viscosity values compared to the neat mPBT at smallest frequency of 0.1 rad/s. This is associated with the increase in free volume induced by an interference of inorganic nanoadditives with the branched chains. Nevertheless, at higher frequencies closer to the processing frequencies, the difference in viscosity gets negligible. Surprisingly the dramatic increase in complex viscosity at higher HNT concentrations are not visible as it is usually seen with inorganic insoluble nanoadditives. It is proposed that the HNT concentrations used for this work are not high enough to rise the viscosity, which is more advantageous for achieving more controlled and easier processability. Based on extensional viscosity fixture results, until the

first second, similar viscosity values are obtained with the neat mPBT and mPBT including HNT concentrations up to 0.08 wt%. Further increase in HNT concentrations leads to higher extensional viscosity values compared to the neat mPBT until 1.5 second. An advance strain hardening with these high concentrations compared to the other materials is resulted in worsened foamability. This is explained by the drop in the extensional viscosity reaching smaller values compared to the neat mPBT at around 2 s which is approximate time required for the expansion during the extrusion foaming process. Comparing S coefficients of HNT modified mPBT resins at different concentrations, 0.02 wt% is found as the optimum concentration featuring the highest melt strength.

Foamed Material

Similar to BTAs, the morphological findings and the extensional viscosity fixture results including S coefficients are found compatible. mPBT foam modified with 0.02 wt% HNT combines highest melt strength, best foamability and thus, foams having the finest cell size of 330 ± 83 μm and the narrowest cell size distribution at the same foam density with the neat mPBT. Findings from compressive tests demonstrates that all HNT-based mPBT foams follow a typical stretch-dominated deformation behavior like BTA-based mPBT foams when exposed to compressive stress in the out-of-plane direction. Elastic moduli of the foam samples strongly depend on the foam density. Apart from an HNT concentration of 0.02 wt%, the elastic modulus of the foams gets higher with increasing foam density. Yet, a slight increase in modulus with 0.02 wt% HNT is present, although the (compact) cell wall material has a similar elastic modulus as well as the foam has a similar degree of crystallinity, even higher OCC compared to those of the reference material. More homogeneous foam morphology and better orientation of the cells through the compression direction might influence the slightly increased modulus value of the mPBT foam with 0.02 wt% HNT. Looking at the compressive strength values of the foam samples, 0.02 wt% HNT is found as an optimum concentration providing foams with noticeably increased compressive strength (26 %) at the same foam density, which is quite essential for foaming applications. Considering all affecting parameters, such as the yield strength of the (compact) cell wall material, ratio of strut thickness to strut length, degree of crystallinity, OCC, the improvement in compressive strength is assigned to the improved foam morphology in which cells have a larger ratio of strut thickness to the strut length, and better oriented, increased number of cells through compression direction compared to the reference

foam. In addition, the intrinsic reinforcing effect of HNTs located in the cell walls and struts might act as stress transfer points through foams and result in an increased buckling resistance and thus improved compressive properties.

5.4 Synergistic Effects of BTAs and HNTs on mPBT Foams

So far, the influence of soluble nanoadditives (BTA1 and BTA2) and an insoluble nanoadditive (HNT) on the various properties of mPBT resin and foam has been discussed in detail. Morphological analyses show that at their optimum concentrations BTA1, BTA2 and HNTs act as nucleating agents for mPBT foam cells, providing an increased number of nucleating sites. As a result, foams with improved foam morphologies, including smaller mean cell size, narrower cell size distribution as well as higher cell density compared to those the reference (neat mPBT) foam, are achieved. Besides, it was shown that these nanoadditives improve not only the foam morphology but also compressive properties. Thus, the question is if the morphology and compressive properties of mPBT foams could be further improved by combining nanoadditives in a synergistic way. Therefore, in this chapter, four combinations of mPBT foams including **(1)** 0.08 wt% BTA1+0.02 wt% BTA2, **(2)** 0.02 wt% HNT+0.08 wt% BTA1, **(3)** 0.02 wt% HNT+0.02 wt% BTA2, **(4)** 0.08 wt% BTA1+0.02 wt% BTA2+0.02 wt% HNT are investigated and compared with the neat mPBT foam.

5.4.1 Synergistic Effects on the Morphology of mPBT Foams

To understand if different nanoadditive combinations in mPBT foams have synergistic effects on cell nucleation behavior and foam morphology, μ-CT images of each foam specimen were reconstructed as in the previous chapters. Figure 56 exhibits the morphological overview of the neat mPBT foam, mPBT foams with 0.08 wt% BTA1, 0.02 wt% BTA2, 0.02 wt% HNT and the combinations of BTA1+BTA2, HNT+BTA1, HNT+BTA2 and BTA1+BTA2+HNT, including the corresponding mean cell sizes, cell densities and foam densities as well as histograms of the cell sizes. For nanoadditive combinations, the concentrations of 0.08 wt%, 0.02 wt% and 0.02 wt% for BTA1, BTA2 and HNT are used, respectively. All foam samples were processed at the melt temperature at around 226 °C and the die temperature of 235 °C.
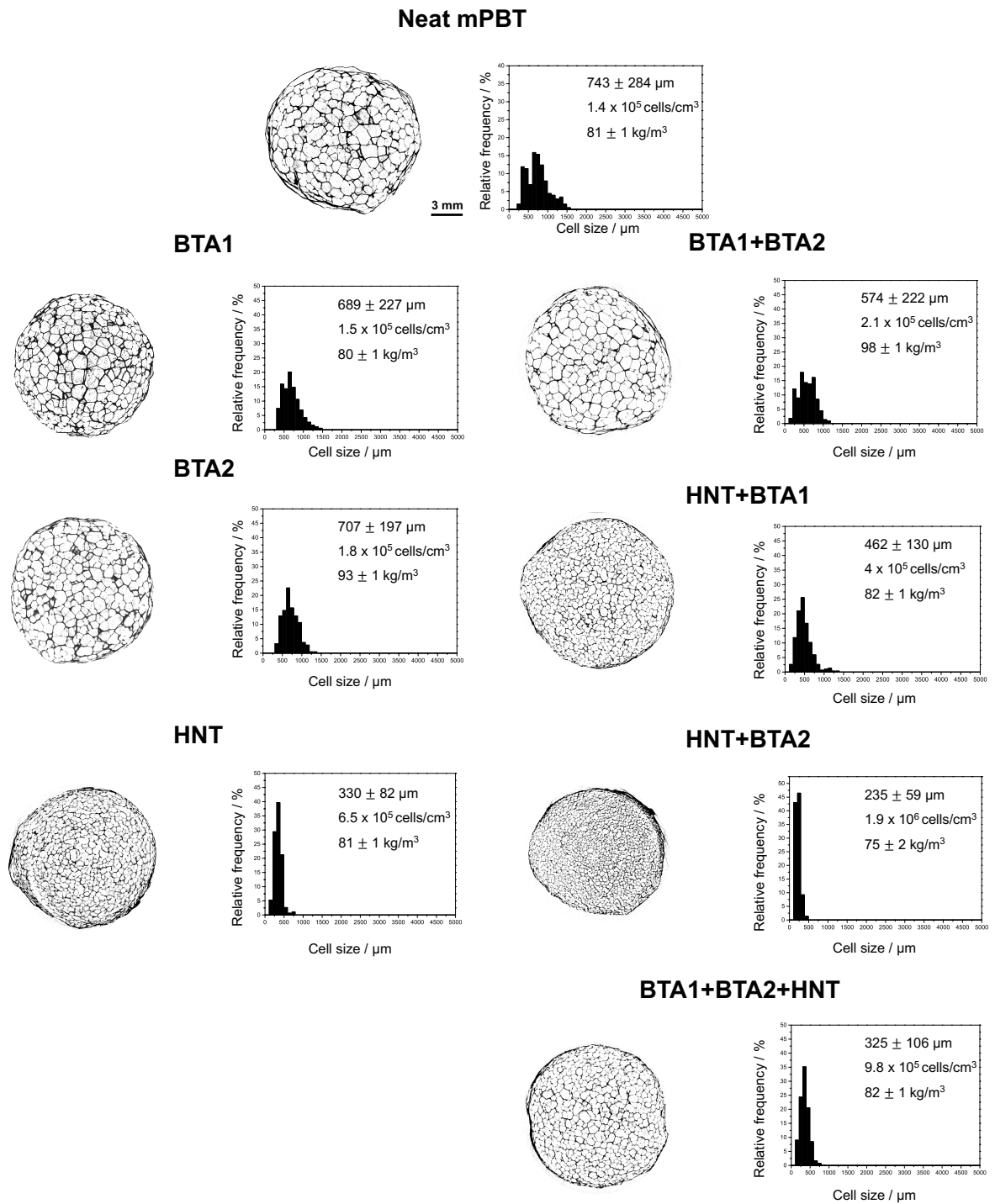
Figure 56 Overview of the µ-CT images, histograms of cell sizes including mean cell size, cell density and foam density of the neat mPBT foam and mPBT foams with BTA1, BTA2, HNT, BTA1+BTA2, HNT+BTA1, HNT+BTA2 and BTA1+BTA2+HNT. The same scale bar (3 mm) is shown for all images.

Figure 56 exhibits that apart from the combination of HNT+BTA1 and BTA1+BTA2+HNT, using multiple nanoadditives in mPBT foams promotes synergistic effects on the foam morphology resulting in smaller cells and narrower cell size distributions compared to the one of the neat mPBT foam and mPBT foam with only one type of nanoadditive. This might be associated with the high quantity of nucleating sites, given by the large surface area of BTA and HNT nanofibers enhancing the cell nucleation by reducing the free energy barrier. Nevertheless, mPBT foam containing HNT and BTA1 exhibits a larger mean cell size than the one of the mPBT foam with only HNT showing that the addition of BTA1 does not promote a synergistic effect on foam morphology. However, comparing mPBT foam only with BTA1 and HNT+BTA1, the addition of HNT to the mPBT with BTA1 results in a 33 % reduction in mean cell size. Compared to the neat mPBT foam, a combination of BTAs leads to around a 23 % reduction in cell size but a 21 % increase in foam density which is not very profitable for foam applications. Using single nanoadditive HNT instead of BTA1+BTA2 features more decrease (56 %) in cell size compared to the neat mPBT foam at the constant foam density of around 81 kg/m^3. Obviously, using two commercially available nanoadditives is more cost-effective when it comes to obtaining foams with smaller cell sizes while keeping the foam density constant.

Nevertheless, the combination of HNT with tailor-made, experimental nanoadditive BTA2 results in the largest reduction of cell size (68 %) at an even lower foam density than the reference foam. Adding BTA1 to this combination (HNT+BTA2) induces an increase in cell size and foam density. Nevertheless, the mean cell size is still around 56 % greater than the neat mPBT, while the foam density is found unchanged.

All in all, comparing all combinations, the addition of 0.02 wt% HNT and 0.02 wt% BTA2 in mPBT leads to the best foam with the mean cell size of 235 ± 59 μm, cell density of 1.9×10^6 cells/cm^3 at the foam density of 75 kg/m^3. It deserves to be mentioned that this is the finest foam morphology with the most homogenous cellular structure and smallest foam density achieved so far. This might be excellent for the insulation applications at elevated temperatures, the applications for sound absorption in the engine compartment as well as fish or seafood packaging.

5.4.2 Synergistic Effects on the Deformation Mechanism and Compressive Properties of mPBT Foams

For many foam applications, aside from fine cellular structure and lightweight, sufficient mechanical properties are also essential. Therefore, this section aims to understand if different nanoadditive combinations in mPBT foams also synergistically affect compressive modulus and strength on the foams.

Figure 57 shows <u>the most representative stretch-dominated deformation curves</u> (out-of-plane direction) of the neat mPBT foam and mPBT foams with 0.08 wt% BTA1, 0.02 wt% BTA2, 0.02 wt% HNT and the combinations of BTA1+BTA2, HNT+BTA1, HNT+BTA2 and BTA1+BTA2+HNT together with the corresponding foam densities. 0.08 wt% BTA1 is used, while for BTA2 and HNT, the concentration of 0.02 wt% is selected to be used in mPBT foams.
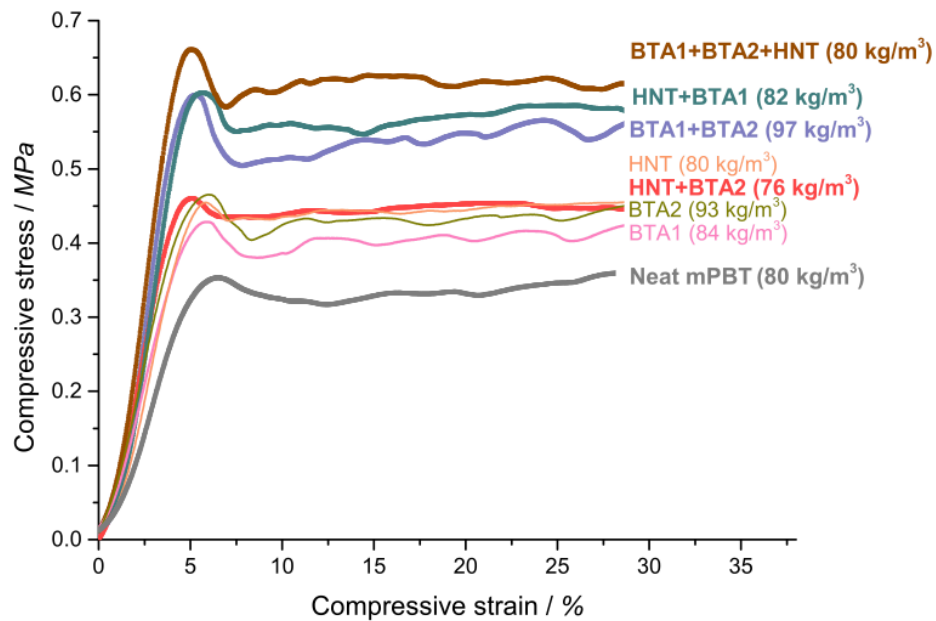
Figure 57 Characteristic compressive stress-strain curves of the neat mPBT foam and mPBT foams with BTA1, BTA2, HNT, BTA1+BTA2, HNT+BTA1, HNT+BTA2 and BTA1+BTA2+HNT.

All foam samples show characteristic stress-strain curves composed of a linear increase and the decrease in stress and a quasi-plateau region in which stress level exhibits noticeable or slight fluctuations. At first glance, looking at the deformation curves at corresponding foam densities, combining nanoadditives seems to have synergistic effects on compressive properties compared to those of the neat mPBT foam and mPBT foams with only BTA1, BTA2 and HNT.

To gain a deeper insight into the synergistic effects on the improvement of compressive properties, compressive modulus versus the density of the neat mPBT foam, mPBT foams with 0.08 wt% BTA1, 0.02 wt% BTA2, 0.02 wt% HNT and their combinations are plotted and depicted in Figure 58.
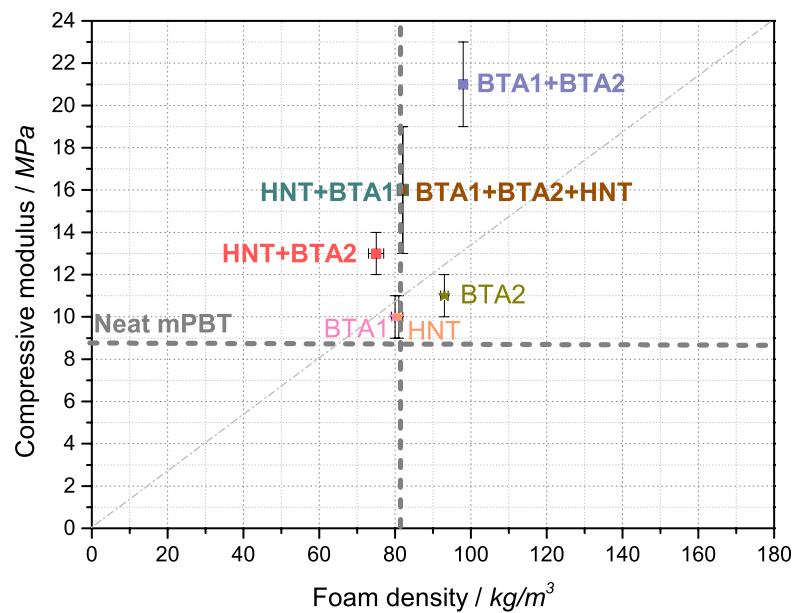
Figure 58   Change in compressive modulus with changing foam density for the neat mPBT foam and mPBT foams with BTA1, BTA2, HNT, BTA1+BTA2, HNT+BTA1, HNT+BTA2 and BTA1+BTA2+HNT.

Comparing the compressive moduli of the neat mPBT, mPBT with only BTA1 and BTA2, it is noticeable that, the combination of BTA1 and BTA2 leads to the greatest increase of 133 % in modulus of 21 ± 2 MPa, which is the highest achieved modulus in this study. There might be several reasons for this improvement, including a 20 % increase in foam density and/or

synergistic effect since OCC and degree of crystallinity values of both foams are very close. To gain a better understanding of the enhancement, the moduli of the mPBT foam with only BTA2 and the foam with BTA1 and BTA2 are compared. As a result, it is found that combining of BTAs at their optimum concentrations features a 90 % increase in modulus at the foam densities and the degree of crystallinities being in the same range. Although the OCC of mPBT foam with both BTAs is found larger than the one with only BTA2, there is a significant increase in modulus value which might be assigned to the finer foam morphology with a better orientation of the cells through the compression direction induced by synergistic effects of combining BTA1 and BTA2. In addition, looking at the combination of mPBT with HNT+BTA1, there is a significant improvement of 78 % compared to the neat mPBT and 60 % compared to the mPBT with only HNT or BTA1 in compressive modulus at the almost identical foam densities and degree of crystallinities. Here, it is believed that synergistic effects result in higher modulus for mPBT foam with the mixed nanoadditives providing an additional intrinsic reinforcing impact despite its larger OCC compared to those of the neat mPBT and mPBT with only HNT.

Furthermore, although mixing HNT and BTA2 leads to a reduced foam density of 75 kg/m^3, a noticeable enhancement of compressive modulus compared to neat mPBT and mPBT with only HNT or BTA2 is observable. This might be again attributed to the smaller and more uniform cellular structure finer foam morphology, including better orientation of the cells through the compression direction, resulted from synergistic effects. However, a mixture of all three nanoadditives in mPBT foam does not increase the compressive modulus further than the mPBT with HNT+BTA1, although 77 % improvement in modulus is present when compared to one of the neat mPBT foam. Apparently, combining BTA2 with HNT+BTA1 is not necessary to obtain foams with a higher modulus.

Besides compressive modulus, compressive strength also plays an essential role in numerous foaming applications. To determine whether synergistic effects exist on compressive strength of mPBT foams, the change in the compressive strength with the ratio of the strut thickness to the strut length of the neat mPBT foam, mPBT foams with 0.08 wt% BTA1, 0.02 wt% BTA2, 0.02 wt% HNT and their combinations are indicated in Figure 59.
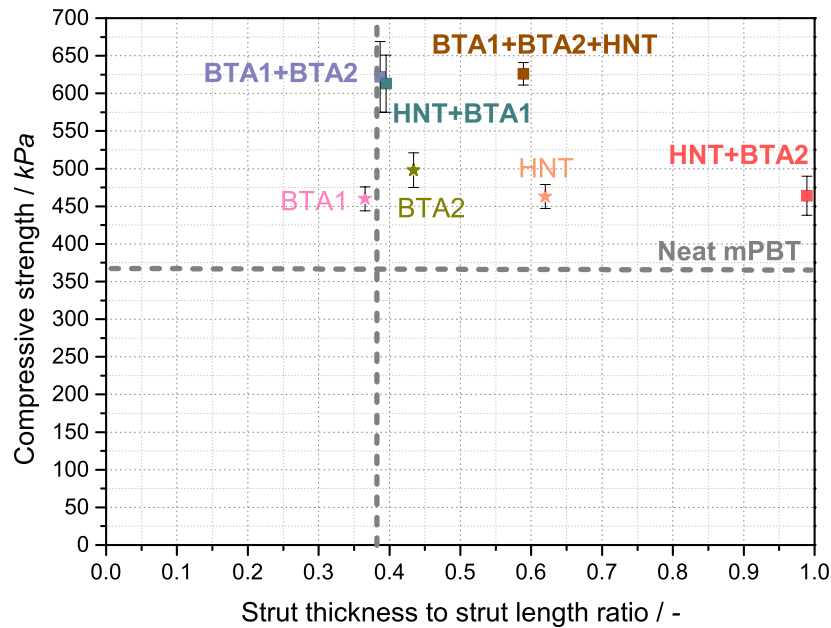
**Figure 59** Influence of the ratio of average strut thickness to average strut length on the compressive strength of the neat mPBT foam and mPBT foams with BTA1, BTA2, HNT, BTA1+BTA2, HNT+BTA1, HNT+BTA2 and BTA1+BTA2+HNT.

As in the case of the compressive modulus, mixing two types of BTAs at their optimum concentrations creates synergistic effects resulting in a significant increase in compressive strength compared to those of the neat mPBT and mPBT with only BTA1 and BTA2. It is assumed that despite the very close or slightly lower ratio of strut thickness to strut length, improved foam morphology including better-oriented cells through the compression direction plays an essential role in enhanced compressive strength. Larger foam density of the mPBT foam having two BTAs might also an impact on higher strength values. Similarly, the combination of HNT with BTA1 leads to increased compressive strength compared to the neat mPBT foam (67 %), mPBT with only HNT (32 %) and BTA1 (26 %), showing that combining these soluble and insoluble nanoadditives results in synergistic effects. Nevertheless, considering the higher compressive strength value of the mPBT foam with only BTA2, this effect could not be achieved by mixing HNT with BTA2 despite its higher ratio of the strut thickness to strut length. Lower foam density of mPBT with HNT and BTA2 than those of the foams with only HNT and BTA2 might be responsible for the slightly lower compressive strength. However, compared to the one of neat mPBT foam, the compressive strength of the mPBT foam with the combination of HNT+BTA2 is found 26 % higher. The compressive

strength of the combination of all three nanoadditives in mPBT foam lies in the same range of the values of the foams with BTA1+BTA2 and HNT+BTA1. However, among these foams, the highest compressive strength of 626 ± 15 kPa at the lowest foam density of around 82 kg/m^3 is achieved with the mixture of three nanoadditives. This improvement in compressive strength might be assigned to the synergistic effects and the high strut thickness to strut length ratio.

5.4.3 Summary

Based on the morphological results of the mPBT foams containing the combinations of multiple nanoadditives at their optimum concentrations, there is a synergistic effect. Among all combinations (BTA1+BTA2, HNT+BTA1, HNT+BTA2 and BTA1+BTA2+HNT), the best foam having the finest mean cell size of 235 ± 59 μm at the minimum achieved foam density of 75 kg/m^3 is obtained with the mixture of 0.02 wt% HNT and 0.02 wt% BTA2. The findings from compression tests show that depending on the combination, the use of multiple nanoadditives results in synergistic effects on compressive properties of the foams when compared to those of neat mPBT, and mPBT foam with the only BTA1, BTA2 and HNT. Combining BTA1 and BTA2 features the foam with the highest compressive modulus of 21 ± 2 MPa, which is the highest achieved modulus in this study. This might be attributed to the improved foam morphology (compared to the foam with only BTA2) that resulted from the synergistic effects of combining BTA1 and BTA2. Similarly, the combination of BTAs results in synergistic effects on the mPBT leading to a significant increase in compressive strength and higher density compared to those of the foams with only BTA1 and BTA2. The compressive strength of 622 ± 47 kPa at the foam density of around 98 kg/m^3 is obtained with mPBT+BTA1+BTA2 foam, whereas the highest compressive strength of 626 ± 15 kPa at the density of about 82 kg/m^3 is achieved with the mixture of all three nanoadditives. It is worthy of mentioning here that depending on the application, one must consider if it is reasonable to use all nanoadditives in terms of financial aspects to obtain foams having the compressive strength of around 620 kPa at about 82 kg/m^3 or use the mixture of BTAs for the foams having the similar compressive strength but the higher density of around 98 kg/m^3.

6 Summary

This thesis aimed to investigate mPBT foams with low foam density (< 100 kg/m^3) and improved foam morphology with a mean cell size of smaller than 500 µm via a tandem-foam extrusion process. By using organic soluble (BTAs) and inorganic non -soluble (HNTs) nanoadditives as nucleating agents for polymer crystals and foam cells, it was attempted to reach this goal. Aside from this, enhancement in compressive properties at low foam densities with the help of nanoadditives at various concentrations was set as another target that is crucial for numerous foam applications. The main scientific focus of this thesis was to establish structure-property relationships of mPBT foam strands affected by BTAs and HNT concerning melt strength, foamability and crystallization kinetics of mPBT-based resins.

First, the optimum PBT grade out of three grades was selected based on a rheological characterization test to address these aims. The findings showed that Ultradur B6550 led to the highest viscosity at the lowest frequency due to its highest molecular weight as well as melt strength which might be advantageous during processing to achieve more stable foam cells. However, pre-trials and literature showed that due to its very poor rheological properties, post-modification of PBT with CE is inevitable to achieve more straightforward and more stable foamability, better foam morphology and properties. After applying several CE concentrations for long-chain branching of PBT, 0.6 wt% was selected as optimum CE concentration featuring easiest and the most stable foamability, the lowest foam density and fine and uniform foam morphology. Findings from the process parameter optimization study exhibited that the optimum melt temperature at the exit of the die and die temperature giving the lowest foam density are around 226 °C and 235 °C, respectively.

Furthermore, the influence of organic soluble nanoadditives, including commercially available BTA1 and tailor-made BTA2, on the crystallization behavior, rheological properties of the mPBT resin was investigated. Calculating crystallization activation energies of the mPBT resins with 0.08 wt% BTA1 and 0.02 wt% BTA2 according to the Kissinger macro-kinetic model, BTA1 led to around 40 % decrease in activation energy whereas BTA2 show similar value compared to the one of the neat mPBT. Thus, it was concluded that BTA1 nanofibers could act as a nucleating agent for mPBT crystals while BTA2 nanofibers do not nucleate

mPBT. According to complex viscosity results of the mPBT with 0.02, 0.04,0.08, 0.1 and 0.25 wt% BTA1 and BTA2, use of BTAs resulted in decreased viscosity at the lowest frequencies compared to the one of the neat mPBT whereby the difference gets smaller at higher frequencies. Nevertheless, a too high concentration BTA ($\geq$ 0.25 wt%) induced a much more pronounced decrease in the complex viscosity at low and high frequencies. This was assigned to the limited solubility of BTAs at high concentrations forming non-dissolved aggregates in the mPBT melt. It was assumed that these aggregates might interfere with the branched chains and act as a plasticizer leading to decreased viscosity values.

To obtain the right BTA1 and BTA2 concentrations for optimum melt strength and thus best foamability, S coefficients of all resins were calculated according to the Trouton relation based on the transient extensional viscosity (from extensional viscosity measurements) and transient shear viscosity (from start-up shear experiments). It was found that a maximum increase of 32 % and 64 % in S coefficients were achieved with 0.08 wt% BTA1 and 0.02 wt% BTA2, respectively. Improved melt strength was associated with the percolated network like BTA nanofibers at their optimum concentrations. Moreover, the effect of BTA type and concentration on morphology, density, OCC, degree of crystallinity and compressive properties of the mPBT foams was determined. The μ-CT images of the foam samples demonstrated that 0.08 wt% BTA1 features foams with 7 % decreased mean cell size and much more homogeneous foam morphology while with 0.02 wt% BTA2, the smallest cell size of 707 $\pm$ 197 μm is obtained. This was associated with BTAs acting as nucleating agents for mPBT foam cells by increasing the number of nucleating sites and decreasing the activation energy barrier for cell nucleation. The morphology results agreed with S coefficient values showing that the higher the coefficient, the higher the melt strength, the better the foam cell stabilization and thus more improved foam morphology. In addition, the degree of crystallinity of all foam samples found within the same range shows that the high strain induced forces mainly dominate the crystallinity during the foam extrusion process. There is no noticeable effect of BTAs at these concentrations. According to compression tests, the characteristic stress-strain diagrams of all foam samples followed typical stretch-dominated deformation behavior (out-of-plane direction). The compressive modulus of foam samples was mainly dependent on the foam density and was not affected by BTAs as the modulus values of BTAs and the polymer matrix lied within the same rpvc

ange. Looking at the compressive strength values of the foams, a 25 % increase was achieved at the same foam density with 0.08 wt% BTA1 while 0.02 wt% BTA2 led to a 35 % increase at around 15 % larger foam density compared to the one of the neat mPBT. The improvement in the compressive strength with BTA1 was assigned to the finer and more uniform foam morphology as well as the intrinsic reinforcing effect of the BTA1 fibers, which are embedded in the cell walls and struts, making the foam more buckling resistant. In the case of BTA2, improved foam morphology, increased cell density and thus foam density, lower OCC as well as the intrinsic reinforcing effect of BTA2 fibers were responsible for the enhanced compressive strength. In a nutshell, mPBT foam with 0.08 wt% BTA1 (commercially available nanoadditive) was found as the most optimum material exhibiting the best mechanical performance at the lowest foam density, which is crucial for numerous foam applications.

Aside from organic soluble nanoadditives, the influence of inorganic insoluble nanoadditive HNT on the crystallization behavior, rheological properties of the mPBT were evaluated. 38 % decrease in crystallization activation energy of the mPBT resin with the addition of 0.02 wt% HNT compared to the one of the neat mPBT showed that HNTs could also act as a nucleating agent for polymer crystals like BTA1. Looking at zero viscosities of mPBT resins having 0.02, 0.04, 0.08, 0.1 and 0.25 wt% HNT, it was concluded that HNTs at all concentrations result in a noticeable decrease in viscosity at the lowest frequencies compared to the one of the neat mPBT. This was assigned to the increase in free volume and decrease in intra-molecular friction due to the interference of the HNTs with large branched mPBT chains. Nevertheless, this difference in viscosity was diminished at higher frequencies, which are close to the frequencies seen in the foaming process. Thus, it was claimed that HNTs at these concentrations do not increase the melt shear viscosity and hinder processability, which is beneficial considering the drawbacks of using insoluble inorganic nanoadditives on the processability of the polymer melts.

Furthermore, the largest S coefficient was resulted from 0.02 wt% HNT in mPBT leading to the highest melt strength and the finest and the most uniform foam morphology with the mean cell size of 330 $\pm$ 83 µm (half of the cell size of the mPBT with 0.08 wt% BTA1 at the same foam density). Improved foam morphology was assigned to the successful role of HNT as a nucleating agent for mPBT foam cells leading to an increase in the number of the nucleating sites and a decrease in energy barrier for foam cell crystallization. Further rise in HNT

concentration could improve neither melt strength nor foam morphology. It was concluded that the morphological findings are compatible with the extensional viscosity analysis. According to the results from compressive tests, all HNT-based mPBT foams exhibited typical stretch-dominated deformation curves like BTA-based mPBT foams. As expected, elastic moduli of the foam samples increased with foam density.

Nevertheless, mPBT with 0.02 wt% HNT showed a slight increase in modulus compared to the one of the neat mPBT having almost the same foam density. This increase was assigned to more improved foam morphology and better cell orientation through the compression direction. Besides, 0.02 wt% HNT concentration gave rise in compressive strength (26 %) compared to the neat mPBT at the same foam density, which is very profitable for foaming applications. This improvement was also associated with better foam morphology, including a higher ratio of the strut thickness to strut length and better-oriented cells through the compression direction compared to the one of the neat mPBT. It was also assumed that HNTs embedded in the cell walls and struts might act as stress transfer points providing larger buckling resistance and thus further reinforcement in compressive strength of mPBT foam with 0.02 wt% HNT.

Finally, the multiple mixtures of nanaoadditives including (1) 0.08 wt% BTA1+0.02 wt% BTA2, (2) 0.02 wt% HNT+0.08 wt% BTA1, (3) 0.02 wt% HNT+0.02 wt% BTA2 and (4) 0.08 wt% BTA1+0.02 wt% BTA2+0.0.02 wt% HNT were used to understand if different nanoadditive combinations in mPBT foams have synergistic effects on foam morphology and compressive properties. Morphological findings showed that among all combinations, HNT+BTA2 nanoadditive mixture in mPBT features the finest foam morphology (cell size of 235 ± 59 μm, cell density of 1.9×10^6 cells/cm^3) and smallest achieved foam density of 75 kg/m^3 in literature and this study. This improvement in foam morphology compared to the neat mPBT foam and mPBT foam with only one type of nanoadditive was attributed to the synergistic effects induced by using multiple nanoadditives in mPBT foams. Looking at the compressive properties of the mPBT foams with multiple nanoadditive mixtures, the combination of BTA1 and BTA2 led to the highest achieved compressive modulus (21 ± 2 MPa) of this thesis. This was associated with the better foam morphology induced by synergistic effects of mixing two BTAs compared to the mPBT with only BTA2. Compressive strength results also exhibited that the same combination of BTAs leads to a significant increase in compressive strength compared to the mPBT foam only with BTA1 and BTA2 at the same

foam density. Nevertheless, the highest compressive strength (626 $\pm$ 15 kPa) was obtained with the mixture of all three nanaoadditives at a relatively higher foam density of 98 kg/m^3.

7 Zusammenfassung

Ziel dieser Arbeit war es, mPBT-Schäume mit niedriger Schaumdichte (< 100 kg/m³) und verbesserter Schaummorphologie mit einer mittleren Zellgröße von weniger als 500 µm in einem Tandem-Schaumextrusionsverfahren zu untersuchen. Diese Ziele wurden durch den Einsatz von organisch löslichen (BTAs) und anorganisch unlöslichen (HNTs) Nanoadditiven als Nukleierungsmittel für Polymerkristalle und Schaumzellen erreicht. Daneben war die Verbesserung der Druckeigenschaften bei niedrigen Schaumdichten mit Hilfe von Nanoadditiven in verschiedenen Konzentrationen ein weiteres Ziel, das für zahlreiche Schaumanwendungen entscheidend ist. Der wissenschaftliche Schwerpunkt dieser Arbeit lag auf der Erstellung von Struktur-Eigenschafts-Beziehungen von mPBT-Schaumsträngen, die in Bezug auf Schmelzfestigkeit, Schäumbarkeit und Kristallisationskinetik von mPBT-basierten Materialien durch BTAs und HNTs beeinflusst werden.

Zunächst wurde auf der Grundlage einer rheologischen Charakterisierung der optimale PBT-Typ aus dreien ausgewählt, um diese Ziele zu erreichen. Die Ergebnisse zeigten, dass Ultradur B6550 die höchste Viskosität bei der niedrigsten Frequenz aufweist, was bei der Verarbeitung von Vorteil sein könnte, um stabilere Schaumzellen zu erzielen. Dieses Verhalten ist auf das sehr hohe Molekulargewicht und der daraus resultierenden Schmelzfestigkeit zurückzuführen. Die Vorversuche und die Literatur zeigten jedoch, dass aufgrund der sehr schlechten rheologischen Eigenschaften eine Nachmodifizierung von PBT mit CE unumgänglich ist, um eine einfachere und stabilere Schäumbarkeit, eine bessere Schaummorphologie und -eigenschaften zu erreichen. Nach Anwendung verschiedener CE-Konzentrationen für die langkettige Verzweigung von PBT, wurden 0,6 Gew.-% als optimale CE-Konzentration ausgewählt, welche die einfachste und stabilste Schäumbarkeit, die niedrigste Schaumdichte und eine feine und gleichmäßige Schaummorphologie aufweist. Die Ergebnisse der Studie zur Optimierung der Prozessparameter zeigten, dass die optimale Schmelzetemperatur am Austritt der Düse und die Düsentemperatur, die die geringste Schaumdichte ergibt, bei 226 °C bzw. 235 °C liegen.

Darüber hinaus wurde der Einfluss von organisch löslichen Nanoadditiven, darunter kommerziell erhältliches BTA1 und maßgeschneidertes BTA2, auf das

Kristallisationsverhalten und die rheologischen Eigenschaften des mPBT untersucht. Die Berechnung der Kristallisations-Aktivierungsenergien (nach dem makrokinetischen Modell von Kissinger) des mPBT mit 0,08 Gew.-% BTA1 und 0,02 Gew.-% BTA2 ergab, dass BTA1 zu einer Verringerung der Aktivierungsenergie um etwa 40 % führte, während BTA2 einen vergleichbaren Wert zum reinen mPBT aufwies. Daraus wurde gefolgert, dass BTA1-Nanofasern als Keimbildner für mPBT-Kristalle fungieren könnten, während BTA2-Nanofasern keine mPBT-Keimbildung bewirken. Die Ergebnisse der komplexen Viskosität von mPBT mit 0,02, 0,04, 0,08, 0,1 und 0,25 Gew.-% BTA1 und BTA2 zeigen, dass die Verwendung von BTAs zu einer Verringerung der Viskosität bei den niedrigsten Frequenzen im Vergleich zu der des reinen mPBT führt, wobei der Unterschied bei höheren Frequenzen geringer wird. Eine zu hohe BTA-Konzentration ($\geq$ 0,25 Gew.-%) führte jedoch zu einer wesentlich stärkeren Abnahme der komplexen Viskosität bei niedrigen und hohen Frequenzen. Dies wurde der begrenzten Löslichkeit von BTAs bei hohen Konzentrationen zugeschrieben, die ungelöste Aggregate in der mPBT-Schmelze ausbilden. Es wurde angenommen, dass diese Aggregate mit den verzweigten Ketten interferieren und als Weichmacher wirken könnten, was zu niedrigeren Viskositätswerten führt.

Um die richtigen BTA1- und BTA2-Konzentrationen für eine optimale Schmelzefestigkeit und damit beste Schäumbarkeit zu erhalten, wurden die S-Koeffizienten aller Polymere nach der Trouton-Beziehung auf der Grundlage der instationären Dehnviskosität (aus Dehnviskositätsmessungen) und der instationären Scherviskosität (aus Anfahr-Scherversuchen) berechnet. Es wurde festgestellt, dass mit 0,08 Gew.-% BTA1 und 0,02 Gew.-% BTA2 ein maximaler Anstieg der S-Koeffizienten von 32 % bzw. 64 % erreicht wurde. Die verbesserte Schmelzefestigkeit wurde mit der Ausbildung eines Perkolationsnetzwerks der BTA-Nanofasern bei ihren optimalen Konzentrationen assoziiert. Darüber hinaus wurde der Einfluss von BTA-Typ und -Konzentration auf Morphologie, Dichte, Offenzelligkeit, Kristallinitätsgrad und Druckeigenschaften der mPBT-Schäume bestimmt. Die µ-CT-Bilder der Schaumproben zeigten, dass 0,08 Gew.-% BTA1 Schäume mit einer um 7 % verringerten mittleren Zellgröße und einer deutlich homogeneren Schaummorphologie aufweist, während mit 0,02 Gew.-% BTA2 die kleinste Zellgröße von 707 ± 197 µm erreicht wird. Dies wurde damit in Verbindung gebracht, dass BTAs als Keimbildner für mPBT-Schaumzellen wirken, indem sie die Anzahl der Keimbildungsstellen erhöhen und die Aktivierungsenergiebarriere für die Zellkeimbildung senken. Die Ergebnisse der Morphologie stimmten mit den Werten des S-

Koeffizienten überein, die zeigen, dass je höher der Koeffizient, desto höher die Schmelzfestigkeit, desto besser die Stabilisierung der Schaumzellen und somit eine bessere Schaummorphologie vorliegt. Darüber hinaus lag der Kristallinitätsgrad aller Schaumproben im gleichen Bereich, was zeigt, dass die Kristallinität während des Schaumextrusionsprozesses hauptsächlich durch die hohen dehnungsinduzierten Kräfte bestimmt wird. Bei diesen Konzentrationen gibt es keine nennenswerten Auswirkungen von BTAs. Den Druckversuchen zufolge folgten die charakteristischen Spannungs-Dehnungs-Diagramme aller Schaumstoffproben dem typischen dehnungsdominierten Verformungsverhalten (Richtung: außerhalb der Ebene). Der Druckmodul der Schaumstoffproben hing hauptsächlich von der Schaumstoffdichte ab und wurde nicht durch BTAs beeinflusst, da die Modulwerte von BTAs und der Polymermatrix im gleichen Bereich lagen. Betrachtet man die Druckfestigkeitswerte der Schaumstoffe, so wurde bei gleicher Schaumdichte mit 0,08 Gew.-% BTA1 ein Anstieg um 25 % erzielt, während 0,02 Gew.-% BTA2 zu einem Anstieg um 35 % bei einer um etwa 15 % höheren Schaumdichte im Vergleich zu der des reinen mPBT führte. Die Verbesserung der Druckfestigkeit mit BTA1 wurde der feineren und gleichmäßigeren Schaummorphologie sowie dem intrinsischen Verstärkungseffekt der BTA1-Fasern zugeschrieben, die in den Zellwänden und Verstrebungen eingebettet sind und den Schaum knickfester machen. Im Fall von BTA2 waren eine verbesserte Schaummorphologie, eine höhere Zelldichte und damit Schaumdichte, eine geringere Offenzelligkeit sowie der intrinsische Verstärkungseffekt der BTA2-Fasern für die höhere Druckfestigkeit verantwortlich. Zusammenfassend lässt sich sagen, dass ein mPBT-Schaum mit 0,08 Gew.-% BTA1 (handelsübliches Nanoadditiv) das optimale Material darstellt, welches die beste mechanische Leistung bei der geringsten Schaumdichte aufweist und damit für zahlreiche Schaumstoffanwendungen entscheidende Vorteile bietet.

Neben den organischen löslichen Nanoadditiven wurde auch der Einfluss des anorganischen, unlöslichen Nanoadditivs HNT auf das Kristallisationsverhalten und die rheologischen Eigenschaften des mPBT untersucht. Die 38%ige Verringerung der Kristallisations-Aktivierungsenergie des mPBT mit 0,02 Gew.-% HNT zeigte im Vergleich zum reinen mPBT, dass HNTs auch als Keimbildner für Polymerkristalle, analog zu BTA1 wirken können. Betrachtet man die Nullviskosität von mPBT mit 0,02, 0,04, 0,08, 0,1 und 0,25 Gew.-% HNT, so kommt man zu dem Schluss, dass HNTs bei allen Konzentrationen zu einer spürbaren Abnahme der Viskosität bei den niedrigsten Frequenzen im Vergleich zu der des reinen mPBT führen. Dies wurde auf die Vergrößerung des freien Volumens und die Verringerung der

intramolekularen Reibung aufgrund der Interferenz der HNTs mit den weit verzweigten mPBT-Ketten zurückgeführt. Dieser Viskositätsunterschied verringerte sich jedoch bei höheren Frequenzen, die in der Nähe der beim Schäumungsprozess auftretenden Frequenzen liegen. Somit konnte bewiesen werden, dass HNTs in diesen niedrigen Konzentrationen die Scherviskosität der Schmelze nicht erhöhen und die Verarbeitbarkeit nicht beeinträchtigen. Dieses Verhalten widerlegt in diesen Fall die allgemeine Annahme, dass sich die Verwendung unlöslicher anorganischer nachteilig auf die Verarbeitbarkeit von Polymerschmelzen auswirken.

Darüber hinaus ergab sich der größte S-Koeffizient bei 0,02 Gew.-% HNT in mPBT, was zu der höchsten Schmelzfestigkeit und der feinsten und gleichmäßigsten Schaummorphologie mit einer mittleren Zellgröße von 330 ± 83 μm führte (entspricht der halben Zellgröße von mPBT mit 0,08 Gew.-% BTA1 bei gleicher Schaumdichte). Die verbesserte Schaummorphologie wurde der erfolgreichen Rolle von HNT als Nukleierungsmittel für mPBT-Schaumzellen zugeschrieben, was zu einer Erhöhung der Anzahl der Nukleierungsstellen und einer Verringerung der Energiebarriere für die Schaumzellkristallisation führte. Eine weitere Erhöhung der HNT-Konzentration konnte weder die Schmelzfestigkeit noch die Schaummorphologie verbessern. Es wurde festgestellt, dass die morphologischen Ergebnisse mit der Analyse der Dehnviskosität vereinbar sind. Nach den Ergebnissen der Drucktests zeigten alle HNT-basierten mPBT-Schäume typische streckungsdominierte Verformungskurven, analog zu BTA-basierte mPBT-Schäume. Wie erwartet, stiegen die Elastizitätsmoduln der Schaumproben mit der Schaumdichte.

Dennoch zeigte mPBT mit 0,02 Gew.-% HNT einen leichten Anstieg des Moduls im Vergleich zum reinen mPBT mit fast derselben Schaumdichte. Dieser Anstieg wurde einer verbesserten Schaummorphologie und einer besseren Zellorientierung in Kompressionsrichtung zugeschrieben. Außerdem führte eine HNT-Konzentration von 0,02 Gew.-% zu einem Anstieg der Druckfestigkeit (26 %) im Vergleich zum reinen mPBT bei gleicher Schaumdichte, was für Schaumanwendungen sehr von Vorteil ist. Diese Verbesserung wurde auch mit einer besseren Schaummorphologie in Verbindung gebracht, einschließlich eines höheren Verhältnisses von Strebendicke zu Strebenlänge und besser ausgerichteten Zellen in Kompressionsrichtung im Vergleich zum reinen mPBT. Es wurde auch angenommen, dass die in den Zellwänden und Verstrebungen eingebetteten HNTs als Spannungsübertragungspunkte fungieren können, die

eine größere Knickbeständigkeit und somit eine weitere Verstärkung der Druckfestigkeit des mPBT-Schaums mit 0,02 Gew.-% HNT bewirken.

Schließlich wurden die Mehrfachmischungen von Nanoadditiven einschließlich (1) 0,08 Gew.-% BTA1+0,02 Gew.-% BTA2, (2) 0,02 Gew.-% HNT+0,08 Gew.-% BTA1, (3) 0,02 Gew.-% HNT+0,02 Gew.-% BTA2 und (4) 0,08 Gew.-% BTA1+0.02 Gew.-% BTA2+0,02 Gew.-% HNT verwendet, um herauszufinden, ob verschiedene Kombinationen von Nanoadditiven in mPBT-Schäumen synergistische Effekte auf die Schaummorphologie und die Druckeigenschaften haben. Die morphologischen Ergebnisse zeigten, dass von allen Kombinationen die HNT+BTA2-Nanoadditivmischung in mPBT die feinste Schaummorphologie (Zellgröße von 235 ± 59 µm, Zelldichte von $1,9 \times 106$ Zellen/cm^3) und die kleinste in der Literatur und in dieser Studie erreichte Schaumdichte von 75 kg/m^3 aufweist. Diese Verbesserung der Schaummorphologie im Vergleich zum reinen mPBT-Schaum und zum mPBT-Schaum mit nur einer Art von Nanoadditiv wurde auf die synergistischen Effekte zurückgeführt, die durch die Verwendung mehrerer Nanoadditive in mPBT-Schäumen entstehen. Betrachtet man die Druckeigenschaften der mPBT-Schäume mit mehreren Nanoadditivmischungen, so führte die Kombination von BTA1 und BTA2 zu dem höchsten erreichten Druckmodul (21 ± 2 MPa) dieser Arbeit. Dies wurde mit der verbesserten Schaummorphologie in Verbindung gebracht, die durch die synergistischen Effekte der Mischung von zwei BTAs im Vergleich zum mPBT mit nur BTA2 hervorgerufen wurde. Die Ergebnisse der Druckfestigkeit zeigten auch, dass die gleiche Kombination von BTAs zu einer signifikanten Erhöhung der Druckfestigkeit im Vergleich zum mPBT-Schaum nur mit BTA1 und BTA2 bei gleicher Schaumdichte führt. Die höchste Druckfestigkeit (626 ± 15 kPa) wurde jedoch mit der Mischung aus allen drei Nanoadditiven bei einer höheren Schaumdichte von 98 kg/m^3 erzielt.

8 Outlook

In polymer foams, density and cell size reduction are essential to achieve improved thermal insulation properties for various applications such as insulation in the engine compartment, fish or seafood packaging or construction applications. 10 % better insulation in a building could have a significant impact on global energy consumption and contributes to the protection of the environment by reducing the carbon dioxide (CO_2) emissions during heating and cooling [197]. Reduction in cell size leads to decreased thermal conductivity through the solid phase due to the tortuosity of the cellular structure [198]. In addition to improved insulation properties, high mechanical performance (under shear and bending as well as compression) is a demand for applications such as aircraft, wind energy systems, automobiles and construction [29,33–35]. To address this, the nanoadditives of BTA1, BTA2 and HNT were used and set goals were achieved with quite promising morphological and mechanical findings. Nevertheless, for the sake of achieving lightweight mPBT foams with more enhanced properties, the following is recommended for future works:

- Use of BTAs having different chemical structures resulting in better solubility and self-assembly behavior in mPBT and thus nano-objects with larger aspect ratio to reduce the cell size of the foams further at the same foam density.
- Selecting various HNT types having different aspect ratios as well as surface modification for obtaining a better quality of dispersion in mPBT even at higher nanoadditive concentrations. By doing so, achieving much finer cell morphology and further reinforcement in compressive properties at low foam densities might be possible.

Furthermore, to be able to apply additional characterization tests to determine insulation, shear and bending properties of the foam samples as well as to increase precision in compression analysis, the following is recommended for future works:

Applying technical-scale foam extrusion (scale-up) with higher barrel pressure providing mPBT melt with higher expandability at the slit die, which is more common and suitable for producing commercial extruded foams. By doing so, it would be possible to manufacture foam samples with higher diameter and larger geometries that can be prepared according to the standards for various characterization.

9 Bibliography

1. Gibson, L.J.; Ashby, M.F. *Cellular Solids*; 2nd ed.; Cambridge University Press, 1997; ISBN 9780521499118.

2. Köppl, T.; Raps, D.; Altstädt, V. E-PBT—Bead foaming of poly(butylene terephthalate) by underwater pelletizing. *J. Cell. Plast.* 2014, *50*, 475–487.

3. Jeong, B.J.; Xanthos, M. Reactive modification of PBT with applications in low density extrusion foaming. *Polym. Eng. Sci.* 2007, *47*, 244–253.

4. Köppl, T. Halogen-free flame-retarded polybutylene terephthalate and its processing into polymer foams. [Dissertation], University of Bayreuth, 2014.

5. Phobos, N. Process for the continuous production of high molecular weight polyester resin, EP0422282B1, 1989.

6. Sugimoto, M.; Tanaka, T.; Masubuchi, Y.; Takimoto, J.-I.; Koyama, K. Effect of chain structure on the melt rheology of modified polypropylene. *J. Appl. Polym. Sci.* 1999, *73*, 1493–1500.

7. Gotsis, A.D.; Zeevenhoven, B.L.F.; Tsenoglou, C. Effect of long branches on the rheology of polypropylene. *J. Rheol.* 2004, *48*, 895–914.

8. Guo, B.; Chan, C.-M. Chain extension of poly(butylene terephthalate) by reactive extrusion. *J. Appl. Polym. Sci.* 1999, *71*, 1827–1834.

9. Bikiaris, D.; Karayannidis, G. Synthesis and characterisation of branched and partially crosslinked poly(ethylene terephthalate). *Polym. Int.* 2003, *52*, 1230–1239.

10. Bikiaris, D.N.; Karayannidis, G.P. Chain extension of polyesters PET and PBT with two new diimidodiepoxides. II. *J. Polym. Sci. Part A Polym. Chem.* 1996, *34*, 1337–1342.

11. Bikiaris, D.N.; Karayannidis, G.P. Chain extension of polyesters PET and PBT with N,N′-bis (glycidyl ester) pyromellitimides. I. *J. Polym. Sci. Part A Polym. Chem.* 1995, *33*, 1705–1714.

12. Romani, F.; Corrieri, R.; Braga, V.; Ciardelli, F. Monitoring the chemical crosslinking of propylene polymers through rheology. *Polymer.* 2002, *43*, 1115–1131.

13. Tian, J.; Yu, W.; Zhou, C. The preparation and rheology characterization of long chain branching polypropylene. *Polymer.* 2006, *47*, 7962–7969.

14. Zhai, W.; Wang, H.; Yu, J.; Dong, J.-Y.; He, J. Foaming behavior of isotactic polypropylene in supercritical CO_2 influenced by phase morphology via chain grafting. *Polymer.* 2008, *49*, 3146–3156.

15. Standau, T.; Hädelt, B.; Schreier, P.; Altstädt, V. Development of a bead foam from an engineering polymer with addition of chain extender: Expanded polybutylene terephthalate. *Ind. Eng. Chem. Res.* 2018, *57*, 17170–17176.

16. Bimestre, B.H.; Saron, C. Chain extension of poly (ethylene terephthalate) by reactive extrusion with secondary stabilizer. *Mater. Res.* 2012, *15*, 467–472.

17. Raffa, P.; Coltelli, M.-B.; Savi, S.; Bianchi, S.; Castelvetro, V. Chain extension and

branching of poly(ethylene terephthalate) (PET) with di- and multifunctional epoxy or isocyanate additives: An experimental and modelling study. *React. Funct. Polym.* 2012, *72*, 50–60.

18. Jeong, B.; Xanthos, M.; Seo, Y. Extrusion foaming behavior of PBT Resins. *J. Cell. Plast.* 2006, *42*, 165–176.

19. Song, K.; Li, W.; Eckert, J.O.; Wu, D.; Apfel, R.E. Generation of novel microstructures in rapidly foamed polybutylene terephthalate. *J. Mater. Sci.* 1999, *34*, 5387–5395.

20. Antunes, M.; Gedler, G.; Velasco, J.I. Multifunctional nanocomposite foams based on polypropylene with carbon nanofillers. *J. Cell. Plast.* 2013, *49*, 259–279.

21. Zhao, J.; Zhao, Q.; Wang, L.; Wang, C.; Guo, B.; Park, C.B.; Wang, G. Development of high thermal insulation and compressive strength BPP foams using mold-opening foam injection molding with in-situ fibrillated PTFE fibers. *Eur. Polym. J.* 2018, *98*, 1–10.

22. Rizvi, A.; Park, C.B.; Favis, B.D. Tuning viscoelastic and crystallization properties of polypropylene containing in-situ generated high aspect ratio polyethylene terephthalate fibrils. *Polymer.* 2015, *68*, 83–91.

23. Kakroodi, A.R.; Kazemi, Y.; Ding, W.D.; Ameli, A.; Park, C.B. Poly(lactic acid)-based in situ microfibrillar Ccmposites with enhanced crystallization kinetics, mechanical properties, rheological behavior, and foaming ability. *Biomacromolecules* 2015, *16*, 3925–3935.

24. Rizvi, A.; Park, C.B. Dispersed polypropylene fibrils improve the foaming ability of a polyethylene matrix. *Polymer.* 2014, *55*, 4199–4205.

25. Huang, H.-X.; Wang, J.-K. Improving polypropylene microcellular foaming through blending and the addition of nano-calcium carbonate. *J. Appl. Polym. Sci.* 2007, *106*, 505–513.

26. Mörl, M.; Steinlein, C.; Kreger, K.; Schmidt, H.-W.; Altstädt, V. Improved compression properties of polypropylene extrusion foams by supramolecular additives. *J. Cell. Plast.* 2018, *54*, 483–498.

27. Wang, C.; Ying, S.; Xiao, Z. Preparation of short carbon fiber/polypropylene fine-celled foams in supercritical CO_2. *J. Cell. Plast.* 2013, *49*, 65–82.

28. Jiang, X.-L.; Bao, J.-B.; Liu, T.; Zhao, L.; Xu, Z.-M.; Yuan, W.-K. Microcellular foaming of oolypropylene/clay nanocomposites with supercritical carbon dioxide. *J. Cell. Plast.* 2009, *45*, 515–538.

29. Wu, W.; Cao, X.; Zhang, Y.; He, G. Polylactide/halloysite nanotube nanocomposites: Thermal, mechanical properties, and foam processing. *J. Appl. Polym. Sci.* 2013, *130*, 443–452.

30. Lee, S.H.; Zhang, Y.; Kontopoulou, M.; Park, C.B.; Wong, A.; Zhai, W. Optimization of dispersion of nanosilica particles in a PP matrix and their effect on foaming. *Int. Polym. Process.* 2011, *26*, 388–398.

31. Hwang, S.; Hsu, P.P. Effects of silica particle size on the structure and properties of polypropylene/silica composites foams. *J. Ind. Eng. Chem.* 2013, *19*, 1377–1383.

32. Richter, F.; Schmidt, H.-W. Supramolecular nucleating agents for poly(butylene terephthalate) based on 1,3,5-benzenetrisamides. *Macromol. Mater. Eng.* 2013, *298*, 190–200.

33. Eryildiz, M.; Altan, M. Polylactide/halloysite nanocomposite foams: Particle dispersion and mechanical strength. *Acta Phys. Pol. A* 2019, *135*, 619–621.

34. Demori, R.; Bischoff, E.; de Azeredo, A.P.; Liberman, S.A.; Maia, J.; Mauler, R.S. Morphological, thermo-mechanical, and thermal conductivity properties of halloysite nanotube-filled polypropylene nanocomposite foam. *J. Cell. Plast.* 2018, *54*, 217–233.

35. Wu, W.; Cao, X.; Lin, H.; He, G.; Wang, M. Preparation of biodegradable poly(butylene succinate)/halloysite nanotube nanocomposite foams using supercritical CO_2 as blowing agent. *J. Polym. Res.* 2015, *22*.

36. Frisch, K.C.; Klempner, D. *Handbook of Polymeric Foams and Foam Technology*; Hanser Verlag: München, 1991; ISBN 3-446-15097-8.

37. Okolieocha, C.; Raps, D.; Subramaniam, K.; Altstädt, V. Microcellular to nanocellular polymer foams: Progress (2004-2015) and future directions - A review. *Eur. Polym. J.* 2015, *73*, 500–519.

38. Baur, E.; Osswald, T.A.; Rudolph, N.; Brinkmann, S.; Schmachtenberg, E. *Saechtling Kunststoff Taschenbuch*; Baur, E., Osswald, T.A., Rudolph, N., Brinkmann, S., Schmachtenberg, E., Eds.; 31st ed.; Hanser Verlag: München, 2013; ISBN 978-3-446-43442-4.

39. *Foam Extrusion: Principles and Practice*; Lee, S.-T., Park, C.B., Eds.; 2nd ed.; CRC Press, 2014; ISBN 9781439898598.

40. Tomasko, D.L.; Burley, A.; Feng, L.; Yeh, S.-K.; Miyazono, K.; Nirmal-Kumar, S.; Kusaka, I.; Koelling, K. Development of CO_2 for polymer foam applications. *J. Supercrit. Fluids* 2009, *47*, 493–499.

41. Molina, M.J.; Rowland, F.S. Stratospheric sink for chlorofluoromethanes: chlorine atom-catalysed destruction of ozone. *Nature* 1974, *249*, 810–812.

42. Jacobs, L.J.M.; Kemmere, M.F.; Keurentjes, J.T.F. Sustainable polymer foaming using high pressure carbon dioxide: a review on fundamentals, processes and applications. *Green Chem.* 2008, *10*, 731.

43. Becker, G.; Braun, D. *Kunststoff Handbuch- Band 4 Polystyrol*; Gausepohl, H., Gellert, R., Eds.; Hanser Verlag: München, 1996; ISBN 3446180044.

44. Goel, S.K.; Beckman, E.J. Nucleation and growth in microcellular materials: Supercritical CO_2 as foaming agent. *AIChE J.* 1995, *41*, 357–367.

45. Ruiz, J.A.R.; Marc-Tallon, J.; Pedros, M.; Dumon, M. Two-step micro cellular foaming of amorphous polymers in supercritical CO_2. *J. Supercrit. Fluids* 2011, *57*, 87–94.

46. McHugh, M.A.; Krukonis, V.J. *Supercritical Fluid Extraction*; 2nd ed.; Elsevier: Stoneheim, 1994; ISBN 9780080518176.

47. Ding, J.; Ma, W.; Song, F.; Zhong, Q. Foaming of polypropylene with supercritical carbon dioxide: An experimental and theoretical study on a new process. *J. Appl. Polym.*

Sci. 2013, *130*, 2877–2885.

48. Xu, Z.-M.; Jiang, X.-L.; Liu, T.; Hu, G.-H.; Zhao, L.; Zhu, Z.-N.; Yuan, W.-K. Foaming of polypropylene with supercritical carbon dioxide. *J. Supercrit. Fluids* 2007, *41*, 299–310.

49. Sauceau, M.; Fages, J.; Common, A.; Nikitine, C.; Rodier, E. New challenges in polymer foaming: A review of extrusion processes assisted by supercritical carbon dioxide. *Prog. Polym. Sci.* 2011, *36*, 749–766.

50. Garcia-Leiner, M.; Lesser, A.J. CO_2-assisted polymer processing: A new alternative for intractable polymers. *J. Appl. Polym. Sci.* 2004, *93*, 1501–1511.

51. Ruiz, J.A.R.; Cloutet, E.; Dumon, M. Investigation of the nanocellular foaming of polystyrene in supercritical CO_2 by adding a CO_2-philic perfluorinated block copolymer. *J. Appl. Polym. Sci.* 2012, *126*, 38–45.

52. Fleming, O.S.; Kazarian, S.G. Polymer Processing with Supercritical Fluids. In *Supercritical Carbon Dioxide*; Wiley-VCH Verlag GmbH & Co. KGaA: Weinheim, FRG, 2006; pp. 205–238.

53. Kamiya, Y.; Mizoguchi, K.; Terada, K.; Fujiwara, Y.; Wang, J.-S. CO_2 Sorption and Dilation of Poly(methyl methacrylate). *Macromolecules* 1998, *31*, 472–478.

54. Kamiya, Y.; Mizoguchi, K.; Naito, Y.; Hirose, T. Gas sorption in poly(vinyl benzoate). *J. Polym. Sci. Part B Polym. Phys.* 1986, *24*, 535–547.

55. Wong, B.; Zhang, Z.; Handa, Y.P. High-precision gravimetric technique for determining the solubility and diffusivity of gases in polymers. *J. Polym. Sci. Part B Polym. Phys.* 1998, *36*, 2025–2032.

56. Lee, J.G.; Flumerfelt, R.W. Nitrogen solubilities in low-density polyethylene at high temperatures and high pressures. *J. Appl. Polym. Sci.* 1995, *58*, 2213–2219.

57. Sato, Y.; Fujiwara, K.; Takikawa, T.; Sumarno; Takishima, S.; Masuoka, H. Solubilities and diffusion coefficients of carbon dioxide and nitrogen in polypropylene, high-density polyethylene, and polystyrene under high pressures and temperatures. *Fluid Phase Equilib.* 1999, *162*, 261–276.

58. Areerat, S.; Hayata, Y.; Katsumoto, R.; Kegasawa, T.; Egami, H.; Ohshima, M. Solubility of carbon dioxide in polyethylene/titanium dioxide composite under high pressure and temperature. *J. Appl. Polym. Sci.* 2002, *86*, 282–288.

59. Sato, Y.; Takikawa, T.; Takishima, S.; Masuoka, H. Solubilities and diffusion coefficients of carbon dioxide in poly(vinyl acetate) and polystyrene. *J. Supercrit. Fluids* 2001, *19*, 187–198.

60. Aubert, J.H. Solubility of carbon dioxide in polymers by the quartz crystal microbalance technique. *J. Supercrit. Fluids* 1998, *11*, 163–172.

61. Li, G.; Li, H.; Wang, J.; Park, C.B. Investigating the solubility of CO_2 in polypropylene using various EOS Models. *Cell. Polym.* 2006, *25*, 237–248.

62. Paul, D.R. Gas sorption and transport in glassy polymers. *Berichte der Bunsengesellschaft für Phys. Chemie* 1979, *83*, 294–302.

63. Klopffer, M.H.; Flaconneche, B. Transport properties of gases in polymers: Bibliographic review. *Oil Gas Sci. Technol.* 2001, *56*, 223–244.

64. Gendron, R. *Thermoplastic Foam Processing: Principles and Development*; Gendron, R., Ed.; 1st ed.; CRC Press, 2004; ISBN 9780367393700.

65. Ramesh, N.S. Fundamentals of Bubble Nucleation and Growth in Polymers. In *Polymeric Foams: Mechanisms and Materials*; Lee, S.T., Ramesh, N.S., Eds.; CRC Press: Florida, 2004.

66. Fisher, M.E. The theory of condensation and the critical point. In *Excursions in the Land of Statistical Physics*; World Scientific, 2016; pp. 25–58.

67. Lothe, J.; Pound, G.M. Reconsiderations of nucleation theory. *J. Chem. Phys.* 1962, *36*, 2080–2085.

68. Dillmann, A.; Meier, G.E.A. A refined droplet approach to the problem of homogeneous nucleation from the vapor phase. *J. Chem. Phys.* 1991, *94*, 3872–3884.

69. Bowers, P.G.; Bar-Eli, K.; Noyes, R.M. Unstable supersaturated solutions of gases in liquids and nucleation theory. *J. Chem. Soc. Faraday Trans.* 1996, *92*, 2843.

70. Girshick, S.L.; Chiu, C. Kinetic nucleation theory: A new expression for the rate of homogeneous nucleation from an ideal supersaturated vapor. *J. Chem. Phys.* 1990, *93*, 1273–1277.

71. Cahn, J.W.; Hilliard, J.E. Free energy of a nonuniform system. III. Nucleation in a two-component incompressible fluid. *J. Chem. Phys.* 1959, *31*, 688–699.

72. Kim, K.Y.; Kang, S.L.; Kwak, H.-Y. Bubble nucleation and growth in polymer solutions. *Polym. Eng. Sci.* 2004, *44*, 1890–1899.

73. Farkas, L. Keimbildungsgeschwindigkeit in übersättigten Dämpfen. *Zeitschrift für Phys. Chemie* 1927, *125U*.

74. Volmer, M.; Weber, A. Keimbildung in übersättigten Gebilden. *Zeitschrift für Phys. Chemie* 1926, *119U*.

75. Oxtoby, D.W. Density functional methods in the statistical mechanics of materials. *Annu. Rev. Mater. Res.* 2002, *32*, 39–52.

76. Kumar, V. Process synthesis for manufacturing microcellular thermoplastic parts : a case study in axiomatic design. [Dissertation], Massachusetts Institute of Technology., 1988.

77. Shafi, M.A.; Lee, J.G.; Flumerfelt, R.W. Prediction of cellular structure in free expansion polymer foam processing. *Polym. Eng. Sci.* 1996, *36*, 1950–1959.

78. Han, J.H.; Dae Han, C. Bubble nucleation in polymeric liquids. II. theoretical considerations. *J. Polym. Sci. Part B Polym. Phys.* 1990, *28*, 743–761.

79. Leung, S.N.; Park, C.B.; Xu, D.; Li, H.; Fenton, R.G. Computer simulation of bubble-growth phenomena in foaming. *Ind. Eng. Chem. Res.* 2006, *45*, 7823–7831.

80. Leung, S.N.; Park, C.B.; Li, H. Effects of nucleating agents' shapes and interfacial properties on cell nucleation. *J. Cell. Plast.* 2010, *46*, 441–460.

81. Shimoda, M.; Tsujimura, I.; Tanigaki, M.; Ohshima, M. Polymeric foaming simulation for extrusion processes. *J. Cell. Plast.* 2001, *37*, 517–536.

82. Jung, P.U. Development of innovative gas-assisted foam injection molding technology. [Dissertation], University of Toronto, 2013.

83. Lee, S.-T. Shear effects on thermoplastic foam nucleation. *Polym. Eng. Sci.* 1993, *33*, 418–422.

84. Ward, C.A.; Levart, E. Conditions for stability of bubble nuclei in solid surfaces contacting a liquid-gas solution. *J. Appl. Phys.* 1984, *56*, 491–500.

85. Blander, M.; Katz, J.L. Bubble nucleation in liquids. *AIChE J.* 1975, *21*, 833–848.

86. Shutov, F.A. Foamed polymers. cellular structure and properties. In *Industrial Developments*; Springer-Verlag: Berlin/Heidelberg, 1983; pp. 155–218.

87. Mills, N.J. Handbook of polymeric foams and foam technology. *Polymer.* 1993, *34*, 2237.

88. Chen, L.; Rende, D.; Schadler, L.S.; Ozisik, R. Polymer nanocomposite foams. *J. Mater. Chem. A* 2013, *1*, 3837.

89. Kim, S., Han, S.H., Lee, Y.M. Thermally rearranged (TR) polybenzoxazole hollow fiber membranes for CO_2 capture. *J. Memb. Sci.* 2012, *403–404*, 169–178.

90. Lee, S.J.; Heo, D.N.; Moon, J.-H.; Park, H.N.; Ko, W.-K.; Bae, M.S.; Lee, J.B.; Park, S.W.; Kim, E.-C.; Lee, C.H.; Jung, B.-Y.; Kwon, I.K. Chitosan/Polyurethane blended fiber sheets containing silver sulfadiazine for use as an antimicrobial wound dressing. *J. Nanosci. Nanotechnol.* 2014, *14*, 7488–7494.

91. Imai, Y. Inorganic Nano-fillers for Polymers. In *Encyclopedia of Polymeric Nanomaterials*; Springer Berlin Heidelberg: Berlin, Heidelberg, 2014; pp. 1–7.

92. Tiwari, J.N.; Tiwari, R.N.; Kim, K.S. Zero-dimensional, one-dimensional, two-dimensional and three-dimensional nanostructured materials for advanced electrochemical energy devices. *Prog. Mater. Sci.* 2012, *57*, 724–803.

93. Rizvi, A.; Tabatabaei, A.; Barzegari, M.R.; Mahmood, S.H.; Park, C.B. In situ fibrillation of CO_2-philic polymers: Sustainable route to polymer foams in a continuous process. *Polymer.* 2013, *54*, 4645–4652.

94. Stumpf, M.; Spörrer, A.; Schmidt, H.-W.; Altstädt, V. Influence of supramolecular additives on foam morphology of injection-molded i-PP. *J. Cell. Plast.* 2011, *47*, 519–534.

95. Aksit, M.; Klose, B.; Zhao, C.; Kreger, K.; Schmidt, H.-W.; Altstädt, V. Morphology control of extruded polystyrene foams with benzene-trisamide-based nucleating agents. *J. Cell. Plast.* 2019, *55*, 249–261.

96. De Greef, T.F.A.; Meijer, E.W. Supramolecular polymers. *Nature* 2008, *453*, 171–173.

97. De Greef, T.F.A.; Smulders, M.M.J.; Wolffs, M.; Schenning, A.P.H.J.; Sijbesma, R.P.; Meijer, E.W. Supramolecular polymerization. *Chem. Rev.* 2009, *109*, 5687–5754.

98. Brunsveld, L.; Folmer, B.J.B.; Meijer, E.W.; Sijbesma, R.P. Supramolecular polymers.

Chem. Rev. 2001, *101*, 4071–4098.

99. Atwood, J.L.; Lehn, J.-M. *Comprehensive Supramolecular Chemistry: Supramolecular Technology*; Atwood, J.L., Lehn, J.-M., Eds.; 1st ed.; Pergamon Press: New York, 1996; ISBN 0080406106.

100. Mörl, M. Steigerung der Zähigkeit von isotaktischem Polypropylen durch Kontrolle der Morphologie mittels 1,3,5-Benzoltrisamiden. [Dissertation], University of Bayreuth, 2018.

101. Kersch, M.; Schmidt, H.-W.; Altstädt, V. Influence of different beta-nucleating agents on the morphology of isotactic polypropylene and their toughening effectiveness. *Polymer.* 2016, *98*, 320–326.

102. Kersch, M.; Pischke, L.; Schmidt, H.-W.; Altstädt, V. Influence of trisamide-based additives on the morphological and mechanical properties of isotactic polypropylene. *Polymer.* 2014, *55*, 3227–3233.

103. Blomenhofer, M.; Ganzleben, S.; Hanft, D.; Schmidt, H.-W.; Kristiansen, M.; Smith, P.; Stoll, K.; Mäder, D.; Hoffmann, K. "Designer" nucleating agents for polypropylene. *Macromolecules* 2005, *38*, 3688–3695.

104. Kristiansen, M.; Smith, P.; Chanzy, H.; Baerlocher, C.; Gramlich, V.; McCusker, L.; Weber, T.; Pattison, P.; Blomenhofer, M.; Schmidt, H.-W. Structural aspects of 1,3,5-Benzenetrisamides−A new family of nucleating agents. *Cryst. Growth Des.* 2009, *9*, 2556–2558.

105. Schmidt, M.; Wittmann, J.J.; Kress, R.; Schneider, D.; Steuernagel, S.; Schmidt, H.-W.; Senker, J. Crystal structure of a highly efficient clarifying agent for isotactic polypropylene. *Cryst. Growth Des.* 2012, *12*, 2543–2551.

106. Wegner, M.; Dudenko, D.; Sebastiani, D.; Palmans, A.R.A.; de Greef, T.F.A.; Graf, R.; Spiess, H.W. The impact of the amide connectivity on the assembly and dynamics of benzene-1,3,5-tricarboxamides in the solid state. *Chem. Sci.* 2011, *2*, 2040.

107. Mohmeyer, N.; Müller, B.; Behrendt, N.; Hillenbrand, J.; Klaiber, M.; Zhang, X.; Smith, P.; Altstädt, V.; Sessler, G.M.; Schmidt, H.-W. Nucleation of isotactic polypropylene by triphenylamine-based trisamide derivatives and their influence on charge-storage properties. *Polymer.* 2004, *45*, 6655–6663.

108. Standau, T.; Altstädt, V. Foams. In *Polypropylene Handbook: Morphology, Blends and Composites*; Karger-Kocsis, J., Bárány, T., Eds.; Springer International Publishing: Cham, 2019; pp. 579–641 ISBN 978-3-030-12903-3.

109. Zehe, C.S.; Hill, J.A.; Funnell, N.P.; Kreger, K.; van der Zwan, K.P.; Goodwin, A.L.; Schmidt, H.-W.; Senker, J. Mesoscale polarization by geometric frustration in columnar supramolecular crystals. *Angew. Chem. Int. Ed. Engl.* 2017, *56*, 4432–4437.

110. Gong, P.; Buahom, P.; Tran, M.-P.; Saniei, M.; Park, C.B.; Pötschke, P. Heat transfer in microcellular polystyrene/multi-walled carbon nanotube nanocomposite foams. *Carbon N. Y.* 2015, *93*, 819–829.

111. Zhang, C.; Zhu, B.; Lee, L.J. Extrusion foaming of polystyrene/carbon particles using carbon dioxide and water as co-blowing agents. *Polymer.* 2011, *52*, 1847–1855.

112. Min, Z.; Yang, H.; Chen, F.; Kuang, T. Scale-up production of lightweight high-strength polystyrene/carbonaceous filler composite foams with high-performance electromagnetic interference shielding. *Mater. Lett.* 2018, *230*, 157–160.

113. Okolieocha, C.; Köppl, T.; Kerling, S.; Tölle, F.J.; Fathi, A.; Mülhaupt, R.; Altstädt, V. Influence of graphene on the cell morphology and mechanical properties of extruded polystyrene foam. *J. Cell. Plast.* 2015, *51*, 413–426.

114. Kausar, A. Synthesis and properties of novel polystyrene/polyurea and functional graphene-based nanocomposite foams. *J. Cell. Plast.* 2017, *53*, 305–318.

115. Fu, D.; Kuang, T.; Yen, Y.-C.; Li, D.; Benatar, A.; Peng, X.; Lee, L.J. Polystyrene/ multi-wall carbon nanotube composite and its foam assisted by ultrasound vibration. *J. Cell. Plast.* 2017, *53*, 273–285.

116. Shen, J.; Han, X.; Lee, L.J. Nanoscaled Reinforcement of Polystyrene Foams using Carbon Nanofibers. *J. Cell. Plast.* 2006, *42*, 105–126.

117. Kumar, A.; Patham, B.; Mohanty, S.; Nayak, S.K. Polypropylene–nano-silica nanocomposite foams: mechanisms underlying foamability, and foam microstructure, crystallinity and mechanical properties. *Polym. Int.* 2020, *69*, 373–386.

118. Acuña, P.; Li, Z.; Santiago-Calvo, M.; Villafañe, F.; Rodríguez-Perez, M.; Wang, D.-Y. Influence of the characteristics of expandable graphite on the morphology, thermal properties, fire behaviour and compression performance of a rigid polyurethane foam. *Polymers.* 2019, *11*, 168.

119. Zhao, J.; Wang, G.; Wang, C.; Park, C.B. Ultra-lightweight, super thermal-insulation and strong PP/CNT microcellular foams. *Compos. Sci. Technol.* 2020, *191*, 108084.

120. Vergaro, V.; Abdullayev, E.; Lvov, Y.M.; Zeitoun, A.; Cingolani, R.; Rinaldi, R.; Leporatti, S. Cytocompatibility and uptake of halloysite clay nanotubes. *Biomacromolecules* 2010, *11*, 820–826.

121. Lvov, Y.M.; Shchukin, D.G.; Möhwald, H.; Price, R.R. Halloysite clay nanotubes for controlled release of protective agents. *ACS Nano* 2008, *2*, 814–820.

122. Di, Y.; Iannace, S.; Maio, E. Di; Nicolais, L. Poly(lactic acid)/organoclay nanocomposites: Thermal, rheological properties and foam processing. *J. Polym. Sci. Part B Polym. Phys.* 2005, *43*, 689–698.

123. Yuan, P.; Tan, D.; Annabi-Bergaya, F. Properties and applications of halloysite nanotubes: recent research advances and future prospects. *Appl. Clay Sci.* 2015, *112–113*, 75–93.

124. Massaro, M.; Lazzara, G.; Milioto, S.; Noto, R.; Riela, S. Covalently modified halloysite clay nanotubes: synthesis, properties, biological and medical applications. *J. Mater. Chem. B* 2017, *5*, 2867–2882.

125. Massaro, M.; Colletti, C.G.; Lazzara, G.; Milioto, S.; Noto, R.; Riela, S. Halloysite nanotubes as support for metal-based catalysts. *J. Mater. Chem. A* 2017, *5*, 13276–13293.

126. Konnova, S.A.; Sharipova, I.R.; Demina, T.A.; Osin, Y.N.; Yarullina, D.R.; Ilinskaya,

O.N.; Lvov, Y.M.; Fakhrullin, R.F. Biomimetic cell-mediated three-dimensional assembly of halloysite nanotubes. *Chem. Commun.* 2013, *49*, 4208–4210.

127. Abdullayev, E.; Abbasov, V.; Tursunbayeva, A.; Portnov, V.; Ibrahimov, H.; Mukhtarova, G.; Lvov, Y. Self-healing coatings based on halloysite clay polymer composites for protection of copper alloys. *ACS Appl. Mater. Interfaces* 2013, *5*, 4464–4471.

128. Abdullayev, E.; Lvov, Y. Halloysite clay nanotubes as a ceramic "skeleton" for functional biopolymer composites with sustained drug release. *J. Mater. Chem. B* 2013, *1*, 2894–2903.

129. Handge, U.A.; Hedicke-Höchstötter, K.; Altstädt, V. Composites of polyamide 6 and silicate nanotubes of the mineral halloysite: Influence of molecular weight on thermal, mechanical and rheological properties. *Polymer.* 2010, *51*, 2690–2699.

130. Alhuthali, A.; Low, I.M. Water absorption, mechanical, and thermal properties of halloysite nanotube reinforced vinyl-ester nanocomposites. *J. Mater. Sci.* 2013, *48*, 4260–4273.

131. Yuan, P.; Southon, P.D.; Liu, Z.; Green, M.E.R.; Hook, J.M.; Antill, S.J.; Kepert, C.J. Functionalization of halloysite clay nanotubes by grafting with γ- aminopropyltriethoxysilane. *J. Phys. Chem. C* 2008, *112*, 15742–15751.

132. Saif, M.J.; Asif, H.M.; Naveed, M. Properties and modification methods of halloysite nanotubes: A State-of-the-Art Review. *J. Chil. Chem. Soc.* 2018, *63*, 4109–4125.

133. Sansone, L.F. Process design for thermoplastic foam extrusion. In *Principles of Thermoplastic Foam Extrusion*; Lee, S.T., Ed.; Technomic Publishing Co., Inc.: Lancaster, 2000.

134. Thiele, W.C. Foam extrusion machinery features. In *Principles of Thermoplastic Foam Extrusion*; Lee, S.T., Ed.; Technomic Publishing Co., Inc.: Lancaster, 2000.

135. Naguib, H.E.; Park, C.B.; Reichelt, N. Fundamental foaming mechanisms governing the volume expansion of extruded polypropylene foams. *J. Appl. Polym. Sci.* 2004, *91*, 2661–2668.

136. Han, X.; Koelling, K.W.; Tomasko, D.L.; Lee, L.J. Effect of die temperature on the morphology of microcellular foams. *Polym. Eng. Sci.* 2003, *43*, 1206–1220.

137. Park, C.B.; Behravesh, A.H.; Venter, R.D. Low density microcellular foam processing in extrusion using CO_2. *Polym. Eng. Sci.* 1998, *38*, 1812–1823.

138. Park, C.B.; Baldwin, D.F.; Suh, N.P. Effect of the pressure drop rate on cell nucleation in continuous processing of microcellular polymers. *Polym. Eng. Sci.* 1995, *35*, 432–440.

139. Lee, K.; Chang, Y.W.; Kim, S.W. Ethylene-propylene-diene terpolymer/halloysite nanocomposites: Thermal, mechanical properties, and foam processing. *J. Appl. Polym. Sci.* 2014, *131*, 1–8.

140. Lee, S.T.; Ramesh, N.S. *Polymeric Foams: Mechanisms and Materials*; Lee, S.-T., Ramesh, N.S., Eds.; 1. Edition.; CRC Press: Boca Raton,FL, 2004; ISBN

9780203506141.

141. Kropp, D. Extrusion thermoplastischer Schäume mit alternativen Treibmitteln. [Dissertation], RWTH Aachen University, 1999.

142. Gendren, R.; Daigneault, L.E. Rheology of blowing agent charged polymeric systems. In *Principles of Thermoplastic Foam Extrusion*; Lee, S.T., Ed.; Technomic Publishing Co., Inc.: Lancaster, 2000.

143. Leslie, J.; Lane, C.; Grant, R. Melt strength improvement of PET, US4145466A, 1979.

144. Thomas, N.W.; Berardinelli, F.M.; Edelman, R. Polycarbodiimide modification of polyesters for extrusion applications, US4071503A, 1978.

145. Gallucci, R.R.; Nelson, L.H.; Shannon, T.G. Stabilization of polyesters using epoxy compounds in combination with a catalyst, WO1993002114A1, 1995.

146. Zhou, P.; Xia, Y.; Cheng, X.; Wang, P.; Xie, Y.; Xu, S. , 2014, 35, 10033-10045. *Biomaterials* 2014, *35*, 10033–10045.

147. Gendron, R.; Champagne, M.F. Effect of physical foaming agents on the viscosity of various polyolefin resins. *J. Cell. Plast.* 2004, *40*, 131–143.

148. Ashby, M.F. Cellular Solids - Scaling of Properties. In *Cellular Ceramics: Structure, Manufacturing, Properties and Applications*; Scheffler, M., Colombo, P., Eds.; WILEY-VCH Verlag GmbH & Co KGaA, 2005; p. 670 ISBN 3-527-31320-6.

149. Ko, W.L. Deformations of foamed elastomers. *J. Cell. Plast.* 1965, *1*, 45–50.

150. Zhu, H.X.; Mills, N.J.; Knott, J.F. Analysis of the high strain compression of open-cell foams. *J. Mech. Phys. Solids* 1997, *45*, 1875–1904.

151. Zhu, H.X.; Knott, J.F.; Mills, N.J. Analysis of the elastic properties of open-cell foams with tetrakaidecahedral cells. *J. Mech. Phys. Solids* 1997, *45*, 319–343.

152. Maiti, S.K.; Gibson, L.J.; Ashby, M.F. Deformation and energy absorption diagrams for cellular solids. *Acta Metall.* 1984, *32*, 1963–1975.

153. Gent, A.N.; Thomas, A.G. Mechanics of foamed elastic materials. *Rubber Chem. Technol.* 1963, *36*, 597–610.

154. Gent, A.N.; Thomas, A.G. The deformation of foamed elastic materials. *J. Appl. Polym. Sci.* 1959, *1*, 107–113.

155. Lederman, J.M. The prediction of the tensile properties of flexible foams. *J. Appl. Polym. Sci.* 1971, *15*, 693–703.

156. Cunningham, A. Modulus anisotropy of low-density cellular plastics: an aggregate model. *Polymer..* 1981, *22*, 882–885.

157. Christensen, R.M. Mechanics of low density materials. *J. Mech. Phys. Solids* 1986, *34*, 563–578.

158. Kanakkanatt, S. V. Mechanical Anisotropy of Open-Cell Foams. *J. Cell. Plast.* 1973, *9*, 50–53.

159. Gibson, L.J. The elastic and plastic behaviour of cellular materials. [Dissertation],

University of Cambridge, 1981.

160. Gibson, I..; Ashby, M.F. The mechanics of three-dimensional cellular materials. *Proc. R. Soc. London. A. Math. Phys. Sci.* 1982, *382*, 43–59.

161. Fathi, A. Mechanical properties of strand PET foams at different length scales. [Dissertation], University of Bayreuth, 2018.

162. Jung, A.; Diebels, S. Yield surfaces for solid foams: A review on experimental characterization and modeling. *GAMM-Mitteilungen* 2018, *41*, e201800002.

163. Ashby, M.. The properties of foams and lattices. *Philos. Trans. R. Soc. A Math. Phys. Eng. Sci.* 2006, *364*, 15–30.

164. Daniel, I.M.; Fenner, J.S.; Werner, B.T.; Cho, J.-M. Characterization and modeling of polymeric foam under multi-axial static and dynamic loading. In; 2017; pp. 123–134.

165. Aksit, M.; Gröschel, S.; Kuhn, U.; Aksit, A.; Kreger, K.; Schmidt, H.-W.; Altstädt, V. Low-density polybutylene terephthalate foams with enhanced compressive strength via a reactive-extrusion process. *Polymers.* 2020, *12*, 2021.

166. Aksit, M.; Zhao, C.; Klose, B.; Kreger, K.; Schmidt, H.; Altstädt, V. Extruded polystyrene foams with enhanced insulation and mechanical properties by a benzene-trisamide-based additive. *Polymers.* 2019, *11*, 268.

167. Dando, K.R.; Salem, D.R. The effect of nano-additive reinforcements on thermoplastic microballoon epoxy syntactic foam mechanical properties. *J. Compos. Mater.* 2018, *52*, 971–980.

168. Standau, T.; Hädelt, B.; Fafara, M.; Altstädt, V. Development of a bead foam based on the engineering polymer polybutylene terephthalate. In Proceedings of the AIP Conference Proceedings; 2019; Vol. 020039, p. 060004.

169. Köppl, T.; Fischer, B.; Altstädt, V. Challenges and possibilities in foaming of semicrystalline poly(butylene terephthalate). In Proceedings of the Blowing agents and foaming processes 2012 Conference Proceedings; Shawbury, U., Ed.; Smithers Rapra Publishing: Berlin, 2012; pp. 175–180.

170. Klotzer, R.; Paul, D.; Seibig, B. Extrusion of microcellular foams and applications. In Proceedings of the SPE ANTEC`97; 1997; pp. 2042–2045.

171. Richter, F.; Schmidt, H. Supramolecular nucleating agents for poly(butylene terephthalate) based on 1,3,5-benzenetrisamides. *Macromol. Mater. Eng.* 2013, *298*, 190–200.

172. Schmidt, H.-W.; Blomenhofer, M.; Stoll, K.; Meier, H.-R. Resin compositions, WO2004072168A3, 2004.

173. Mäder, D.; Hoffmann, K.; Schmidt, H.-W. Beta crystalline polypropylenes, WO2003102069A1, 2003.

174. Schmidt, H.-W.; Smith, P.; Blomenhofer, M. Polypropylene resin compositions, WO2002046300A2, 2002.

175. Du, M.; Guo, B.; Wan, J.; Zou, Q.; Jia, D. Effects of halloysite nanotubes on kinetics

and activation energy of non-isothermal crystallization of polypropylene. *J. Polym. Res.* 2010, *17*, 109–118.

176. Li, G.; Mu, X.; Fan, S.; Ren, X. Study on the Non-isothermal melt crystallization kinetics of PTT/PBT blends. *J. Macromol. Sci. Part B* 2009, *48*, 684–695.

177. Kissinger, H.E. Variation of peak temperature with heating rate in differential thermal analysis. *J. Res. Natl. Bur. Stand. (1934).* 1956, *57*, 217.

178. Spitael, P.; Macosko, C.W. Strain hardening in polypropylenes and its role in extrusion foaming. *Polym. Eng. Sci.* 2004, *44*, 2090–2100.

179. Gendron, R.; Daigneault, L.E. Rheology of thermoplastic foam extrusion process. In *Foam extrusion: Principles and Practice (Polymeric Foams)*; Lee, S.-T., Ed.; CRC Press Technomic Publishing: Florida, 2000; p. 35 ISBN 1566768799.

180. Trouton, F.T. On the coefficient of viscous traction and its relation to that of viscosity. *Proc. R. Soc. London. Ser. A, Contain. Pap. a Math. Phys. Character* 1906, *77*, 426–440.

181. Stadler, F.J.; Kaschta, J.; Münstedt, H.; Becker, F.; Buback, M. Influence of molar mass distribution and long-chain branching on strain hardening of low density polyethylene. *Rheol. Acta* 2009, *48*, 479–490.

182. Buahom, P.; Wang, C.; Alshrah, M.; Wang, G.; Gong, P.; Tran, M.-P.; Park, C.B. Wrong expectation of superinsulation behavior from largely-expanded nanocellular foams. *Nanoscale* 2020, *12*, 13064–13085.

183. Wunderlich, B. *Thermal Analysis of Polymeric Materials*; Springer-Verlag: Berlin/Heidelberg, 2005; ISBN 3-540-23629-5.

184. Okolieocha, C. Microcellular low-density nanocomposite foams nucleated by carbon-based nanofillers – processing, properties and foaming behaviour. [Dissertation], University of Bayreuth, 2019.

185. Sugimoto, M. Control of strain hardening of polymer melts under elongational flow. *J. Soc. Rheol.* 2008, *36*, 219–228.

186. Cailloux, J.; Santana, O.O.; Franco-Urquiza, E.; Bou, J.J.; Carrasco, F.; Gamez-Perez, J.; Maspoch, M.L. Sheets of branched poly(lactic acid) obtained by one step reactive extrusion calendering process: Melt rheology analysis. *Express Polym. Lett.* 2013, *7*, 304–318.

187. Bethke, C.; Goedderz, D.; Weber, L.; Standau, T.; Döring, M.; Altstädt, V. Improving the flame-retardant property of bottle-grade PET foam made by reactive foam extrusion. *J. Appl. Polym. Sci.* 2020, 49042.

188. Naguib, H.E.; Park, C.B.; Reichelt, N. Fundamental foaming mechanisms governing the volume expansion of extruded polypropylene foams. *J. Appl. Polym. Sci.* 2004, *91*, 2661–2668.

189. Supaphol, P. Nonisothermal bulk crystallization and subsequent melting behavior of syndiotactic polypropylenes: Crystallization from the melt state. *J. Appl. Polym. Sci.* 2000, *78*, 338–354.

190. Al-Mulla, A.; Mathew, J.; Yeh, S.-K.; Gupta, R. Nonisothermal crystallization kinetics of PBT nanocomposites. *Compos. Part A Appl. Sci. Manuf.* 2008, *39*, 204–217.

191. Zepnik, S.; Kabasci, S.; Kopitzky, R.; Radusch, H.; Wodke, T. Extensional flow properties of externally plasticized cellulose acetate: Influence of plasticizer content. *Polymers.* 2013, *5*, 873–889.

192. Okamoto, M.; Nam, P.H.; Maiti, P.; Kotaka, T.; Nakayama, T.; Takada, M.; Ohshima, M.; Usuki, A.; Hasegawa, N.; Okamoto, H. Biaxial flow-induced alignment of silicate layers in polypropy- lene/clay nanocomposite foam. *Nano Lett* 2001, *1*, 503–505.

193. Kluge, D.; Singer, J.C.; Neubauer, J.W.; Abraham, F.; Schmidt, H.-W.; Fery, A. Influence of the molecular structure and morphology of self-assembled 1,3,5-benzenetrisamide nanofibers on their mechanical properties. *Small* 2012, *8*, 2563–2570.

194. Oburoğlu, N.; Ercan, N.; Durmus, A.; Kaşgöz, A. effects of halloysite nanotube on the mechanical properties and nonisothermal crystallization kinetics of poly(butylene terephthalate) (PBT). *J. Macromol. Sci. Part B* 2012, *51*, 860–879.

195. Cassagnau, P. Melt rheology of organoclay and fumed silica nanocomposites. *Polymer.* 2008, *49*, 2183–2196.

196. Okamoto, M.; Nam, P.H.; Maiti, P.; Kotaka, T.; Nakayama, T.; Takada, M.; Ohshima, M.; Usuki, A.; Hasegawa, N.; Okamoto, H. Biaxial flow-induced alignment of silicate layers in polypropylene/clay nanocomposite foam. *Nano Lett.* 2001, *1*, 503–505.

197. Simona, P.L.; Spiru, P.; Ion, I. V. Increasing the energy efficiency of buildings by thermal insulation. *Energy Procedia* 2017, *128*, 393–399.

198. Azdast, T.; Hasanzadeh, R. Increasing cell density/decreasing cell size to produce microcellular and nanocellular thermoplastic foams: A review. *J. Cell. Plast.* 2020, 0021955X2095930.

10 Other sources

a.   Market Report, 2019. [online]. *Polymer Foam Market by Resin Type (PU, PS, PO, Phenolic), Foam Type (Rigid, Flexible), End-Use Industry (Building & Construction, Packaging, Automotive, Furniture & Bedding, Footwear, Sports & Recreational), and Region - Global Forecast to 2025*. [Accessed on: 25.08.2022]. Available under: https://www.marketsandmarkets.com/Market-Reports/foams-market-1011.html?gclid=CjwKCAjwu5yYBhAjEiwAKXk_eH9wEZgX5ej6XaE4FSPQQoF_e0Ku2jeMxCGTuX7Fs-jrFL_TDlPLhxoCm3AQAvD_BwE

b.   Wood L.; Market Report, 2016. [online]. *Global Polyethylene Terephthalate (PET) Foam Market Research Report 2016-2021 - Analysis of Wind Energy, Transportation, Marine, Packaging, Building & Construction & Others - Research and Markets.* [Accessed on: 04.09.2022]. Available under: https://www.prnewswire.com/news-releases/global-polyethylene-terephthalate-pet-foam-market-research-report-2016-2021---analysis-of-wind-energy-transportation-marine-packaging-building--construction--others---research-and-markets-300285202.html

c.   DeArmitt, C.; Phantom Plastics. Halloysite Handbook. [online]. [Accessed on: 04.09.2022]. Available under: https://phantomplastics.com/wp-content/uploads/2022/06/Halloysite-Handbook-Phantom-Plastics-v1.50-Web.pdf

d.   Evonik Industries AG. Rohacell® SL, Product Information. [online]. [Accessed on: 04.09.2022]. Available under: https://products.evonik.com/assets/33/98/243398.pdf

e.   Gurit Holding AG. Gurit® CORECELL™ M-Series, General Datasheet. [online]. [Accessed on: 06.09.2022]. Available under: https://www.gurit.com/-/media/gurit/datasheets/guritcorecell-m.pdf

f.   DIAB Group AB, Divinycell H, Technical Data. [online]. [Accessed on: 06.09.2022]. Available under: http://www.divinycell.com.br/pt/wp-content/uploads/2015/07/Datasheet-Divinycell-H-Barracuda-Diab-Group.pdf

g.   Armacell International S. A., ArmaPET® Struct FR, Technical Data. [online]. [Accessed on: 06.09.2022]. Available under: https://local.armacell.com/fileadmin/cms/pet-foams/ArmaPET_website/Product_Flyer/ArmaPET_Struct_FR.pdf

h.   BASF SE, Styrodur® C, Technical Data. [online]. [Accessed on: 06.09.2022]. Available under: https://www.tempra.is/static/files/pdf/styrodurc_properties-and-applications_10_2003.pdf

i.   Trassl, C., Evonik Industries AG 2022. Re: Density and elastic modulus of PMI [E-Mail]. 10.08.2022, 10:48

j.   RTP Company Inc., Styrene Acrylonitrile (SAN), Product Data Sheet & General Processing Conditions. [online]. [Accessed on: 06.09.2022]. Available under: https://www.rtpcompany.com/mp-files/san-0010-rtp-500.pdf/

k.   Vinidex, Polyvinyl Chloride (PVC), PVC Properties. [online]. [Accessed on: 06.09.2022]. Available under: https://www.vinidex.com.au/technical-resources/material-properties/pvc-properties/

l.   Röchling Industries, Sustadur® PET, Datasheet. [online]. [Accessed on: 06.09.2022]. Available under: https://www.roechling.com/industrial/materials/thermoplastics/detail/ sustadur-pet-140

m.   INEOS STYROLUTION, Styrolution Polystyrene PS 158N/L, Technical Datasheet. [online]. [Accessed on: 06.09.2022]. Available under: https://www.ineos-styrolution.com/INTERSHOP/web/WFS/Styrolution-Portal-Site/en_US/-/USD/ViewPDF-Print.pdf?SKU=200300060584&RenderPageType=ProductDetail

n.   European Commission, Green Paper, 2000. [online]. *Environmental issues of PVC*; Brussels. [Accessed on: 06.09.2022]. Available under: http://aei.pitt.edu/1202/1/envir onment_PVC_gp_COM_2000_469.pdf

o.   Goepfert, R., LANXESS Deutschland GmbH 2017. Re: Molekulargewicht von PBT Pocan B 1600 / 1700 [E-Mail]. 13.09.2017, 15:29

p.   Weber, M., BASF SE 2017. Re: Molekulargewicht von PBT Ultradur B6550 [E-Mail]. 13.09.2017, 13:27

q.   LANXESS Deutschland GmbH, POCAN® B 1600 000000, Data Sheet. [online]. [Accessed on: 07.09.2022]. Available under: https://techcenter.lanxess.com/scp/ameri cas/en/products/datasheet/LANXESS_Pocan_B1600_000000_ISO_EN.pdf?docId=31 437929

r.   LANXESS Deutschland GmbH, POCAN® B 1700 000000, Data Sheet. [online]. [Accessed on: 07.09.2022]. Available under: https://techcenter.lanxess.com/scp/ameri cas/en/products/datasheet/LANXESS_Pocan_B1700_000000_ISO_EN.pdf?docId=31 454849

s.   BASF SE Ultradur® B 6550 LN, Product Information. [online]. [Accessed on: 07.09.2022]. Available under: https://www.google.com/url?sa=t&rct=j&q=&esrc=s&s ource=web&cd=&cad=rja&uaua=8&ved=2ahUKEwidybednoL6AhXYtKQKHYOTD wgQFnoECAMQAQ&url=httht%3A%2F%2Fdownload.basf.com%2Fp1%2F8a8081c 57fd4b609017fd62eaf2a5445%2Fde%2FULTRADUR%253Csup%253E%25C2%25 AE%253Csup%253E_B6550_LN&usg=AOvVaw301C7LlmPDkGZy51Xf1rUZ

t.   BASF SE Joncryl® Styrene acrylic resins, Product Selection Guide. [online]. [Accessed on: 07.09.2022]. Available under: https://www.google.com/url?sa=t&rct=j&q=&esrc= s&source=web&cd=&cad=rja&uact=8&ved=2ahUKEwjOqOeQn4L6AhU6IcUKHeS QDDoQFnoECAgQAQ&url=https%3A%2F%2Fwww.basf.com%2Fhk%2Fdocument s%2Fen%2Fproducts-industries%2Fpackaging-and-print%2FBASF_Printing_Packaging_Product_Guide_201803.pdf&usg=AOvVaw0Ub rUCgc_stKza86TB3Ub-
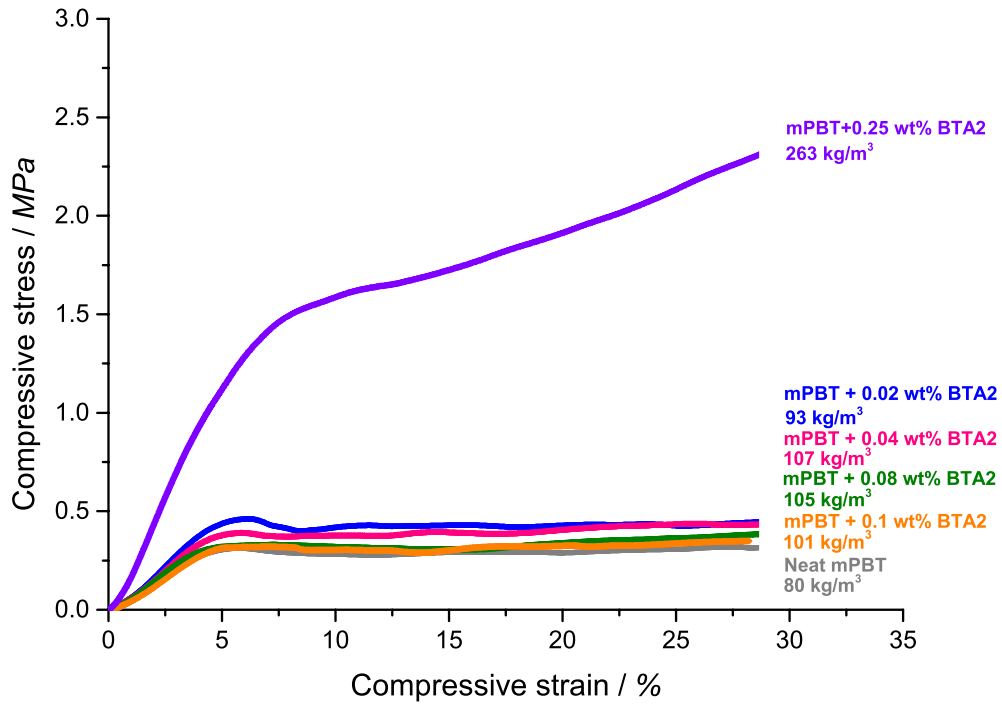
11 Appendix

Figure A1 Compressive stress-strain curve of the neat mPBT foam and mPBT foams with all concentrations of BTA2 including 0.25 wt%.

Table A1 Properties of all foam samples.

Sample	Comp. modulus [MPa]	Comp. strength [kPa]	Foam density [kg/m³]	Strut thickness [μm]	Strut length [μm]	Open cell content [%]	Degree of crystallinity [%]
Neat mPBT	9 ± 1	368 ± 21	81 ± 1	127 ± 24	334 ± 128	42 ± 1	33 ± 1
BTA1							
0.02 wt%	12 ± 2	486 ± 22	86 ± 2	141 ± 34	454 ± 194	65 ± 1	29 ± 2
0.04 wt%	14 ± 2	650 ± 33	97 ± 1	177 ± 44	400 ± 158	80 ± 2	31 ± 3
0.08 wt%	10 ± 1	460 ± 16	80 ± 1	113 ± 20	309 ± 102	42 ± 1	29 ± 2
0.1 wt%	12 ± 1	451 ± 62	137 ± 4	264 ± 118	853 ± 394	71 ± 9	31 ± 3
0.25 wt%	7 ± 3	585 ± 54	99 ± 6	191 ± 73	578 ± 220	85 ± 1	34 ± 1

Sample	Comp. modulus [MPa]	Comp. strength [kPa]	Foam density [kg/m^3]	Cell edge (strut) thickness [μm]	Strut length [μm]	Open cell content [%]	Degree of crystallinity [%]
BTA2							
0.02 wt%	11 ± 1	498 ± 23	93 ± 1	128 ± 25	317 ± 88	30 ± 1	30 ± 1
0.04 wt%	11 ± 1	421 ± 36	105 ± 1	156 ± 39	548 ± 231	52 ± 2	30 ± 1
0.08 wt%	9 ± 1	383 ± 20	107 ± 2	113 ± 50	543 ± 195	53 ± 3	29 ± 1
0.1 wt%	8 ± 1	382 ± 12	96 ± 2	181 ± 59	520 ± 191	58 ± 6	29 ± 1
0.25 wt%	27 ± 6	1408 ± 180	240 ± 20	153 ± 52	393 ± 168	59 ± 2	31 ± 1
HNT							
0.02 wt%	10 ± 1	463 ± 16	81 ± 1	95 ± 15	154 ± 45	69 ± 3	31 ± 2
0.04 wt%	13 ± 2	495 ± 22	85 ± 1	116 ± 21	251 ± 85	46 ± 5	29 ± 2
0.08 wt%	14 ± 2	520 ± 59	108 ± 2	187 ± 66	616 ± 237	59 ± 2	29 ± 1
0.1 wt%	16 ± 2	596 ± 48	116 ± 1	214 ± 81	621 ± 274	55 ± 2	29 ± 1
0.25 wt%	17 ± 2	605 ± 23	113 ± 3	188 ± 56	545 ± 292	51 ± 1	29 ± 1
Synergy							
BTA1+ BTA2	21 ± 2	622 ± 47	98 ± 1	100 ± 23	257 ± 98	42 ± 1	32 ± 2
HNT+ BTA1	16 ± 3	613 ± 38	82 ± 1	87 ± 14	219 ± 88	50 ± 1	30 ± 1
HNT+ BTA2	13 ± 1	464 ± 26	75 ± 2	97 ± 20	98 ± 3	47 ± 2	31 ± 1
BTA1+ BTA2+ HNT	16 ± 3	626 ± 15	82 ± 1	92 ± 15	156 ± 62	53 ± 2	29 ± 2

12 Curriculum Vitae

Personal data	Merve Aksit 21.08.1990, Bursa
Marital status	Married
Nationality	Turkish

Education	2004 – 2008	Ulubatli Hasan Anotolian High School
		Diploma in Mathematics & Science
	2008 – 2013	Izmir Institute of Technology
		B.Sc. in Chemical Engineering
	2013 – 2016	Friedrich-Alexander University Erlangen Nürnberg
		M.Sc. (hons.) in Advanced Materials and Processes
Professional experience	2016 – 2021	Associate Research Fellow
		Polymer Engineering, University of Bayreuth
	2021 – 2023	Career break for maternity leave
	Since 02/2023	Polymer Engineer
		GNS Gesellschaft für Nuklear-Service mBH

13 Publications and Conference Contributions

<u>**Reviewed Publications:**</u>

M. Aksit, *B. Klose, C. Zhao, K. Kreger, H.-W. Schmidt, V. Altstädt*

Morphology Control of Extruded Polystyrene Foams with Benzene-Trisamide-Based Nucleating Agents
Journal of Cellular Plastics 55 (3), pp. 249-261, 2019
DOI: https://doi.org/10.1177/0021955X19837508

M. Aksit, *C. Zhao, B. Klose, K. Kreger, H.-W. Schmidt, V. Altstädt*

Extruded Polystyrene Foams with Enhanced Insulation and Mechanical Properties by a Benzene-Trisamide-Based Additive

Polymers 11(2), pp. 268, 2020
DOI: https://doi.org/10.3390/polym11020268

M. Aksit, *S. Gröschel, U. Kuhn, A. Aksit, K. Kreger, H.-W. Schmidt, V. Altstädt*

Low-Density Polybutylene Terephthalate Foams with Enhanced Compressive Strength via a Reactive-Extrusion Process

Polymers 12(9), pp. 2021, 2020
DOI: https://doi.org/10.3390/polym12092021

A. Aksit, T. Menzel, ***M. Aksit***, *V. Altstädt*

Properties of Styrene-Maleic Anhydride Copolymer Compatibilized Polyamide 66/Poly (Phenylene Ether) Blends: Effect of Maleic Anhydride Concentration and Copolymer Content

Materials, 13(5), pp. 1237, 2020
DOI: https://doi.org/10.3390/ma13051237

A. Aksit, N. Geis, ***M. Aksit***, *V. Altstädt,*

Properties of Styrene-Maleic Anhydride Copolymer Compatibilized Polyamide 66/Poly (Phenylene Ether) Blends: Effect of Blend Ratio and Compatibilizer Content

Materials, 13(15), pp. 3400, 2020
DOI: https://doi.org/10.3390/ma13153400

*B. Klose, D. Kremer, **M. Aksit**, K. P. van der Zwan, K. Kreger, J. Senker, V. Altstädt, H.-W. Schmidt*

Kinked Bisamides as Efficient Supramolecular Foam Cell Nucleating Agents for Low-Density Polystyrene Foams with Homogeneous Microcellular Morphology
Polymers 13 (7), pp. 1094, 2021
DOI: https://doi.org/10.3390/polym13071094

*K. Hofmann, M. Gehde, **M. Aksit**, V. Altstädt,*

Process Design and Influencing Factors in the case of the Welding of Foamed Thermoplastics (TSG)
Joining Plastics 15 (1), pp. 18-24, 2021

Conference Contributions:

***M. Demir**, M. Mörl, C. Steinlein, K. Kreger, H.-W. Schmidt, V. Altstädt*

Effect of Supramolecular Additives on the Morphology and Mechanical Properties of Polymer Foams

Oral presentation: Polymer Processing Society Europe-Africa (PPS-29), Dresden, 2017

***M. Demir**, M. Mörl, C. Steinlein, K. Kreger, H.-W. Schmidt, V. Altstädt*

Polypropylene Foams with Supramolecular Additives

Poster: 17th Bayreuth Polymer Symposium (BPS), Bayreuth, 2017

***M. Demir**, M. Mörl, C. Steinlein, K. Kreger, H.-W. Schmidt, V. Altstädt*

Effect of Supramolecular Additives on the Morphology and Properties of Semicrystalline Polymer Foams

Oral presentation: International SPE Foams Conference, Bayreuth, 2017

***M. Demir**, V. Altstädt*

Extruded Polystyrene Foams Nucleated by Supramolecular Additive to Enhance the Foam Morphology and Properties

Oral presentation: International SPE Foams Conference, Montreal, 2018

<u>Patents:</u>

*A. Seidel, S. Hobeika, S. Bärwinkel, **M. Demir**, V. Altstädt*
Polycarbonate Compositions Having Good Mechanical Properties
Patent No: EP3562885A1, 2019

*A. Seidel, S. Hobeika, S. Bärwinkel, **M. Aksit**, V. Altstädt*
Polycarbonate Compositions with Good Mechanical Properties
Patent No: EP3562885B1, 2020